THESIS

EVALUATING THE IMPACT OF DEEP-WATER CHANNEL ARCHITECTURE ON THE PROBABILITY OF CORRECT FACIES CLASSIFICATION USING 3D SYNTHETIC SEISMIC DATA

Submitted by

Teresa Rose Langenkamp

Department of Geosciences

In partial fulfillment of requirements

For the Degree of Master of Science

Colorado State University

Fort Collins, Colorado

Fall 2021

Master's Committee:

Advisor: Lisa Stright

Dennis Harry
Richard Eykholt

ABSTRACT

EVALUATING THE IMPACT OF DEEP-WATER CHANNEL ARCHITECTURE ON THE PROBABILITY OF CORRECT FACIES CLASSIFICATION USING 3D SYNTHETIC SEISMIC DATA

Modeling studies of bed-to geobody-scale architecture in deep-water channel deposits reveal that channel element stacking patterns and internal architecture strongly control connectivity. This architecture is critical to understanding hydrocarbon flow and recovery but is unresolvable in exploration-scale seismic-reflection profiles. Forward seismic reflectivity modeling of a digital outcrop models is commonly used to explore how depositional architecture is interpretable in a filtered seismic response. One limitation of forward seismic reflectivity modeling studies is that they often stop short of qualitatively assessing the link between underlying depositional architecture and seismic response. This study addresses the gap between qualitative interpretation and quantitative evaluation by calculating the prediction reliability of inverted seismic data.

Specifically, this study uses synthetic 3D seismic modeling and inversion of a 3D outcrop model of deepwater channels in the Tres Pasos Formation of the Magallanes Basin of southern Chile. The model includes outcrop- (bed and geobody) to seismic- (reservoir to basin) scale architecture. The primary objective is to quantify where and when channel architecture is accurately predicted by seismic facies classification. Bayesian classification is used to test the probability of correct facies classification from P-impedance and if the classification results are dependent upon architectural styles (e.g., channel element stacking patterns). Model sensitivity variables include seismic frequency (ranging from 15 to 180 Hz) and deep versus shallow rock properties. Results show that prediction reliability increased for both channel element axis sandstone and mass transport deposits with increasing frequency. Deep reservoirs or faster seismic velocities more accurately predict facies than shallow reservoirs or slower seismic velocities due to the increasing contrast between sandstone and shale velocities. Channel axis sandstone is less easily interpreted where channel elements are vertically aggraded, reducing acoustic impedance contrasts with background shale. When channel elements are laterally stacked or disorganized, facies can be predicted from seismic attributes with a higher confidence, due to a strong contrast between channel element sandstone and background shale. This study highlights that architectural information strongly impacts 3D inverted seismic data and highlights conditions that either hinder or aid accurate interpretation from facies classification.

ACKNOWLEDGEMENTS

This work adds to and builds upon geologic research conducted by the Chile Slope Systems (CSS) Joint Industry Project, which is a collaboration between the University of Calgary, Colorado State University, and Virginia Tech. Phase III industry partners which supported this study include: Repsol, Nexen/CNOOC, ConocoPhillips, BHP, Equinor, and Petrobras. Fieldwork, data collection, and interpretation of the Laguna Figueroa outcrop used in this study were performed by Brian Romans, Steve Hubbard, Ryan Macauley, Sean Fletcher, and Sarah Southern. The deterministic model in this study was created by Andrew Ruetten, who built upon the groundwork of Casey Meirovitz. Thank you to Andrew Ruetten and Noah Vento who provided valuable insight into the study area, navigating Petrel, AAPG, and life at CSU. I want to express my gratitude to my committee members: Dennis Harry and Richard Eykholt. Thank you to Lisa Stright for bringing me to CSU, seeing my potential, being an inspiring female role model, and providing advice, guidance, and support on this project and throughout my time in graduate school. Lastly, thank you to my instructors in the CSU Geoscience Department, IBA mentors and team, family, and friends at CSU who taught me, supported me, and made my time here memorable.

TABLE OF CONTENTS

CHAPTER 1: RESEARCH MOTIVATION

1.1 Introduction

Deep-water slope deposits host some of the largest and most valuable oil and gas reserves in the world, but prior to 3-D seismic data (circa 1985) were challenging to drill successfully (Pettingill and Weimer, 2002). Since 1985, the oil and gas industry has had increasing success in the exploration for hydrocarbons in deep-water settings (Pettingill and Weimer, 2002) due largely to technological advances in 3D seismic acquisition, processing, and interpretation (Alfaro et al., 2007), engineering advances, including drilling (Epelle and Gerogiorgis, 2020) and geotechnical advances, including new techniques and equipment to characterize the seabed (Randolph et al., 2011). Increasing success in exploration for hydrocarbons is also a result of scientists gaining a better understanding of deep-water sedimentological processes and their resulting deposits.

Accumulations of sediment on deep-water slopes are a result of sediment gravity-flows in the marine environment, transporting sediment from the shelf to the seafloor (Slatt, 2006). These processes have historically been difficult to monitor, but recent research has provided new data on sediment gravity-flows, including sediment trap samples, velocity measurements, and seafloor cores (Maier et al., 2019). Monitoring modern seafloor processes provides insight into how such processes create and preserve deposits of sand in ocean basins, deposits that are seen at the bed-scale in outcrop and core. This deep-water architecture, specifically channel fill styles and stacking patterns, strongly controls reservoir fluid distribution and flow connectivity (Jackson et al., 2019; Meirovitz et al., 2020). However, this scale of architecture, which is on the order of 10's of meters thick and 100-400 meters wide (McHargue et al., 2011) is difficult to interpret in seismic-reflection profiles due to limits of resolvability (e.g., Stright et al., 2014; Nielson, 2017; Pemberton et al., 2018).

Advances in seismic data acquisition, processing and interpretation reduce the risk of drilling deep-water wells in a poor location that proves to be uneconomic (e.g., poor quality reservoir or limited reservoir thickness, negligible to no hydrocarbon saturation). When this happens, it is called drilling a dry hole. These advances improve the difficult task of interpreting drill locations using seismic data by better predicting reservoir presence and quality. Advances in data acquisition include increasing azimuthal coverage of the survey to improve signal to noise ratio, thus improving seismic data quality, along with vertically aligning sources and receivers (Alfaro et al., 2007). Improved processing techniques, such as surface-related multiple elimination (SRME), also improve seismic data quality by reducing noise (Alfaro et al., 2007). Additionally, new workflows have been created for more reliable interpretation of subsurface architecture using single seismic attributes (e.g., inversion models) and combinations of seismic attributes (e.g., amplitude, phase, and spectral frequency; La Marca, 2020). Seismic attributes are used in interpretation and modeling workflows (Chopra and Marfurt, 2008), and increasingly in machine learning workflows (La Marca et al., 2019; Li et al., 2019). Finally, advances in computing capabilities have led to improved efficiency (e.g., processing speed and resolution; Neal & Krohn, 2012).

While these improvements lower the risk of drilling a dry hole through more accurate imaging and interpretation, correct versus incorrect interpretation cannot be checked or evaluated due to unknown architecture and challenges with resolvability. Understanding the linkage between reliable facies classification and architecture can aid in interpretation and modeling workflows with the goal of decreasing risk in exploration and development. Forward seismic reflectivity modeling of outcrops explores interpretability of depositional architecture in a filtered seismic response (Biddle et al., 1992; Stafleu and Schlager, 1995; Campion et al., 2000; Gartner et al., 2001; Tomasso et al., 2006; Schwab et al., 2007; Falivene et al., 2010; Pemberton et al., 2018). One limitation of this approach is that it stops short at qualitatively assessing the link between underlying depositional architecture and seismic response, and concludes, somewhat predictably, that decreasing seismic frequency results in a decrease in resolvability without quantification of the error in the prediction (Schwab et al., 2007). This study addresses this gap by quantifying interpretable deep-water channel architecture preserved in inverted seismic data.

For this study, an architecturally accurate geocellular model (Ruetten, 2021), derived from outcrop observations and interpretations (Macauley and Hubbard, 2013; Fletcher, 2013; Southern et al., 2017), forms the foundation of forward seismic models which are then in turn, inverted and classified. Comparison of the resulting classification with the truth model provides a clear understanding of the probability of correct classification and how it is a function of architecture. Using 3D synthetic forward seismic modeling and inversion, the overarching goal is to quantify how well acoustic impedance accurately predicts deep-water channel architecture. Specifically, one objective is to look at correct versus incorrect classification of channel element axis sandstone and mass transport deposits (MTDs) as a function of frequency. Classification sensitivity to deep and shallow rock properties is also evaluated. Finally, the impact of architecture on correct versus incorrect classification is further evaluated as a function of channel element stacking patterns.

1.2 Thesis Format

Beyond this chapter, there are an additional five chapters (Chapters 2-6). Chapter 2 reviews the geologic background of the Magallanes Basin and provides a description of the Laguna Figueroa outcrop, including data, observations, facies and stratigraphic interpretation. Previous modeling work of this outcrop that is the foundation for this research, is reviewed. Chapter 3 presents the methodology and results of forward seismic modeling and inverse modeling. Chapter 4 presents the methodology and sensitivity analysis of the facies classification using inverse models from Chapter 3. The impact of facies architecture on sensitivity is also examined within Chapter 4. Chapter 5 discusses the implications this study has for reservoir prediction and reservoir modeling. Chapter 6 provides the conclusions and discusses future work that could be done related to this study.

CHAPTER 2: GEOLOGIC BACKGROUND

2.1 Geologic Setting

The Magallanes Basin is a retroarc foreland basin on the tip of South America, covering parts of Chile and Argentina (Fig. 1A: Fildani and Hessler, 2005; Romans et al., 2011; Daniels et al., 2019). The Rocas Verdes backarc basin underlies the Magallanes basin and formed from extension related to the Jurassic breakup of Gondwana (Dalziel et al., 1974; Wilson, 1991; Fildani and Hessler, 2005; Fosdick et al., 2011; Romans et al., 2011). Compression caused uplift of the Andean fold-thrust belt, the closure of the Rocas Verdes Basin and the formation of the Magallanes retroarc foreland basin along the western margin of South America (Dalziel et al., 1974; Wilson, 1991; Fildani and Hessler, 2005; Fosdick et al., 2011; Romans et al., 2011). The subsidence was promoted by the dense extensional predecessor basin, the Rocas Verdes Basin (Covault et al., 2009; Romans et al., 2009). This, in addition to the load added by the fold and thrust belt, produced bathymetric relief of the shelf-to-basin floor profile that is comparable with large-scale continental margins (Covault et al., 2009; Romans et al., 2009). As a result, this basin contains over 4000 m of deep-water fill (Fildani and Hessler, 2005; Romans et al., 2010). A longitudinal basin filling pattern is seen from north to south (Romans et al., 2009).

The three major phases of deposition occurred in the Magallanes Basin during the Cretaceous. The first phase is recorded in the Punta Barrosa Formation (~92-85 Ma) which consists of thin-bedded, sandy turbidites (Fig. 1; Fildani and Hessler, 2005; Romans et al., 2010; Romans et al., 2011). Overlying the Punta Barrosa Formation is the second phase of the shale dominated Cerro Toro Formation (86-80 Ma) with a conglomeratic channel-levee-complex system running parallel to the basin axis (Fig. 1; Romans et al., 2011). The third phase of deposition is the Tres Pasos Formation (81-72 Ma), which represents the final deep-water phase and infilling of the basin through a prograding clinoform system (Fig. 1; Romans et al., 2011. This deep-water slope system transported turbidity currents resulting in slope deposits of sandstone rich channel elements with related thin-bedded inner and outer levee deposits (Hubbard et al., 2010; Romans et al., 2011). Various scales of mudstone-rich MTDs are also present at the base of the Tres Pasos Formation marking the initiation of slope progradation and intermittently higher up in the stratigraphy within the channelized sections (Romans et al., 2009; Hubbard et al., 2010; Romans et al., 2011; Macauley and Hubbard, 2013). The overlying Dorotea formation (~72-65 Ma), consisting of shallow marine deltaics, is genetically linked as a sediment source for the progradational slope system (Fig. 1; Covault et al., 2009; Romans et al., 2009).

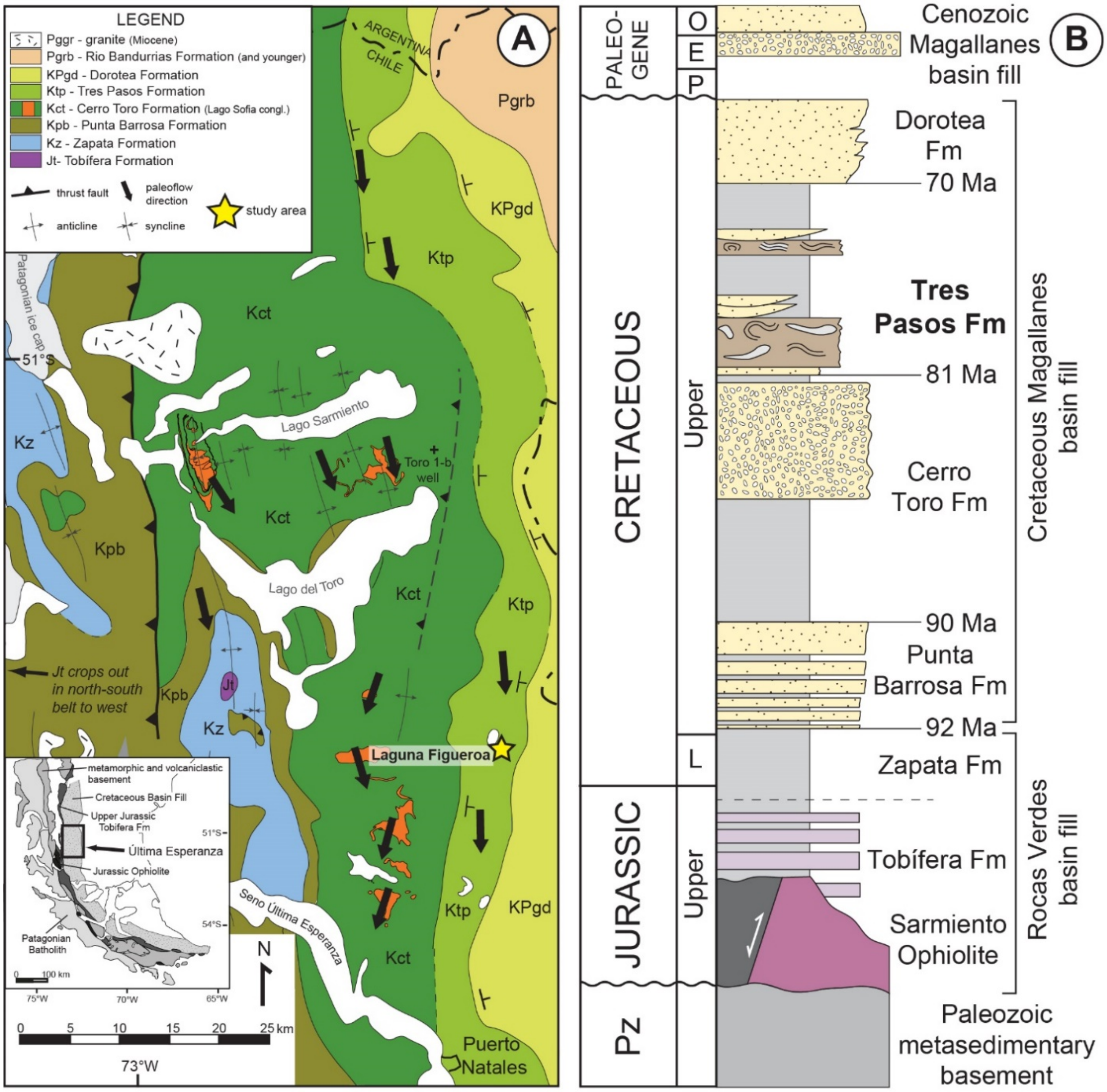

Figure 1. (A) Geologic map of the Última Esperanza District in southern Chile (Vento, 2020; modified from Romans et al., 2011; originally adapted from Wilson, 1991; and Fosdick et al., 2011). This map shows the formations of the Magallanes Basin. Moving to the east, the Late Cretaceous-age strata becomes older with a paleoflow direction of south to southeast along the axis of the elongate basin. The Tres Pasos Fm. (Ktp), modeled in this study, is located to the east of the Cerro Toro Fm. (Kct) and west of the Dorotea Fm. (KPgd). The star marker represents the study area, Laguna Figueroa, which is located north of Puerto Natales. (B) Stratigraphic column of the Magallanes Basin (Modified from Daniels et al., 2018, GSA Bulletin) with the Tres Pasos Fm. bolded.

2.2 Laguna Figueroa Outcrop

The Laguna Figueroa outcrop, named for a nearby lake, is a 2.5 km long, 300 m thick section of the uplifted slope system located in the Última Esperanza District of Chile (Figs. 1A and 2A; Fletcher, 2013; Macauley and Hubbard, 2013). Data collected along the 2.5 km long and 300 m thick Laguna Figueroa outcrop exposure include 68 measured sections totaling 3,435 m and over 100 paleocurrent measurements comprise the foundation for sedimentological and stratigraphic interpretations (Figs. 2B and 2C; Fletcher, 2013; Macauley and Hubbard, 2013; Southern et al., 2017). Additional supplementary data was used to guide channel element plan view interpretation and geocellular modeling, including thousands of GPS points, high-resolution satellite imagery, and drone data resulting in photomosaics and drone photogrammetry models. These data help to delineate facies transitions as well as capture the major stratigraphic horizons (Fletcher, 2013; Macauley and Hubbard, 2013; Southern et al., 2017).

2.2.1 Description of Facies and Interpretation

Analysis of bed-scale observations (e.g., grainsize, bed thickness, sedimentary structures) resulted in the interpretation of 4 facies (F1-F4) which include: thick-bedded, highly amalgamated sandstone (F1); thick- to thin-bedded, semi-amalgamated sandstone and siltstone (F2); and thick- to thin-bedded, largely non-amalgamated sandstone and siltstone (sandstone-dominated) (F3); and medium- to very-thin bedded largely non-amalgamated sandstone and siltstone (siltstone-dominated) (F4) (Fig. 3; Fletcher, 2013; Macauley and Hubbard, 2013; Southern et al., 2017).

The internal channel element architecture is formed mainly from these facies, which are correlated with channel position (Macauley and Hubbard, 2013). Channel element axis sandstone is predominantly composed of F1, while channel margins are predominantly composed of F3 (Fig.

3). Between the channel element axis and the margin, the "off-axis" is predominantly composed of F2 (Fig. 3, Macauley and Hubbard, 2013). Thin-bedded F4 is present along the bases of the channel elements, predominantly below the margin and off-axis and less commonly present draping the channel element base below the axis. Channel element stacking and these thin drapes are important features due to their impact on reservoir connectivity and flow (Jackson et al., 2019; Meirovitz et al., 2020; Ruetten, 2021). Although channel element base drapes are critical in defining reservoir flow pathways, these facies are sub-seismic scale and are not imaged in seismic reflectivity.

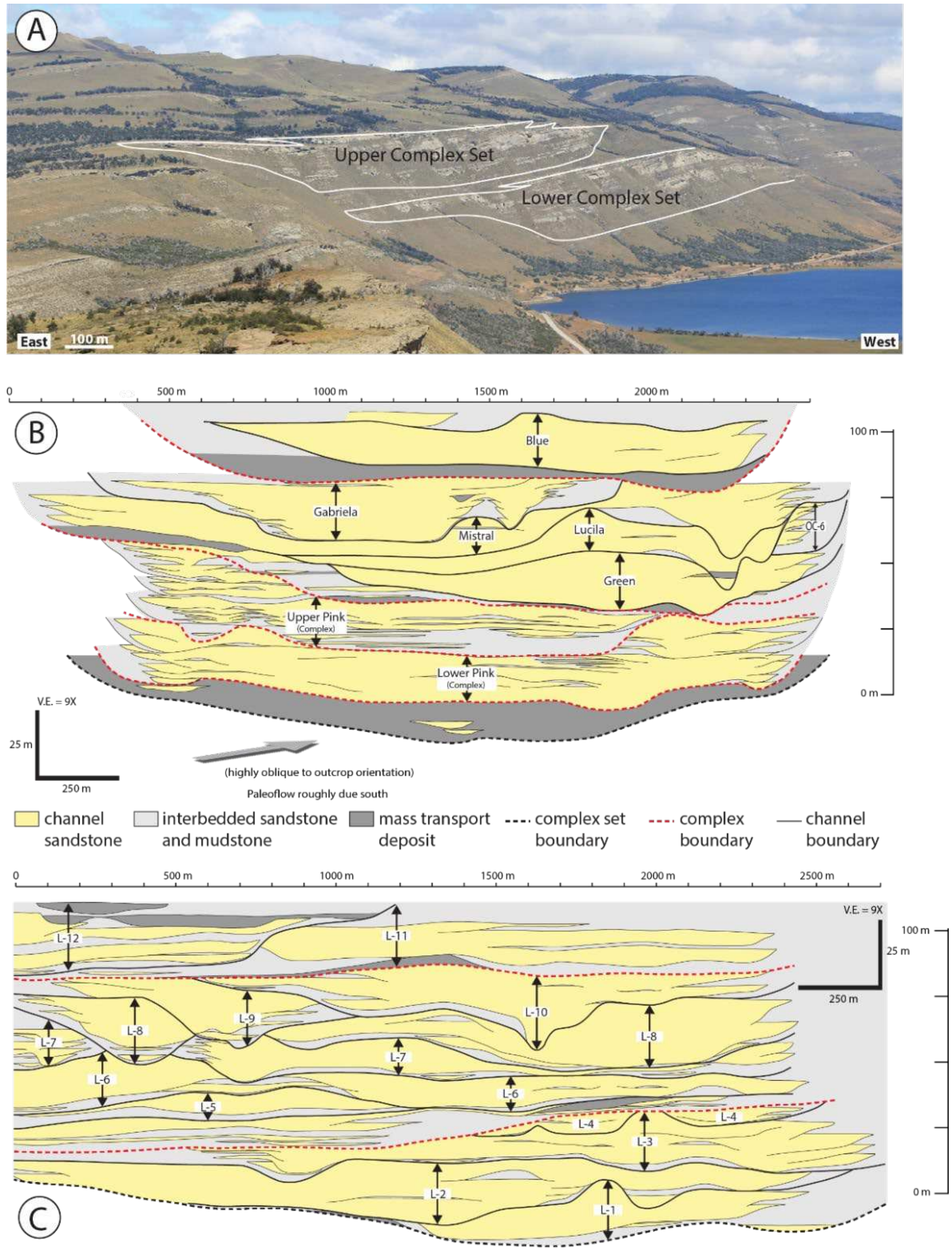

Figure 2. (A) Photo of the outcropping deep-water channel strata of the Laguna Figueroa outcrop with complex sets outlined (Modified from Ruetten 2021; originally adapted from Daniels et al., 2019). (B) Oblique dip-oriented cross section of Upper Figueroa with channel elements labeled. Channel complexes are separated by dashed red lines. Note that Lower and Upper Pink are each distinct complexes (adapted from Southern et al., 2017). (C) Oblique dip-oriented cross section of Lower Figueroa with channel elements labeled. Channel complexes are separated by dashed red lines (adapted from Southern et al., 2017).

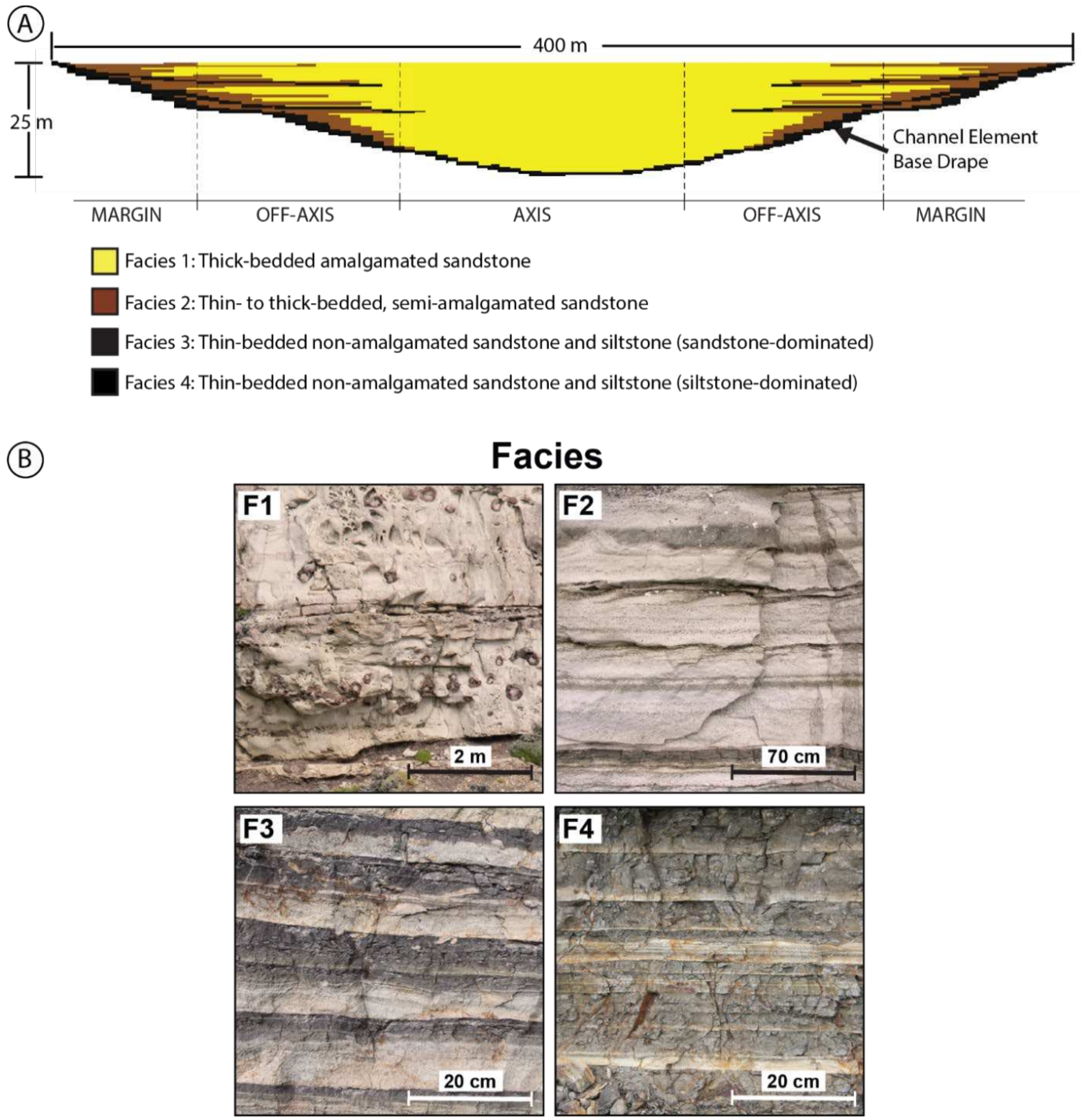

Figure 3. (A) Channel element cross section showing channel positions and related facies. (B) Photos of channel element facies including: F1 – thick-bedded amalgamated sandstone; F2 – thin- to thick-bedded, semi-amalgamated sandstone; F3 – thick- to thin-bedded non-amalgamated sandstone and siltstone (sandstone-dominated); and F4 – medium- to very-thin bedded largely non-amalgamated sandstone and siltstone (siltstone-dominated). (Modified from Jackson et al., 2019 and Meirovitz et al. (2020).)

Three additional facies are observed at the outcrop and in analog subsurface data that are important to this study: inner levee and outer levee facies, and mass transport deposit (MTD) facies. The inner levee and outer levee facies comprise the model background. In the model, the outer levees fully or partially bound the entire channel-levee system (Kane and Hodgson, 2011; Macauley and Hubbard, 2013). Smaller, internal levees bound individual channel elements within the channel belt. (Kane and Hodgson, 2011). The levees present at Laguna Figueroa are composed of mudstone-prone turbiditic deposits, and are often covered by vegetation (Deptuck et al., 2003; Macauley and Hubbard, 2013; Hubbard, 2014). Due to a lack of levee exposure at the outcrop, it is difficult to know whether the entire channel system is erosionally- or levee-confined.

Mass transport deposits (MTDs) are formed by submarine mass movement and include debris-flow deposits and slide deposits (Nardin et al., 1979; Armitage and Stright, 2009). MTDs can act as a reservoir, a migration pathway, or as a seal due to varying lithologies (Cardona et al., 2020). Within the Tres Pasos Formation at Laguna Figueroa, the widespread MTDs show chaotically bedded mudstone and sandstone (Fletcher, 2013). They overlie deep-incision surfaces and underlie channel elements (Fletcher, 2013). MTDs are also present in the outcrop within channel elements, between channel elements, and draping the bases of some complexes and between the lower and upper channel complex set (Macauley and Hubbard, 2013; Hubbard et al., 2014; Pemberton et al., 2018). MTDs modeled in this study have low porosity and permeability, acting as baffles and barriers to fluid flow (Ruetten, 2021).

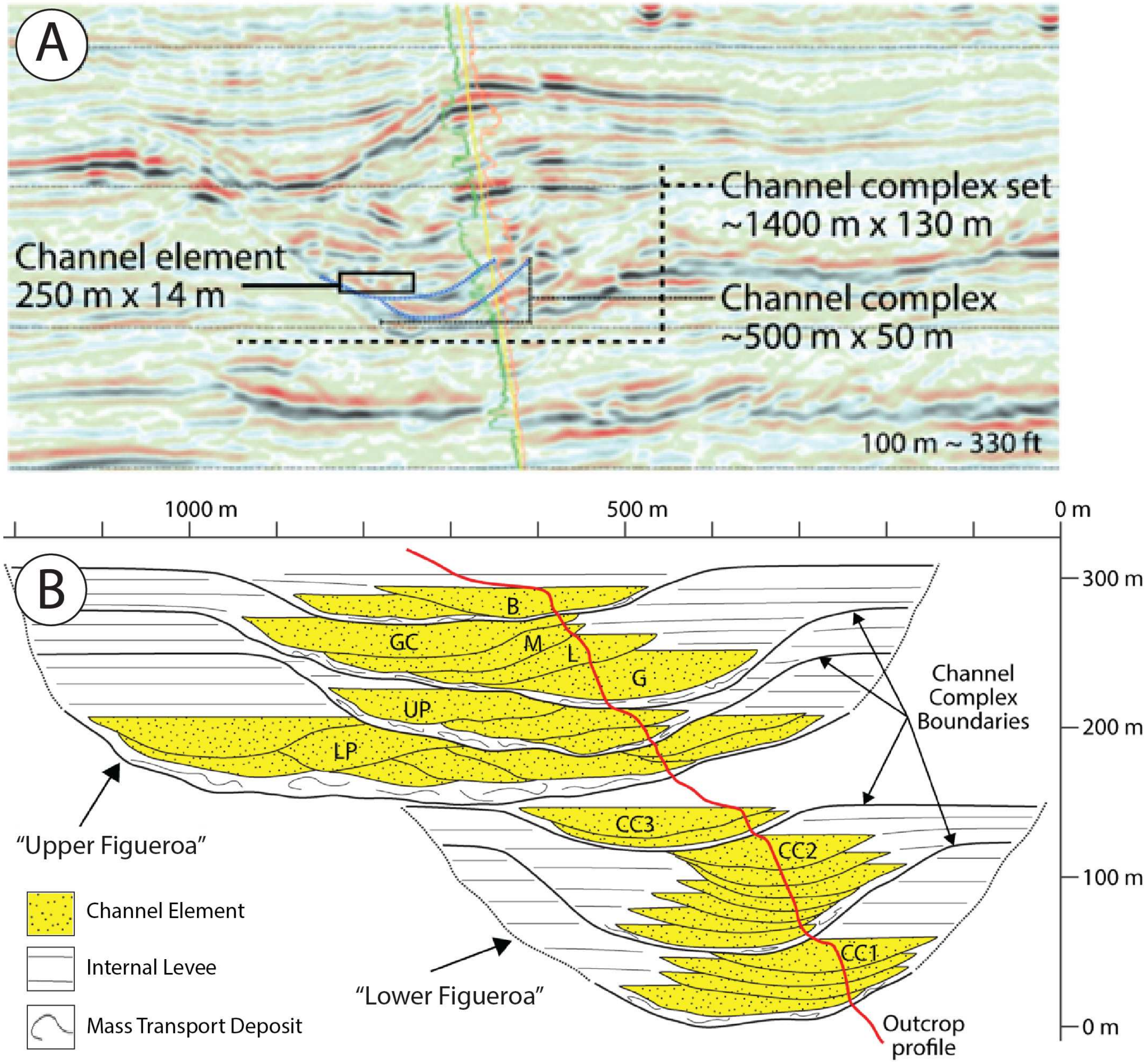

Figure 4. (A) Deep-water channel system stratigraphic hierarchy displayed in a seismic reflection image from the Dalia field, West Africa. The scale of various features is highlighted as well as their seismic response (Modified from Jackson et al., 2019; originally from Zhang et al., 2017). (B) Conceptual model of Lower and Upper Laguna Figueroa outcro Hierarchical architecture is shown, including channel complex boundary surfaces. (Modified from Ruetten, 2021; originally adapted from Macauley and Hubbard, 2013 and Covault et al., 2016). A different number of channel elements is used in this interpretation, but it maintains a similar overall hierarchy. The red line marks the outcrop profile.

2.2.2 Deep-water Stratigraphic Hierarchy

The outcrops at Laguna Figueroa contains high-quality exposures of channelized turbidite systems (Macauley and Hubbard, 2013; Southern et al., 2017; Fletcher, 2013). Deep-water architecture is often categorized using a common stratigraphic hierarchy (Fig 2A and 2B). At Laguna Figueroa there are two channel systems (i.e., complex sets; Fig. 2A), Lower and Upper Figueroa, separated by a mass transport complex (MTC), which consists of a series of stacked mass transport deposits (MTDs) (Fig. 4B; Ruetten, 2021).

The channel element is the main architectural element of channelized deep-water systems, and it is made up of a composite channel surface and sediment infill (Fig. 4A; McHargue et al., 2011; Fig. 3A). A series of genetically related stacked channel elements, laterally or vertically, organized or disorganized, make up a channel complex (Fig. 4A). A series of genetically related channel complexes make up a channel complex set (Fig. 4A; McHargue et al., 2011).

The first interpretation of the Laguna Figueroa outcrop was only comprised of strata from the lower channel complex set and was interpreted as 18 individual channel elements grouped into 3 channel complexes (Macauley and Hubbard, 2013). Additional work and new data collected in the area, revised this original interpretation to 12 channel elements in 3 complexes (Fig. 4B and 3C; Southern et al., 2017) and expanded the interpretation to include the upper channel complex set with four channel complexes and thirteen individual channel elements (Fig. 4B and 3B; Fletcher, 2013; Southern et al., 2017).

2.3 Previous Modeling Work

The work presented in this thesis is the next step in a series of modeling studies of the Laguna Figueroa outcrop, built upon the previous work of researchers in the Chile Slope Systems joint industry project. Sedimentological observations and interpretations of the Laguna Figueroa outcrop (Macauley and Hubbard, 2013; Fletcher, 2013; Southern et al., 2017) served as the foundation for fine-scale geocellular models utilizing planforms and vertical stacking which analyzed static connectivity (Jackson et al., 2019; Ruetten, 2021). Further studies analyzed the influence of stacked channel element architecture on seismic response (Nielson, 2017; Pemberton et al., 2018), and how stacking patterns matter for reservoir connectivity and fluid flow (Meirovitz et al., 2020; Ruetten, 2021). The database of outcrop statistics used to create these models (Southern et al., 2017) was also used in a study designed to bridge the gap between sedimentology and data analytics using machine learning algorithms to predict stratigraphic architecture and heterogeneity in a deep-water slope channel system (Vento, 2020).

2.3.1 Legacy Modeling Work (2013-2019)

Stratigraphic interpretations provided the basis for the modeling work, and at the Lower Figueroa channel complex set, 18 channel elements were interpreted by Macauley and Hubbard (2013). These interpretations were used to create the first geocellular model of the Laguna Figueroa outcrop which was constructed for a study that analyzed static connectivity (Jackson et al., 2019). The fine-scale model had cell sizes of 2m x 2m x 0.25 m (6.5 ft x 6.5 ft x 0.8 ft; total model size > 600 M cells) and focused on channel elements and their stacking patterns without explicit stratigraphic hierarchical groupings. Channel elements had dimensions of 200-300 m wide and 14 m thick. Complex surfaces and MTDs were not included in this model. Jackson et al.

(2019) examined how upscaling grid cell size impacted the "true" connectivity observed in the fine-scale model. They concluded that connectivity is a function of cell size, which is a decision in the modeling workflow. Furthermore, connectivity is highest when channel elements are vertically stacked and lowest when they are laterally stacked. When lateral migration between successive channel elements was more than 2/3 of a channel element width, connections are cut off completely. Thin channel element base drapes are responsible for controlling connectivity (Jackson et al., 2019). Channel element base drapes do not contribute significantly to net-to-gross (NTG), the fraction of reservoir volume occupied by hydrocarbon-bearing rocks, and are sub-seismic scale. This is important because if a system is interpreted as high NTG from seismic interpretation and/or attributes, connectivity could be overestimated. Linking stacking patterns to connectivity highlights the importance of correctly interpreting and predicting channel element architecture from seismic interpretation.

Given the role of element stacking and intra-element heterogeneity on static connectivity, a second study explored the impact on dynamic reservoir connectivity and performance (Meirovitz et al., 2020). Meirovitz et al. (2020) isolated two channel elements in twelve different stacking patterns to explore the impact of bed- to geobody-scale architecture on fluid flow connectivity in a water flood scenario (Meirovitz et al., 2020). Their results further supported the conclusion that thin-beds (i.e., drapes and thin-bedded margin facies; facies 3 and 4) impeded flow in laterally offset stacked scenarios, and flow is funneled through vertically aligned channel elements (Meirovitz et al., 2020). If the thin-beds are not taken into account in recovery estimates, the flow and recoveries are misleadingly optimistic (Meirovitz et al., 2020).

These two research studies begged the question of what architecture can be interpreted in the seismic reflection data to guide connectivity, fluid flow and recovery predictions. Therefore, a seismic-reflectivity modeling study using the two element models generated by Meirovitz et al. (2020) provided insight into when and at which frequencies channel element stacking patterns might be detectable in seismic (Nielson, 2017). Nielson (2017) utilized rock properties from multiple cored wells that penetrate the subsalt Gulf of Mexico, an analogous depositional system. 1-D convolutional forward seismic models were generated using a Ricker wavelet with peak frequencies of 20, 30, 40, 50, 60, 90, 120 and 180 Hz. Nielson (2017) analyzed these models by interpretating top and base of channel element pairs, calculating RMS amplitude and exploring RMS amplitude as a function of both true stratigraphic thickness and apparent thickness. He found that laterally migrating channel elements are harder to interpret stratigraphically in comparison with vertically aggrading channel elements due to tuning. If a priori information is known about channel element width and thickness, patterns seen in seismic-reflection profiles could be used to interpret one versus two channel elements and infer stacking patterns (Nielson, 2017). However, Nielson (2017) recognized the simplicity of the modeling and that the inclusion of more than two channel elements would generate more challenges to interpretation.

To test the impact of multiple channel elements and their realistic stacking configurations, the 18-channel element geocellular model created by Jackson et al. (2019) provided the foundation for a study to analyze the influence of stacked channel element architecture on seismic-reflectivity (Pemberton et al., 2016). Pemberton et al. (2016) generated a synthetic seismic model of the Jackson et al. (2019) Laguna Figueroa model and compared the results to a synthetic seismic model of the nearby outcrop showing weakly confined channel strata (Arroyo Picana; Pemberton et al., 2018). Arroyo Picana architecture includes channel elements of varying widths and depths, as well as variably sized scours and scour complexes (Pemberton et al., 2016). Rock properties for both models came from the same analogous depositional system in the Gulf of Mexico used by Nielson (2017). Forward seismic models were generated using a Ricker wavelet at peak frequencies of 15, 30, 60, 90, 120, and 180 Hz and 1-D convolution for both study areas. The confined channel strata at Laguna Figueroa were generally more accurately resolved in seismic reflection data than the mixed channel and scour architecture at Arroyo Picana until the lowest frequencies (i.e., 15 and 30 Hz) where neither were clearly resolved (Pemberton et al., 2018). Tuning effects result in composite seismic surfaces that were vertically displaced from their true location, inhibiting accurate interpretation, and erroneously grouping strata into stratigraphic packages in which they did not belong (Pemberton et al., 2018). Additionally, at peak frequencies commonly encountered in the subsurface, the number of complexes were underestimated and size, shape and type of architectural bodies (channels vs. scours; large vs. small channels) were difficult to differentiate. Gross rock volume (total reservoir volume) calculations were over-estimated by 10% - 50%, the error increasing with decreasing frequency (Pemberton et al., 2018).

While these modeling studies provided insight into how architecture impacts static and dynamic connectivity and seismic-reflectivity responses, they did not include critical architecture including MTDs, channel element grouping into complexes and complex sets.

2.3.2 Updated Architectural Model (2019-present)

A new interpretation was created in which the upper channel complex set at Laguna Figueroa was measured, mapped and interpreted similar to the lower channel complex set used for the legacy modeling work (Fletcher, 2013; Southern et al., 2017). Southern et al., (2017) also reinterpreted the lower channel complex set to fewer channel elements, 12 instead of 18, causing them to be thicker. These new data and interpretations, along with measured sections and mapped surfaces provided the foundation for a new seismic-scale, deterministic, 3D geocellular model

(Fig. 4A; Figs. 5 and 6; Ruetten, 2021). Ruetten's (2021) model encompassed Lower and Upper Laguna Figueroa and captured hierarchal organization including complex and complex set surfaces, along with MTDs associated with these surfaces. A detailed description of how the geocellular model used in this study was built can be found in Ruetten (2021) and will be briefly described herein.

Ruetten (2021) created a deterministic outcrop model that is 265 m high, 2.25 km long (orientated north to south), and 2 km wide (oriented east to west) and with ~ 5.7 M grid cells that are 50 m x 50 m x 2.5 m (Figs. 5 and 6), a significant increase from Jackson et al. (2019) cell sizes. The model includes two channel complex sets, Lower and Upper Figueroa, separated by a MTC (Fig. 2; Hubbard et al., 2014). Within the lower channel complex set, twelve channel elements have been interpreted within three channel complexes (Fig. 2). Each channel element has a standardized width of 400 m and a thickness of 25 m (Ruetten, 2021), compared to the previous channel element dimensions of 200-300 m wide and 14 m thick (Jackson et al., 2019). Within the upper channel complex set, eight channel elements have been interpreted within four channel complexes (Fig. 2). The exception is the lowest element in the upper channel complex set, modeled as a laterally migrating, sandy, amalgamated channel complex of multiple indistinguishable channel elements, which is 800 m wide (Ruetten, 2021).

Ruetten's (2021) outcrop model was used to test how fluid flow behavior responds to channel element stacking patterns, channel element net to gross ratio, channel element base drape coverage, and MTD properties (Ruetten, 2021). Drapes and/or low NTG margins acted as baffles that reduced water breakthrough, with increasing drape leading the baffle to become a barrier (Ruetten, 2021). Reservoir compartmentalization was also created in a variety of ways, revealed by this study, including channel element base drape coverage, laterally divergent stacking patterns, low NTG margins, and the presence of MTDs, which all resulted in a reduction in recovery efficiency (RE; Ruetten, 2021). Ruetten (2021) compared the deterministic flow responses to simplified models to better understand general flow character. He also attempted to model the channel elements and MTDs with object-based methods to see if the flow character could be reproduced with simple out-of-the-box modeling tools, but it could not.

The database of outcrop statistics from Lower and Upper Laguna Figueroa was further utilized in a study designed to bridge the gap between sedimentology and machine learning to predict stratigraphic architecture (Vento, 2020). Variables which captured channel element stacking patterns (i.e., channel element positions: axis, off-axis, and margin) were classified by the machine learning algorithms. Complex algorithms (i.e., random forest, XGBoost, and neural networks) had higher accuracies, above 80%, while less complex algorithms, (i.e., decision trees), had lower accuracies, between 60% - 70% (Vento, 2020). Additionally, the transitional off-axis class was more difficult for the machine learning algorithms to classify, compared to axis and margin (Vento, 2020).

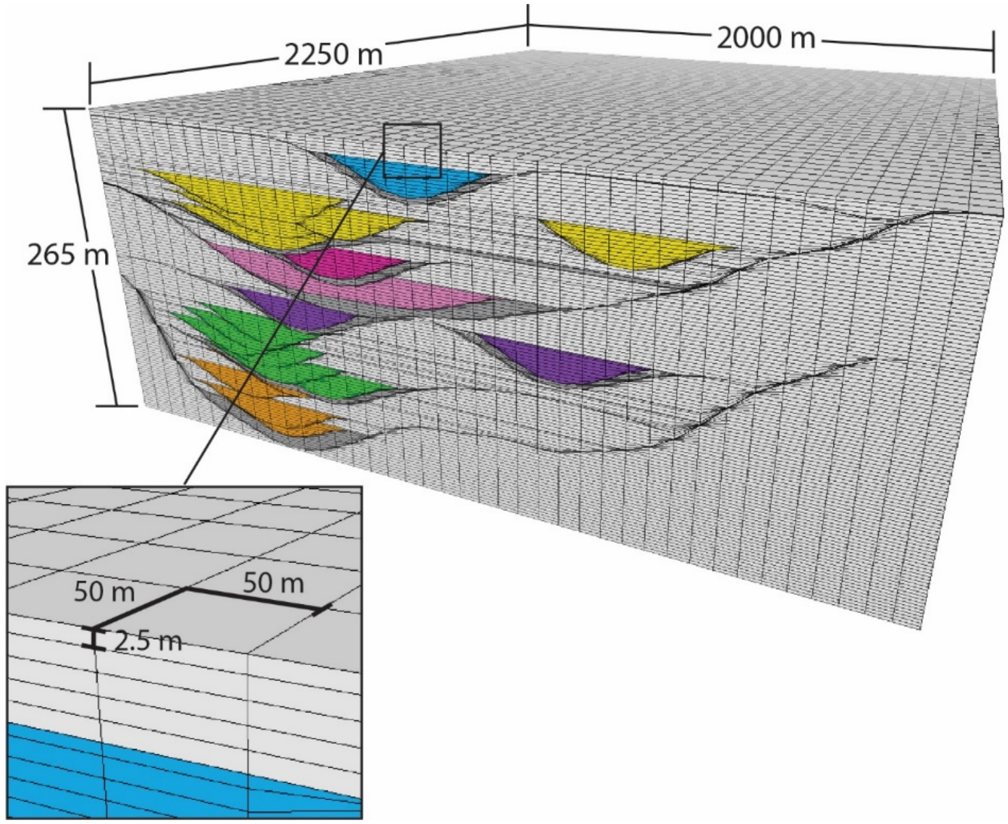

Figure 5. 3D geocellular model displaying model dimensions with inset showing grid cell dimensions. Channel elements are color coded according to channel complex. MTCs are shown in gray at the base of each channel complex (Ruetten, 2021).

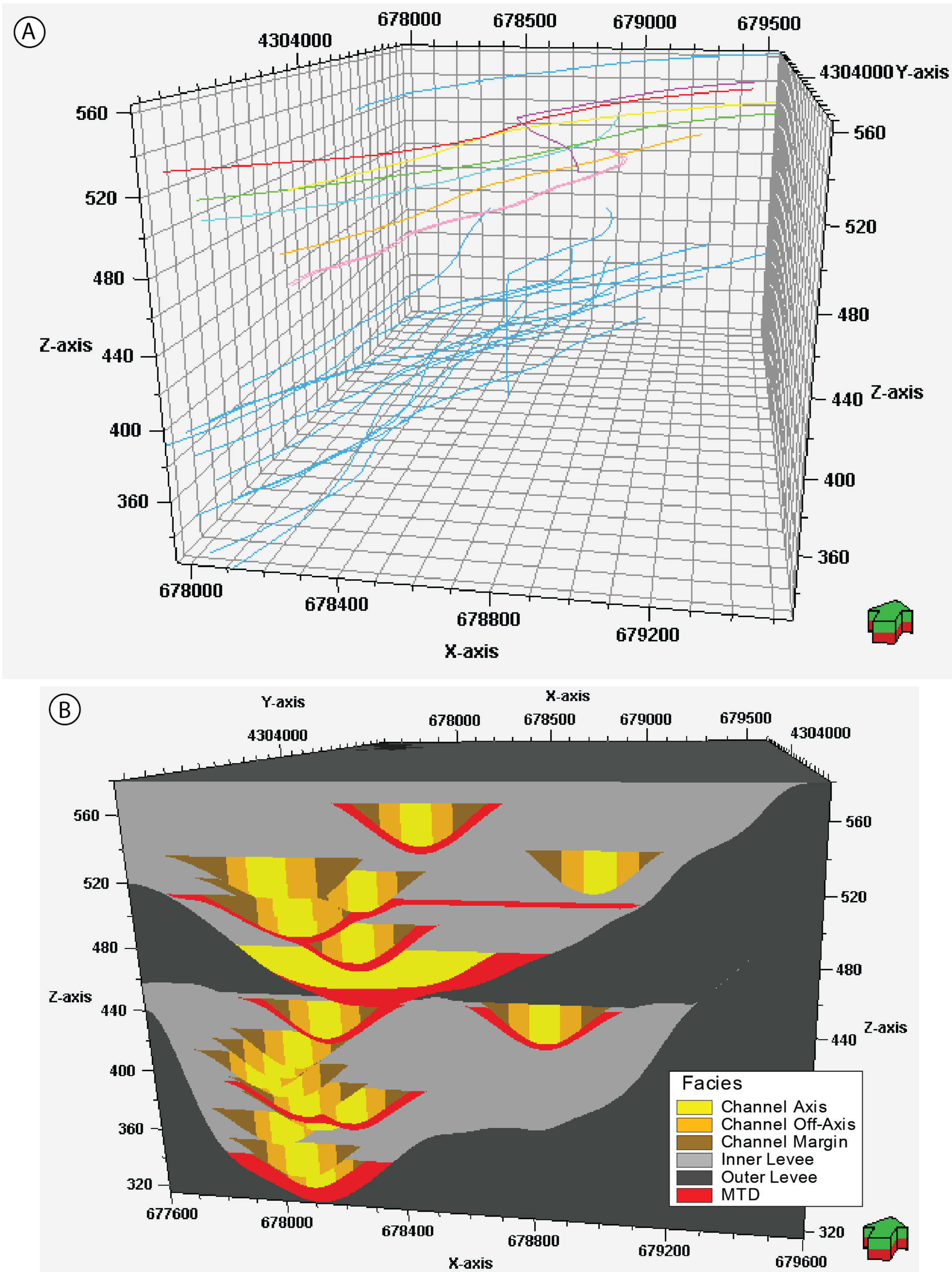

Figure 6. Facies within the model were calculated using a normalized distance from the centerline (A). Axis is within 15% of the centerline, Off-Axis is 15% to 34% of the centerline, Margin is 34% and beyond from the centerline. (B) The resulting facies model with vertical cutoffs.

CHAPTER 3: FORWARD SEISMIC AND INVERSE MODELING

3.1 Methodology

This study utilizes 3D synthetic forward seismic and inverse modeling of the seismic-scale, 3D geocellular model generated by Ruetten (2021) to quantify how well acoustic impedance can be used to accurately predict and interpret deep-water channel facies and subsequent architecture. The forward seismic modeling process begins with a facies model derived from outcrop data (Fig. 7). An earth model of acoustic impedance (AI) is defined by assigning analogous AI properties to this facies model (Fig. 7). A reflectivity series can be derived from the AI model and then convolved with an input wavelet to generate the forward model (Fig. 7). The inverse modeling process begins by deconvolving the wavelet from the seismic trace to obtain a reflectivity series and subsequent AI for each seismic trace. From this model, facies classification models can be produced to generate a model of the probability of encountering specific facies at any point in the seismic volume (Fig. 7).

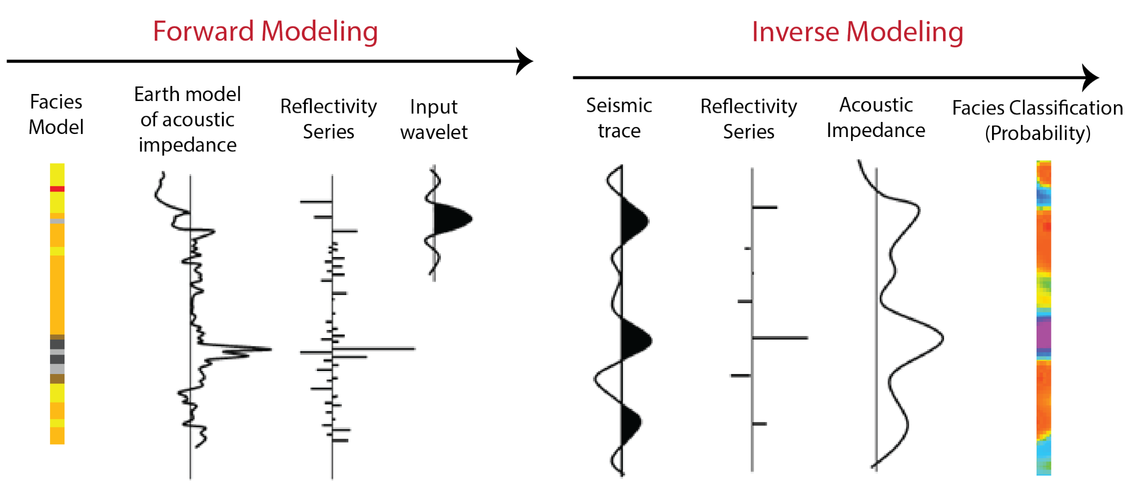

Figure 7. The forward and inverse modeling process, showing how it begins and ends with an acoustic impedance model. (Modified from Stright, *CSU course materials*).

3.1.1 Rock Properties Assigned to Facies

Average acoustic impedance (AI) values from analogous deep-water systems (shallow offshore West Africa and deep Gulf of Mexico) are assigned to facies to create two unique AI models (Fig. 8; Table 1).

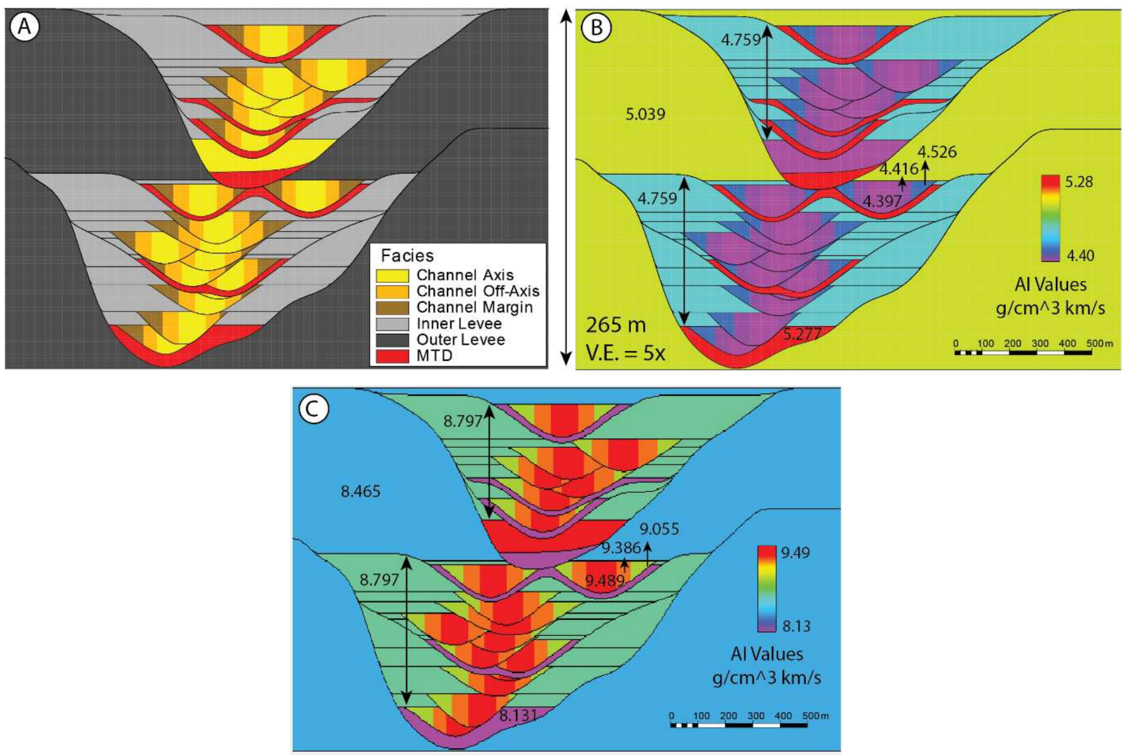

Figure 8. 2D cross sections from 3D models showing A) the facies model, and B) AI values assigned to each facies using values from shallow offshore West Africa, C) AI values assigned to each facies using values from deep Gulf of Mexico, which together lead to the input AI earth models.

Table 1. Acoustic Impedance (AI) value assigned to each facies for the AI model. Shallow and deep rock properties were used to construct two separate models.

Facies	Shallow West Africa Acoustic Impedance (g/cm^3 km/s)	Deep Gulf of Mexico Acoustic Impedance (g/cm^3 km/s)
Channel Axis	4.397	9.489
Channel Off Axis	4.416	9.386
Channel Margin	4.526	9.055
Inner Levee	4.759	8.797
Outer Levee	5.039	8.465
Mass Transport Deposit	5.277	8.131

3.1.2 Forward modeling method

In this study, forward seismic models are generated in Petrel™ 2019 (Schlumberger, 2019) from the geocellular model (Ruetten, 2021). Zones of overburden and underburden 300 m thick are added to bound the model. The model was converted from depth to time using a constant interval velocity of 3,750 m/s and converted back from time to depth using that same velocity. This velocity (3,750 m/s) is close to the velocity for interbedded sandstone and shale (3,675 m/s) from the deep Gulf of Mexico rock properties.

Forward seismic models are created using 1D convolution with Ormsby wavelets at varying dominant frequencies of 15, 30, 60, 90, and 180 Hz (Fig. 9; Table 2). Ormsby wavelets were used rather than simple Ricker wavelets because Ormsby wavelets contain numerous side lobes, rather than only two, resulting in a smaller impact to the shape of the amplitude tuning curve (Fig. 9; Table 2; personal communication Andrew Wilson from CNOOC).

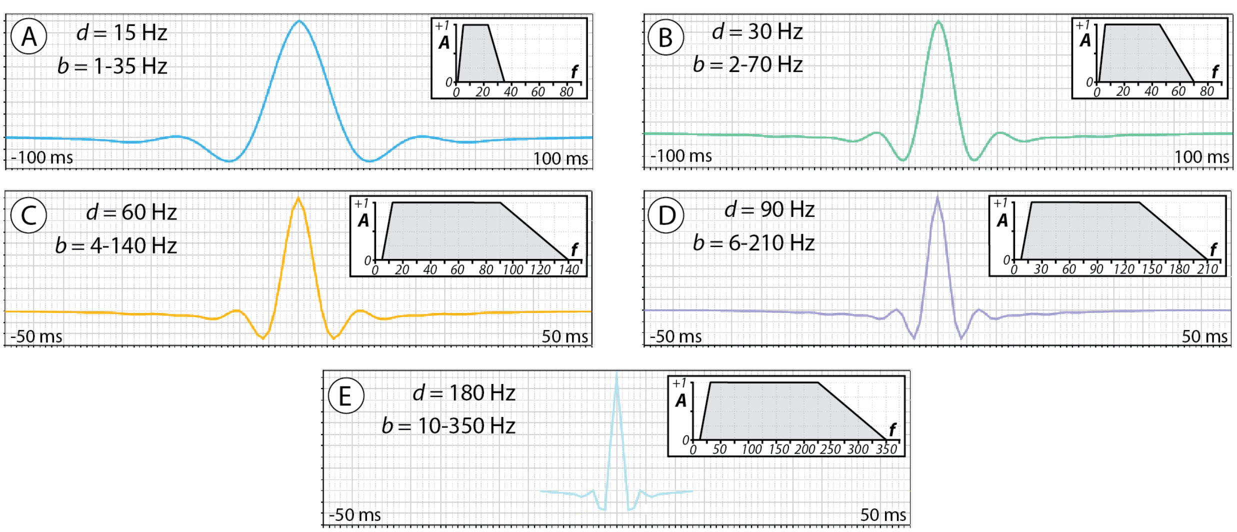

Figure 9. Ormsby Wavelets used in this study with dominant frequencies, d, of (A) 15 Hz, (B) 30 Hz, (C) 60 Hz, (D) 90 Hz, (E) 180 Hz. The diagrams in the upper right corner show the amplitude and trapezoidal shaped frequency spectrum used when making the wavelet.

Table 2. Ormsby wavelet dominant frequency and parameters used to create each wavelet. Ormsby wavelets are created using a low-cut, low-pass, high-pass, and high-cut frequency, rather than a single dominant frequency.

Dominant Frequency (Hz)	Length (ms)	Sample Rate (ms)	Low-Cut Frequency (Hz)	Low-Pass Frequency (Hz)	High-Pass Frequency (Hz)	High-Cut Frequency (Hz)
15	200	1	1	3	23	35
30	200	1	2	6	45	70
60	100	1	4	12	90	140
90	100	1	6	18	135	210
180	26	1	10	30	225	350

To create the forward seismic models, the algorithm selected was post stack, normal incidence and the parameter used was acoustic impedance. The post-stack trace can be approximately modeled using the convolutional model of the recorded seismogram (Yilmaz, 2001) which is given by:

$$\boldsymbol{s_t} = [\boldsymbol{r_t} * \boldsymbol{w_t} + \boldsymbol{n_t}] \tag{1}$$

In this equation, s_t = the seismic trace, r_t = the earth's reflectivity, w_t = the seismic wavelet, n_t = additive noise, and "*" denotes convolution (Russell and Hampson, 1991; Yilmaz, 2001). Noise was not added to these models because this was not a variable observed in this study. Noise could be added in further studies to study its effects.

Two different background models were used to represent the earth's reflectivity, comparing deep Gulf of Mexico rock properties with shallow offshore West Africa rock properties. Combining the background assigned acoustic impedance models with the Ormsby wavelets produced a variety of forward seismic models. Below a workflow graphic shows the detailed process of creating the forward models (Fig. 10). Forward seismic models were created at frequencies of 15, 30, 60, 90, and 180 Hz for shallow offshore West Africa rock properties and frequencies of 15, 30, and 60 Hz, for deep Gulf of Mexico rock properties. Channel element base drapes are not directly modeled in this work, however, they may be interpreted or modeled from seismic reflection data where channel elements are imaged due to their clear association with channel elements. These forward seismic models are used for inverse modeling.

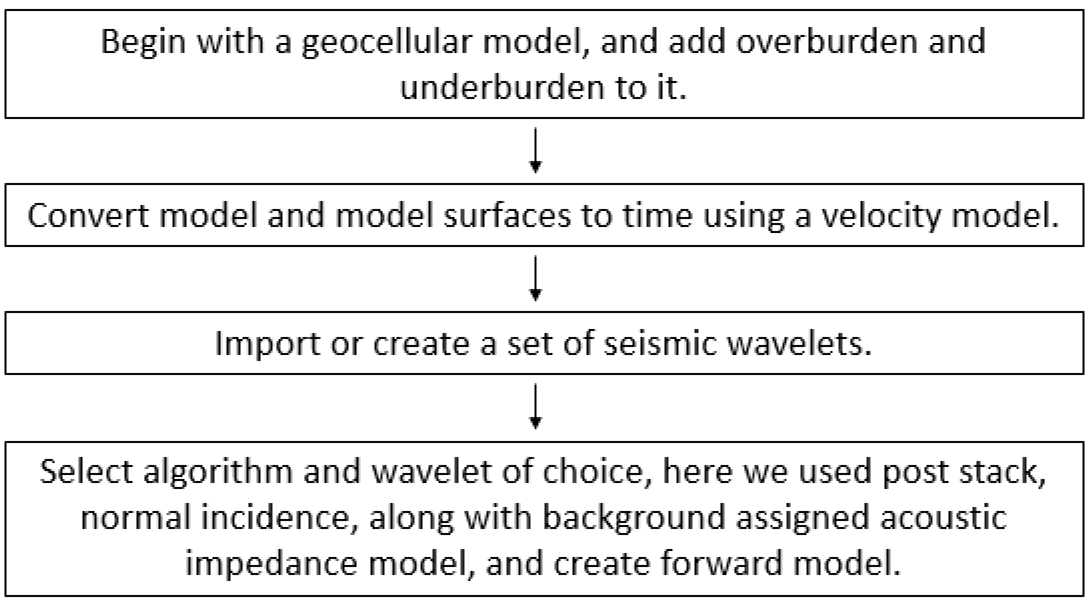

Figure 10. Workflow for creating the forward seismic models.

3.1.3 Inverse modeling method

The 3D seismic models produced in the forward modeling process serve as input for post-stack inversion (Fig. 11). To obtain acoustic impedance, the wavelet is deconvolved, leaving a filtered version of the earth's normal incidence reflectivity, which is related to acoustic impedance by the equation (Russell and Hampson, 1991; Yilmaz, 2001):

$$\mathbf{Z_{t+1}} = \mathbf{Z_t}\left[\frac{1+r_t}{1-r_t}\right] \quad (2)$$

In this equation, $Z_t = p_t V_t$, which is the acoustic impedance of layer t, where p_t = density, and V_t = compressional wave velocity, and layer t overlies layer t +1 (Russell and Hampson, 1991; Yilmaz, 2001). The interface property (i.e. reflectivity) is converted to a rock property (i.e. acoustic impedance). Thus, we can obtain Z_t and Z_{t+1}, the acoustic impedance of layer t and t+1, from the inversion. The post-stack inversion inverts the post-stack seismic amplitude volumes into elastic properties in the seismic grid (i.e., acoustic impedance). The output of each inversion is a 3D acoustic impedance volume.

Inputs for the inversion included a stacked seismic cube, a wavelet, and a prior low frequency model (LFM) cube or constant (Fig. 11). A LFM constant was used which consisted of a prior model cube of P-impedance with a single value of 5.04 kPa.s/m. This choice was simpler than creating a layered low frequency model and it allowed quick creation of the inverse models. Parameters included the signal to noise ratio (SNR), horizontal continuity, tie to low frequency model (LFM), and reflection threshold (Fig. 11). The default values were kept for these variable parameters because this study does not test the sensitivity to these variables.

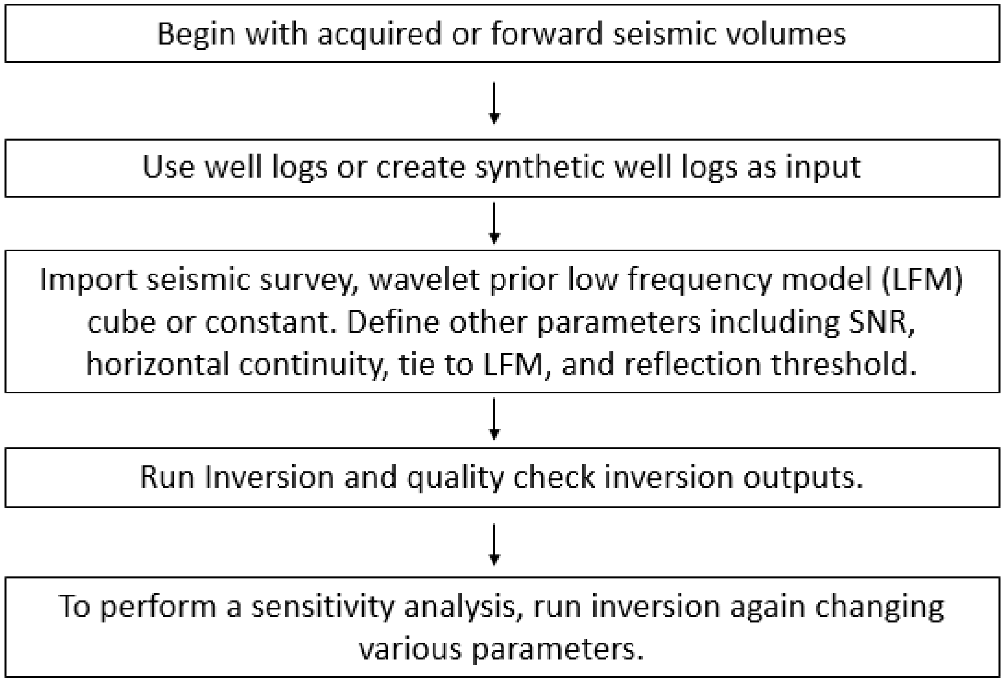

Figure 11. Workflow for creating the 3D inverse models.

3.2 Results

This section presents an overview of the results from the forward and inverse modeling. A comprehensive set of seismic models, including cross sections through 3-D cubes at each frequency for different rock properties, are compiled in Appendices A and B.

3.2.1 Forward Models

Eight forward seismic models were created to analyze the seismic expression of reservoir architecture at different frequencies for deep versus shallow rock properties. These forward seismic models serve as input for the inverse modeling process (Chapter 3.2.2). Five models were created at varying frequencies, 15, 30, 60, 90, and 180 Hz, using the shallow offshore West Africa rock properties, while three additional models were created at varying frequencies, 15, 30, and 60 Hz, using the deep Gulf of Mexico rock properties.

Figure 12 shows seismic models at frequencies of 15, 30, 60, 90, and 180 Hz, with higher resolution at higher frequencies, created using shallow Offshore West Africa rock properties. Figure 12A shows the lowest resolution model of the Laguna Figueroa outcrop, at a dominant frequency of 15 Hz. At 15 Hz channel complex set boundaries are interpretable in the model, but individual channel elements, which have a thickness of 25 m, are not resolvable. Mass transport deposits (MTDs) are also not resolvable.

Individual channel elements can be seen in some areas at 30 Hz (Fig. 12B). It is difficult to interpret overlapping channel elements at this frequency. Channel elements which have an MTD underlying them are the best resolved. MTDs are not easily distinguishable at 15, but at 30 Hz and above, they can be detected as a blue reflector underlying the red-orange reflectors of the channel elements. In seismic reflection data, MTDs commonly have a chaotic response (Posamentier and Kolla, 2003; Armitage and Stright, 2009). At 60 Hz (Fig. 12C), overlapping channel architecture can start to be distinguished. At 90 Hz (Fig. 12D), individual and overlapping channel elements can be more accurately resolved, but it is fairly similar to the 60 Hz result. At least 4 elements can be distinguished here. At 180 Hz (Fig. 12E), fewer reflectors are seen, leaving gray space within the individual channel complexes due to stacked and overlapping channel elements. The lack of definition may make interpretation more challenging.

When evaluating the thickness of architecture from seismic, the thickness that is at theoretical resolution ($\lambda/4$; see Sheriff and Geldart, 1995) is known as the tuning thickness. Above tuning thickness, the apparent thickness interpreted from seismic will always be greater than the true stratigraphic thickness (Pemberton et al., 2018). The true thicknesses of isolated channel elements will be interpretable at their center, maximum thickness (25 m) at 30 Hz and above for shallow rock properties, and at 60 Hz and above for deep rock properties. At these frequencies, the channel element maximum thickness of 25 m is thicker than the tunning thickness (24.4 m at 30 Hz for shallow rock properties and 21.0 m at 60 Hz for deep rock properties; Table 3). At 90 Hz and lower for shallow rock properties, 5 m thick MTDs will be tuned and thus interpreted as thicker than reality in seismic reflection data. For all frequencies tested using deep rock properties (15, 30, and 60 Hz), the MTDs will be tuned (Fig. 12).

Table 3. Tuning thickness for shallow and deep rock properties for channel element axis (CEA) and mass transport deposit (MTD) at frequencies modeled.

Dominant Frequency (Hz)	Tuning Thickness CEA Shallow (m)	Tuning Thickness CEA Deep (m)	Tuning Thickness MTD Shallow (m)	Tuning Thickness MTD Deep (m)
15	48.9	93.3	53.2	83.9
30	24.4	46.7	26.6	42.0
60	12.2	23.3	13.3	21.0
90	8.1	-	8.9	-
180	4.1	-	4.4	-

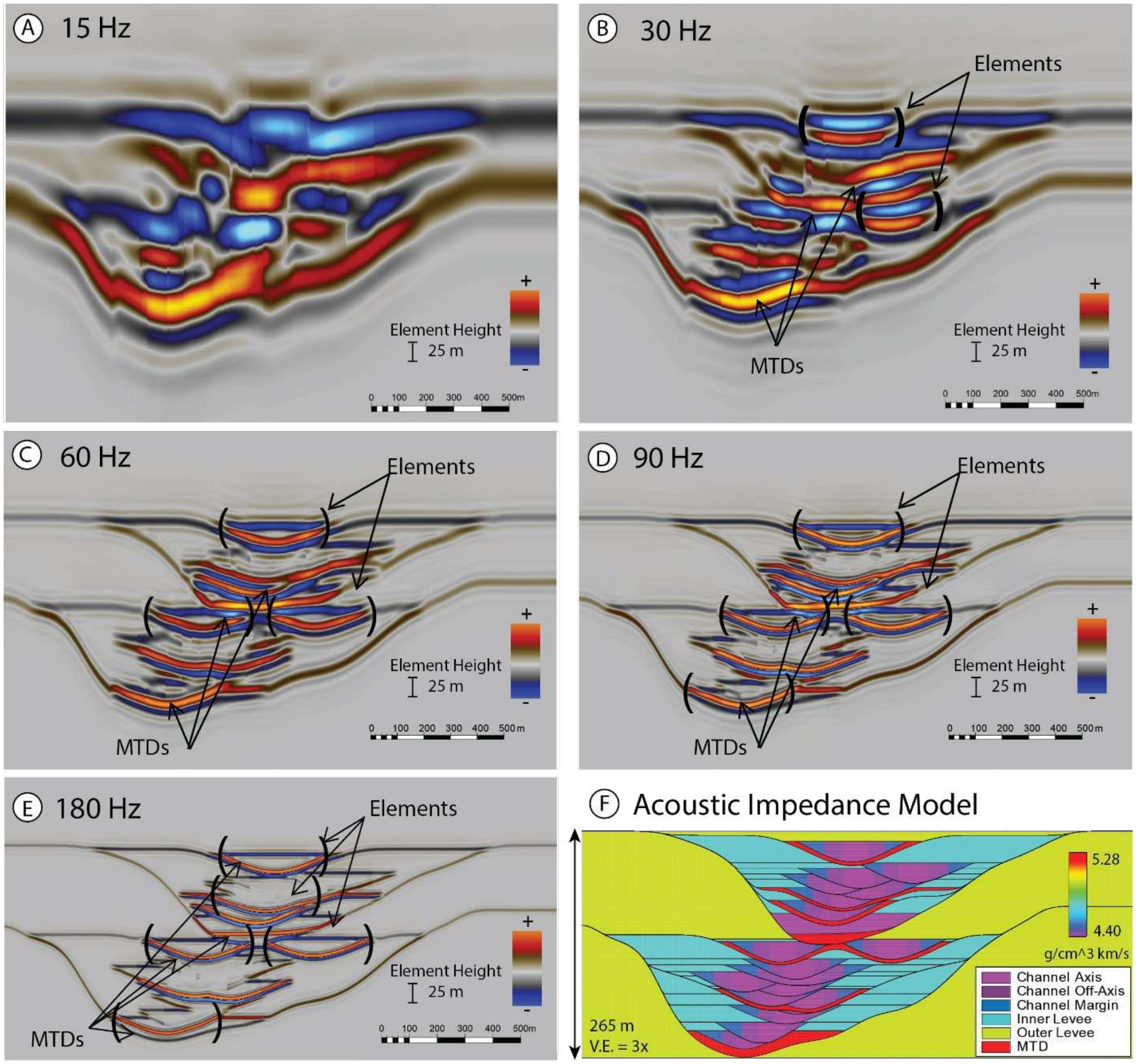

Figure 12. Seismic models at varying frequencies of 15, 30, 60, 90, and 180 Hz, A-E, created using shallow offshore West Africa rock properties.

Figure 13 shows seismic models at frequencies of 15, 30, and 60 Hz, created using deep Gulf of Mexico rock properties. Figure 13A. shows the lowest resolution model of the Laguna Figueroa outcrop, at a dominant frequency of 15 Hz. Individual channel elements are not resolvable at 15 Hz , yet two can be seen at 30 Hz, and at 60 Hz several can be seen. MTDs are not resolvable at 15, however they can be roughly seen at 30 Hz, and three can be seen at 60 Hz.

Overall, the seismic images created using the deep Gulf of Mexico rock properties are of similar but slightly lower quality as the forward models created using shallow offshore West Africa rock properties at the same frequencies.

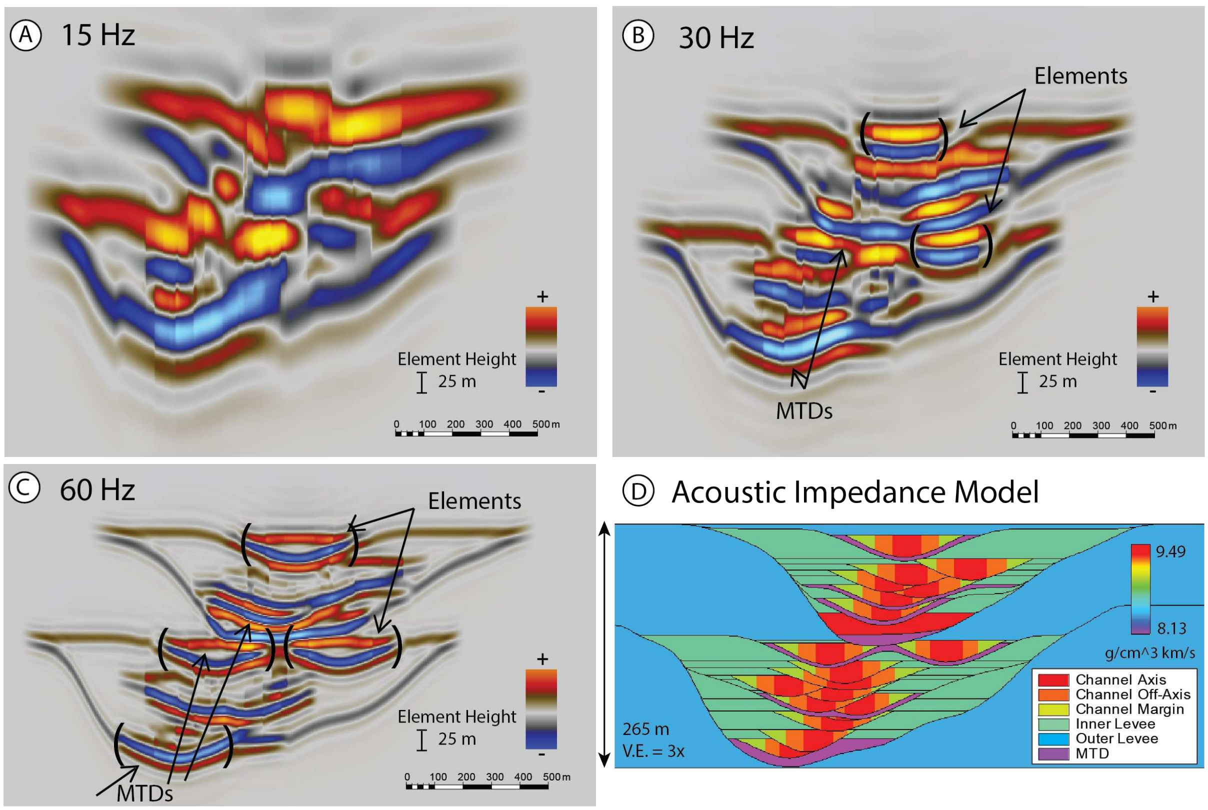

Figure 13. Seismic models at varying frequencies of 15, 30, and 60 Hz, A-C, created using deep Gulf of Mexico rock properties.

Figure 14 provides a side-by-side comparison of each set of rock properties modeled at 30 Hz. One observation is that reflectors showing the same surfaces in each model are the opposite color (Fig. 14). Where there are blue reflectors in the shallow model, they are red in the deep model, known as a polarity reversal. The polarity reversal is a result of hard sandstone having higher impedance than shale (i.e., MTD) in the deep model and soft sandstone having a lower impedance than shale (i.e., MTD) in the shallow model. Overall, the image quality is comparable and would allow for similar interpretations to be made (Fig. 14).

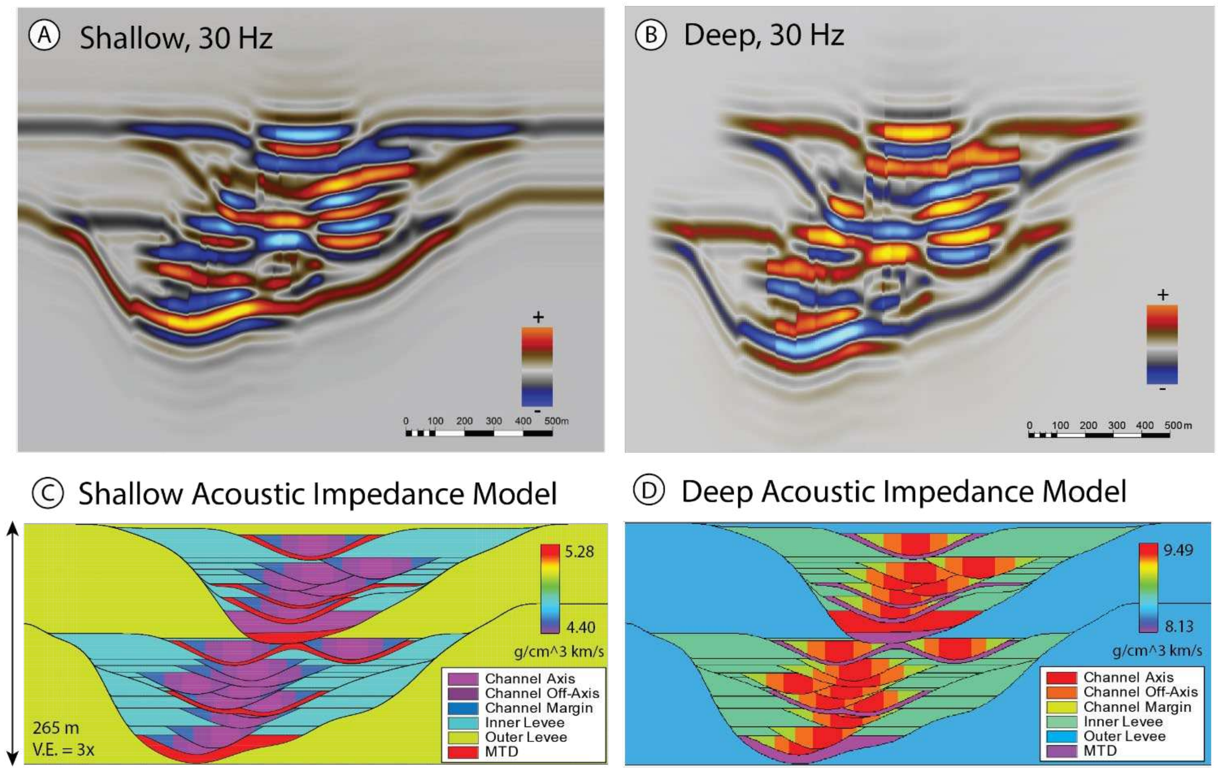

Figure 14. Seismic models at a frequency of 30 Hz, created using A,C) shallow offshore West Africa rock properties and B,D) deep Gulf of Mexico rock properties.

See appendix A for figures with cross sections of the forward models at each frequency.

3.2.2 Inverse Models

Eight inverse models were created from the forward seismic models. Five models were created at varying frequencies, 15, 30, 60, 90, and 180 Hz, using the shallow offshore West Africa rock properties (Fig. 15), while three additional models were created at varying frequencies, 15, 30, and 60 Hz, using the deep Gulf of Mexico rock properties (Fig. 16).

Individual channel elements are not observable in the 15 Hz inverse model (Fig. 15A) and appear thicker than they are due to the results of tuning. They are seen at higher frequencies, 30, 60, 90 and 180 Hz, and with a more accurate thickness, where the effects of tuning lessen (Fig. 15). Channel element axis sandstone has a lower AI relative to the surrounding facies. At 90 and 180 Hz, the channel element axis AI rises compared to lower frequencies, and it looks more similar to the background AI.

MTDs, seen in dark blue, are not interpretable within the 15 Hz inverse model (Fig. 15A), and only two are seen in the 30 Hz model (Fig 15B.), but they gradually become more interpretable with increasing frequency. They are 5m thick and significantly thinner than channel elements, making them hard to detect at low frequencies. At 90 Hz (Fig. 15D) and 180 Hz (Fig. 15E), all MTDs in the model can be seen. They have a higher AI relative to the surrounding facies, making them easily distinguishable

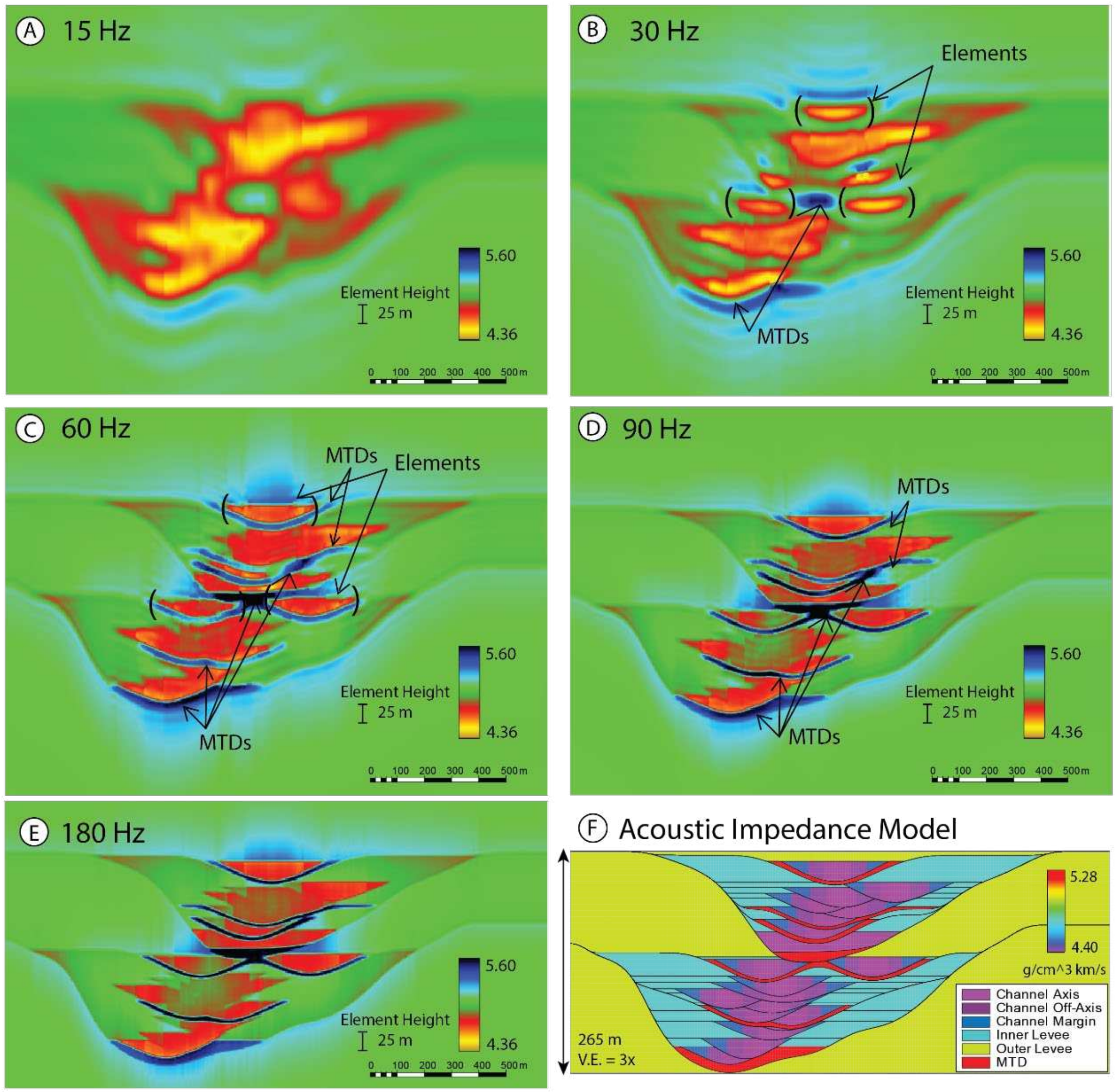

Figure 15. Inverse models at varying frequencies, A-E, using shallow Offshore West Africa rock properties.

Figure 16 shows the inverse model using deep Gulf of Mexico properties. Similar to the shallow rock property 15 Hz inverse model, individual channel elements are not observable, but at 30 Hz and 60 Hz they can be seen. Likewise, MTDs can start to be seen at 30 Hz (Fig. 16B) and are more easily distinguished at 60 Hz (Fig. 16C). Channel complex set surfaces can be seen at all frequencies modeled for both sets of rock properties (Fig. 16). The AI Range for the deep

Gulf of Mexico models is larger than that of the shallow offshore West Africa models. A few vertical, low AI stripes are also seen on the sides of the model and are artifacts from an unknown source, possibly from an issue with the input model (Fig. 16). These were not present in the AI models using the shallow offshore West Africa rock properties, although the same steps were taken to create both sets of models. However, the low AI stripes do not impact the model results and analysis since they are outside of the analysis area.

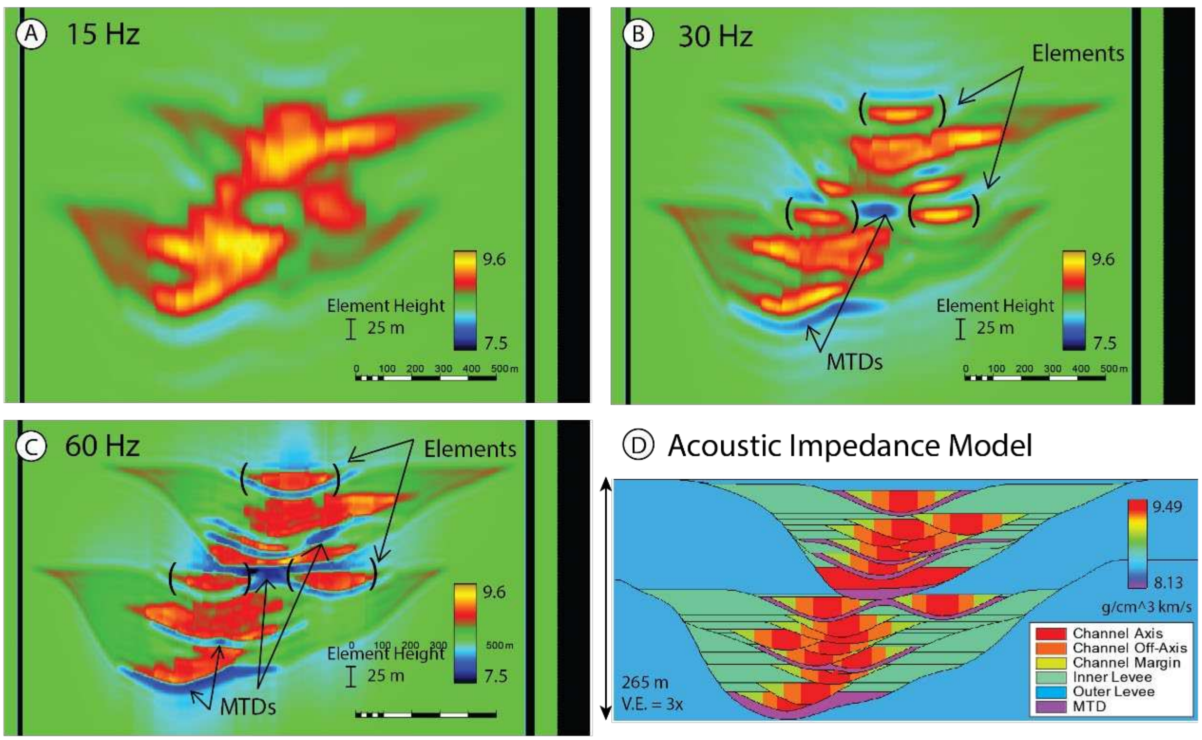

Figure 16. Inverse models at varying frequencies, A-C, using deep Gulf of Mexico rock properties.

Figure 17 provides a side-by-side comparison of each set of rock properties modeled at 30 Hz. Overall, the image quality is similar and would allow for similar interpretations to be made (Fig. 17).

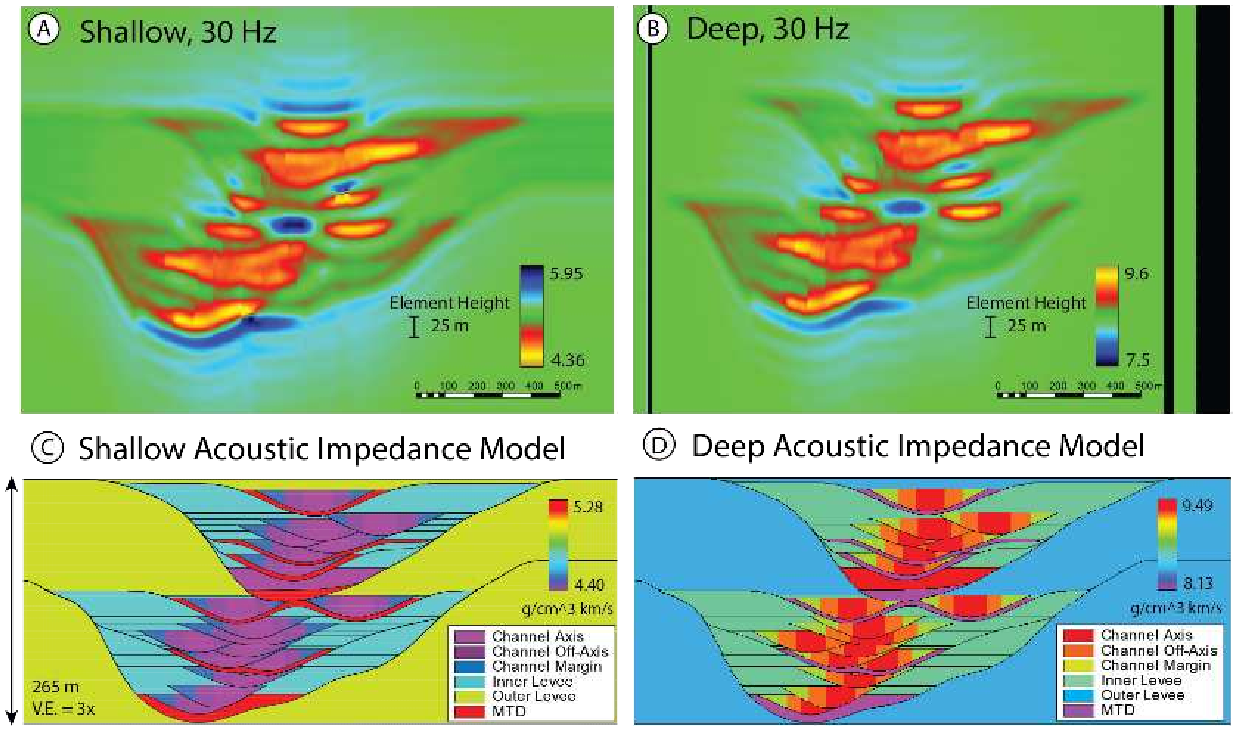

Figure 17. Inverse models at a frequency of 30 Hz, created using A,C) shallow offshore West Africa rock properties and B,D) deep Gulf of Mexico rock properties.

See appendix B for figures with cross sections through the inverse models at each frequency.

3.3 Summary

Eight forward seismic and inverse models were created from the geocellular model. As frequency increased, so did the ability to resolve individual channel elements and MTDs, due to less tuning. Models created using shallow offshore West Africa rock properties had smaller tuning thickness than those created with deep Gulf of Mexico rock properties. These models serve as an important input for facies classification and the finding the probability of correct classification. Understanding what architecture can be interpreted from these models aids in the understanding of prediction models created in the next section.

CHAPTER 4: FACIES CLASSIFICATION

4.1 Methodology

Seismic facies classification from 3D seismic attributes provides a seismic-scale prediction of facies. However, results are rarely validated due to lack of a truth model. Herein the outcrop model serves as a foundation to quantify where and when channel architecture is accurately predicted from facies classification. Seismic facies probabilities are generated with Bayesian classification and correlated with the underlying geologic truth model to test 1) the probability of correct classification overall, and 2) the probability of correct classification as a function of different architectural styles (e.g., channel element stacking patterns).

4.1.1 Bayesian Classification

Bayesian classification (Eq. 3) is performed using a calibration with three synthetic wells derived from the "ground truth" facies model to classify the seismic response from collocated seismic traces (Fig. 18; e.g., Zhu and Journel, 1993; Goovaerts, 1997; Avseth et al., 2005).

$$\boldsymbol{P(A|D) = \frac{P(A)P(D|A)}{P(D)}} \tag{3}$$

In this equation showing the Bayesian classification, *A* = facies (e.g., axis, margin, inner levee, etc.), and *D* = inverted seismic attribute (P-impedance). *P(A)* is the overall probability of encountering facies *A* in the model, or the overall proportion of facies A. *P(D)* is the probability distribution of P-impedance values (Fig. 18). The calibration of facies (*A)* interpreted at the well location to P-impedance at a collocated seismic trace location (*D*) provides a filtered probability distribution function, *P(D)*, where A is present, hence *P(D|A)* (Fig. 18). This calibration is repeated for each defined facies [1,n].

Applying the calibration to the full seismic dataset generates models of the probability of encountering facies away from well locations. Therefore, the calibration is utilized to predict the probability of encountering facies, *A*, for a given value of P-impedance, *D*, resulting in *P(A|D)*. The Bayesian classification results in probability models which can be used to determine the probability of correct vs. incorrect classification.

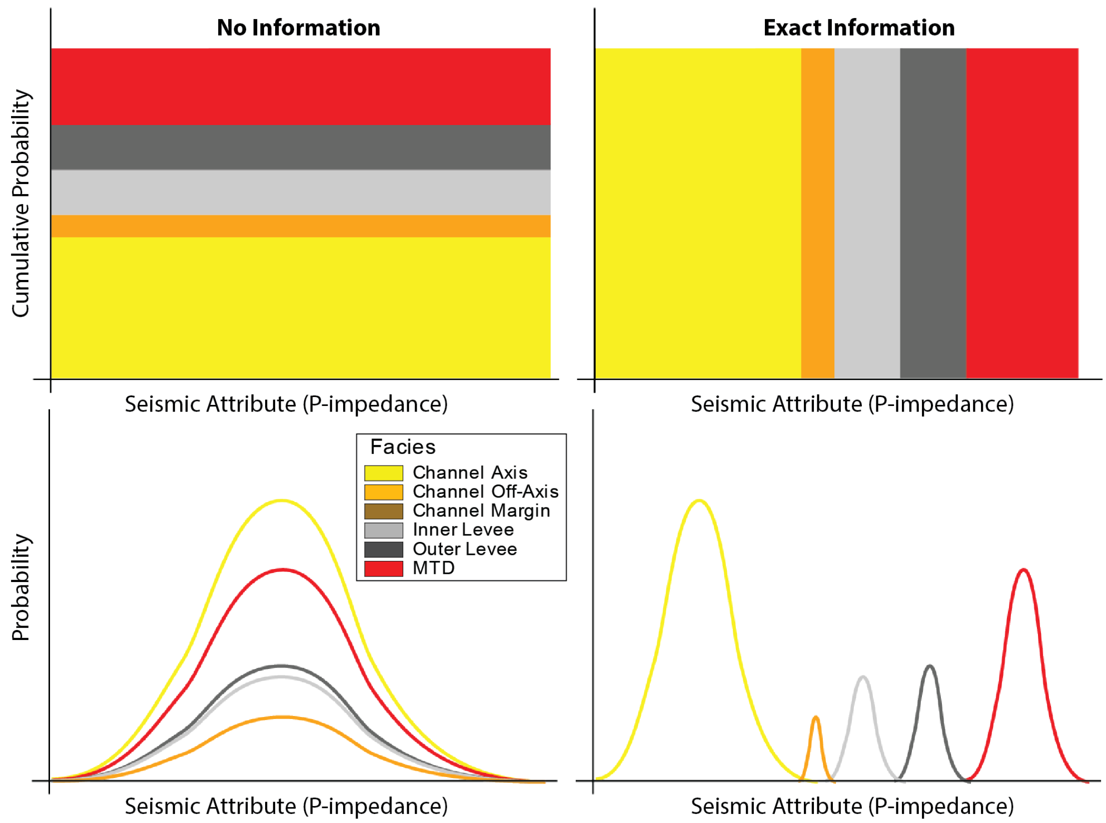

Figure 18. Left: Conceptual diagram showing the probability curves and cumulative probability when no information. The probability is equal to the proportion of facies, so P(A|D) = P(A), and no information is provided from seismic. Classification is based off the global probability or the proportion of facies A. Right: Conceptual diagram showing the probability curves and cumulative probability when there is exact information. P(A|D) = 1. The seismic provides exact information and classification is based off the probability of facies A, which is perfectly calibrated with seismic. (Modified from CSS consortium materials)

4.1.2 Classification Evaluation

The reliability of facies classification from the probability models is tested against the "ground truth" facies model to quantify the probability of correct or incorrect classification overall and for channel element axis sandstone and mass transport deposits (MTDs). The probability of correct classification is evaluated and quantified using the Markov-Bayes calibration coefficient, or herein referred to as the "B value", (Zhu and Journel, 1993; Goovaerts, 1997; Avseth et al., 2005):

$$\boldsymbol{B} = \Delta\boldsymbol{\mu} = \boldsymbol{E}\{\boldsymbol{P}(\boldsymbol{A}|\boldsymbol{D})\} - \boldsymbol{E}\{\boldsymbol{P}(\overline{\boldsymbol{A}}|\boldsymbol{D})\} \tag{4}$$

The B value provides a measure of facies prediction reliability by quantifying the expected value (E) of the probability of correct classification of a facies (e.g., channel element axis sandstone, A=1) from AI (D) minus the expected value of the probability of misclassification of a facies (not channel element axis sandstone, A=0) from AI (D). Simply put, B captures the expected value of a facies being predicted correctly where it exists minus the average value of the facies being predicted where it should not be. When B = 1, the average probability of correct classification is 1, and incorrect classification is 0 (B = 1 – 0, or perfect information) (Fig. 19). When B = 0, on average, the prediction will be right as many times as it is wrong (no information), and when B = -1, the probability of an incorrect classification is 1 (misinformation from D) (Fig. 19). The B value (probability of correct classification) shows how well a seismic attribute (i.e., AI) is able to classify facies.

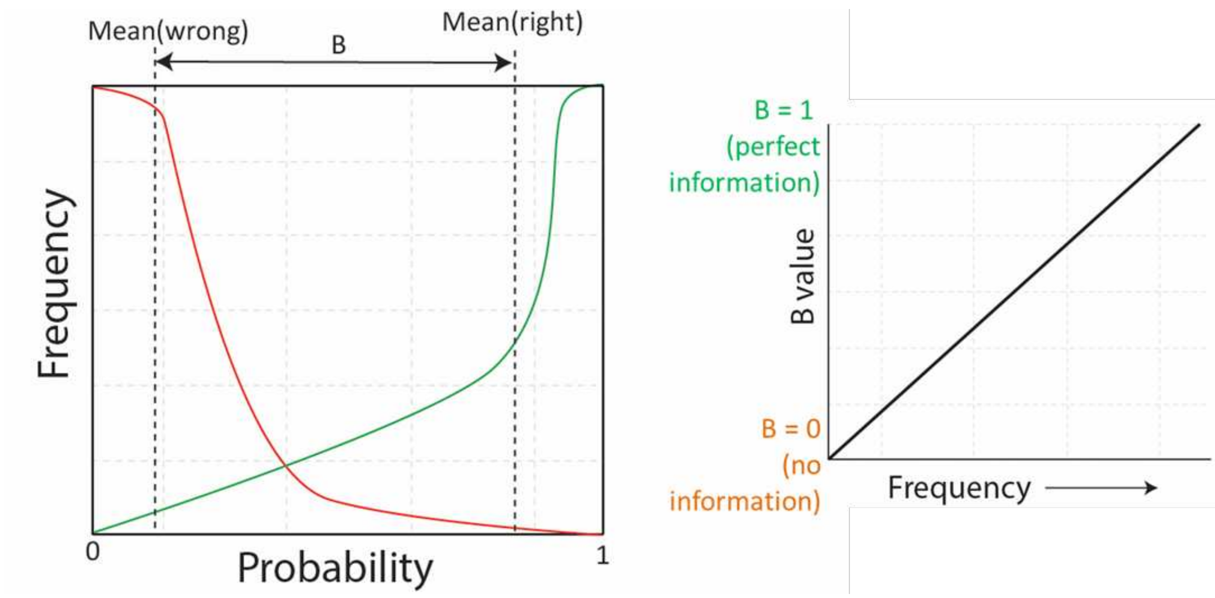

Figure 19. Left: The B value captures the expected value of a facies being predicted correctly where it exists (green line) minus the average value of the facies being predicted where it should not be (red line). Right: When the B value is 0, the seismic provides no information. When the B value is 1, it provides perfect information. With a rise in seismic frequency, a rise in B value was hypothesized. (CSS consortium materials)

4.1.3 Evaluation of Facies by Frequency, Rock Properties and Architecture

The facies classification is evaluated by frequency, rock properties, and architecture. To evaluate the effect of frequency, the facies classification and evaluation was performed on all 8 inverse models. Specifically, the effect of frequency was evaluated at frequencies of 15, 30, 60, 90, and 180 Hz using the shallow offshore West Africa rock properties. Probability models of channel element axis sandstone and MTD facies were evaluated for correct classification due to their importance as reservoir (channel element axis) or flow baffles and barriers (MTD).

Probability models created at 15, 30, and 60 Hz using the deep Gulf of Mexico rock properties were compared to shallow offshore West Africa models at the same frequencies to evaluate the effects of rock properties. The probability of correct classification (B value) provides a quantitative measure to compare the effects of rock properties on facies classification of channel element axis sandstone. MTD facies were not looked at using the deep Gulf of Mexico models. The effect of frequency was also analyzed on these three deep Gulf of Mexico models since they were created at three different frequencies.

The global evaluation gives an indication for overall probability of correct classification (B value) for the entire dataset. We hypothesized that the B value would be a function of architecture, specifically, channel stacking patterns that vary throughout the dataset. However, stacking patterns are difficult to quantify. Jackson et al. (2019) showed that higher NTG was correlated with more vertically aligned (and connected) channel elements and a narrower channel system, thus NTG can be used as a proxy for stacking patterns. To quantify the changes in architecture throughout the dataset, the model was broken into 18 sectors and NTG and channel-to-channel distance were calculated within each sector. The 18 sectors consist of 9 lower channel complex set containers and 9 upper channel complex set containers. Net is the proportion of sand within the sector volume (channel element axis sandstone), and gross is the total volume of the complex set container. Volumes of net and gross were found for each sector to find net to gross per sector. The background outer levee facies were not included in the NTG and B value calculations. Channel-to-channel distance is measured from the centerline at the base of the lowest channel to the next closest channel base, and so on to the top channel in the channel complex set. These two methods provided a way to quantify stacking patterns and thus allowed for quantitative comparison with the B value.

4.2 Results

This section presents an overview of the results from the Bayesian classification and the classification evaluation. The classification evaluation is further sectioned into 1) facies by frequency and rock properties and 2) architecture by channel element stacking pattern.

4.2.1 Bayesian Classification

The Bayesian classification used a calibration with three synthetic wells derived from the "ground truth" facies model to classify the seismic response from collocated seismic traces (Fig. 20). The three wells were placed in the north, south, and middle of the channel system. The calibration is utilized to predict the probability of encountering facies, *A*, for a given P-impedance value, *D,* for example shown in blue-green on Figure 20, resulting in *P(A|D)*, shown by a black box on the upper right side of Figure 20. For this example, the probability of encountering sand is higher than the probability of encountering any other facies, given this P-impedance (Fig. 20).

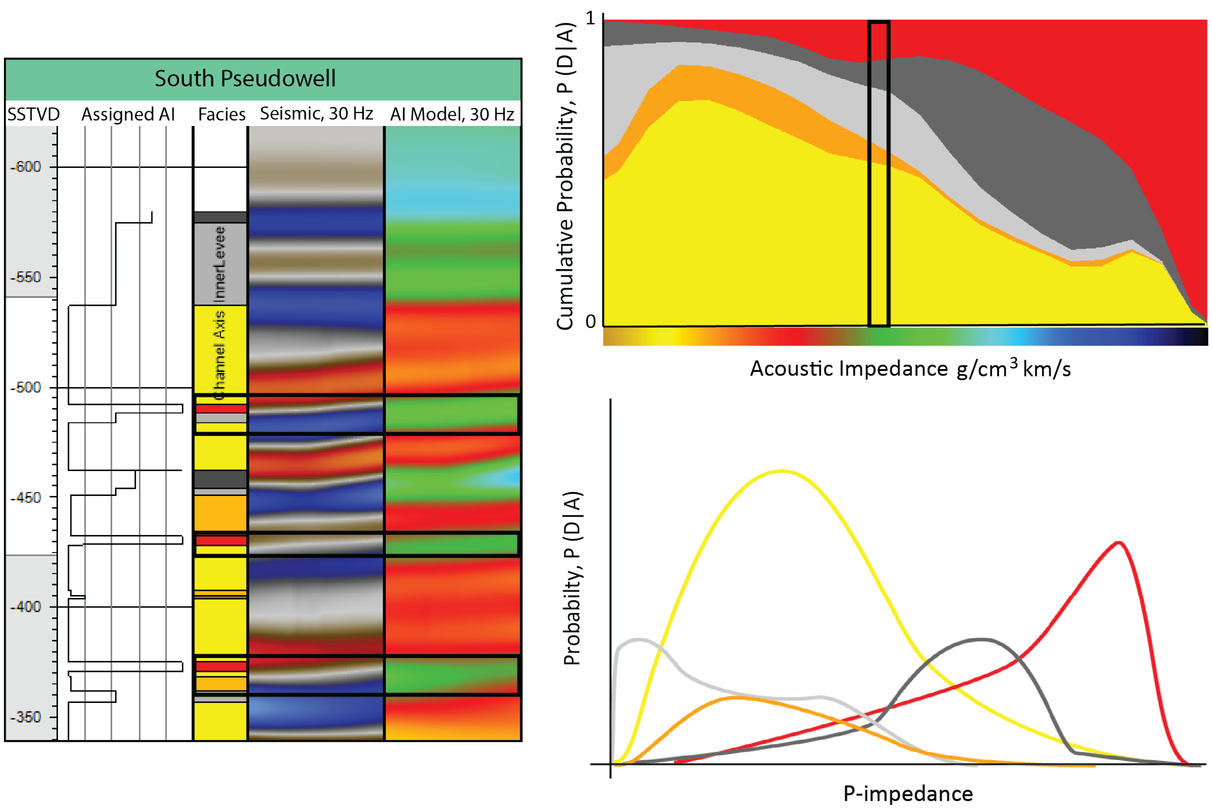

Figure 20. Left: Well logs at the south pseudowell showing assigned AI, facies, the seismic model at 30 Hz using offshore West Africa rock properties, and the AI model at 30 Hz. Black boxes show where the AI in the well correlates with AI in the cumulative probability distribution. Upper Right: Cumulative probability, P(A|D), from the well to seismic calibration. Lower Right: Probability curves, P(A|D), from the well to seismic calibration. Channel element axis sandstone and mass transport deposits (MTDs) have the highest P(A|D). (Modified from CSS consortium materials)

This classification provides a filtered probability distribution function, *P(D)*, where A is present, hence *P(D|A)* at all points in the model, allowing prediction of AI values away from the well location. This results in a probability model for each of the 6 facies (Fig. 21). Channel element axis sand and MTD facies had the highest probabilities, near one in some parts of the probability models (Fig. 21). The other four facies, channel off-axis, channel margin, inner levee, and outer levee, had low probabilities, near 0 in some cases. The classification probability models were evaluated using the B value, and results are described in the next section.

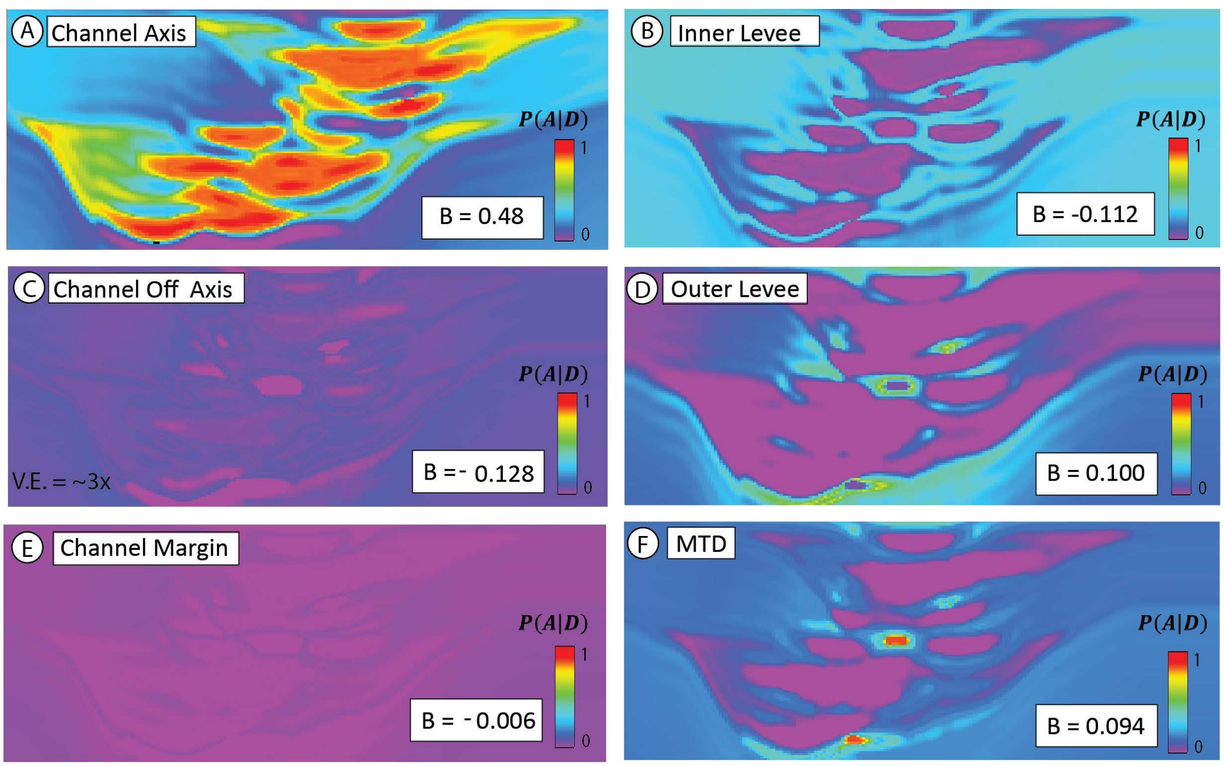

Figure 21. Probability models for each facies from Bayesian classification with three calibration wells. The calculated B value for each facies is shown, using shallow rock properties. Negative B values result when the average probability of incorrect classification is great then the probability of correct classification.

4.2.2 Classification Evaluation

The classification evaluation shows that channel element axis sandstone and MTD facies have the highest probability of correct classification (i.e., B value; Fig. 21). The other four facies have low B values, as expected from the low probabilities shown throughout the models overall and are not further discussed (Fig. 21). Figure 22 shows the Bayesian classification results and the corresponding B values. Figure 22A shows the location of one of the three pseudowells used in the model. Figure 22B provides an example showing channel element axis sandstone probability, *P(A|D)*, where A is channel element axis sandstone and D is P-impedance at a collocated seismic trace location, from Bayesian classification. The mean value of the probability of correct prediction (Fig. 22C) minus the mean value of the probability of incorrect prediction (Fig. 22D), provides the probability of correct classification, also called the B value. The classification was evaluated by frequency, rock properties, and architecture using stacking patterns.

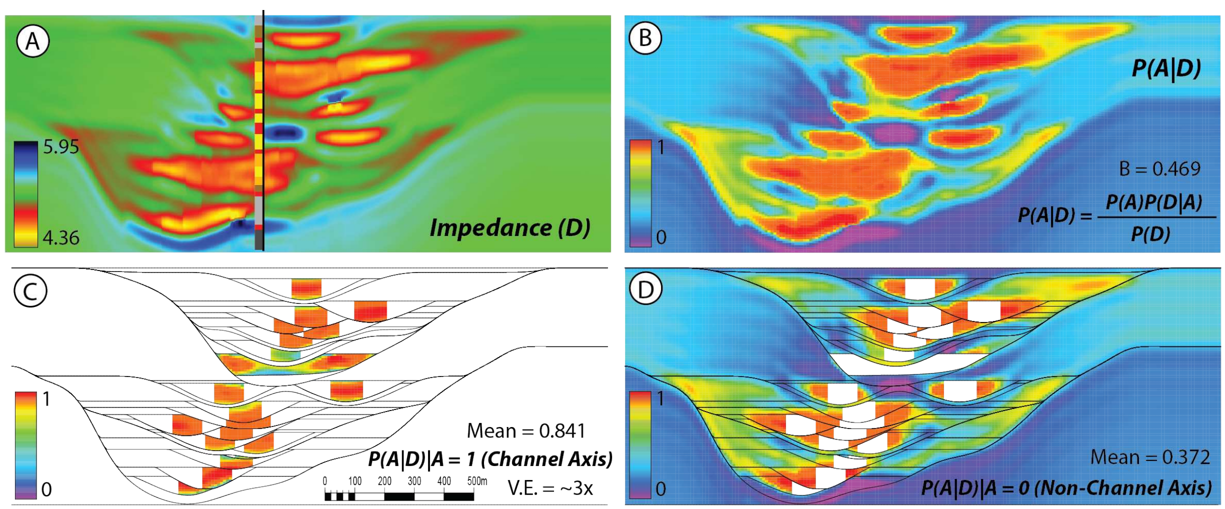

Figure 22. Facies classification and analysis that starts with an A) inversion model and synthetic well used in calibration for Bayesian classification that produces B) channel element axis sandstone probability, P(A|D), where A is channel element axis sandstone and D is AI, from Bayesian classification. This model (B) has a B value (probability of correct classification) of 0.469 resulting from the difference of the mean value of the probability of correct prediction (shown in C) and the mean value of the probability of incorrect prediction (shown in D).

4.2.2.1 Facies by Frequency and Rock Properties

The classification response to seismic frequency and rock properties is examined. Probability models were produced using Bayesian classification for each of the six facies in the model and for all frequencies and rock properties (e.g., shallow OWA, 30Hz; Fig. 21). Of these six facies, channel element axis sandstone and MTD facies were evaluated for correct classification. Facies classification is evaluated by frequency using shallow rock properties and then by rock properties (e.g., shallow vs. deep). Sensitivity to seismic frequency is tested using frequencies of 15, 30, 60, 90, and 180 Hz and the model created using shallow rock properties. Various seismic frequencies are available in industry, depending on the stage of the project. With increasing frequency, probability of correct classification (B value) increased for channel element axis sandstone (Figs. 23 and 24). Likewise, probability of correct classification (B value) increased for MTDs with increasing frequency (Figs. 23 and 25).

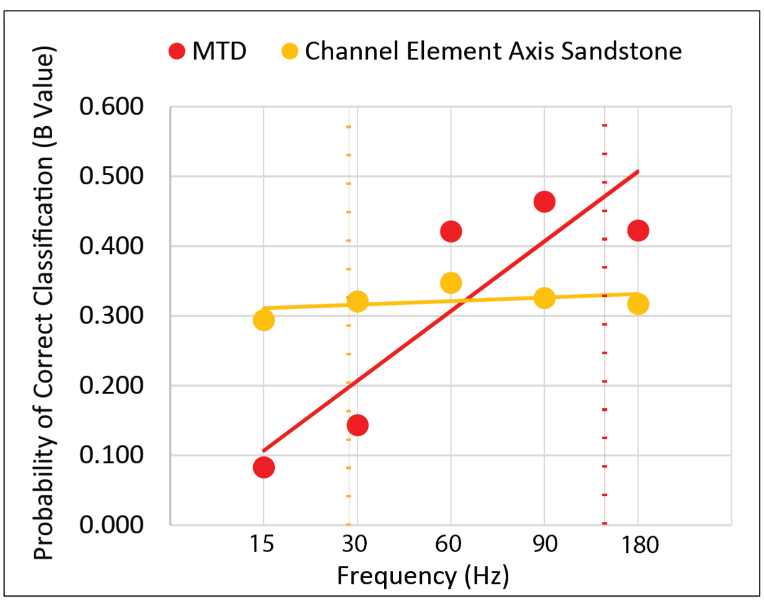

Figure 23. Channel element axis sandstone B value (probability of correct classification) increases gradually up to 60 Hz, then decreases gradually with increasing frequency, while B value (probability of correct classification) increases steeply for MTDs. Channel element axis sandstone is tuned at frequencies below the dashed yellow line. MTDs are tuned at frequencies below the dashed red line.

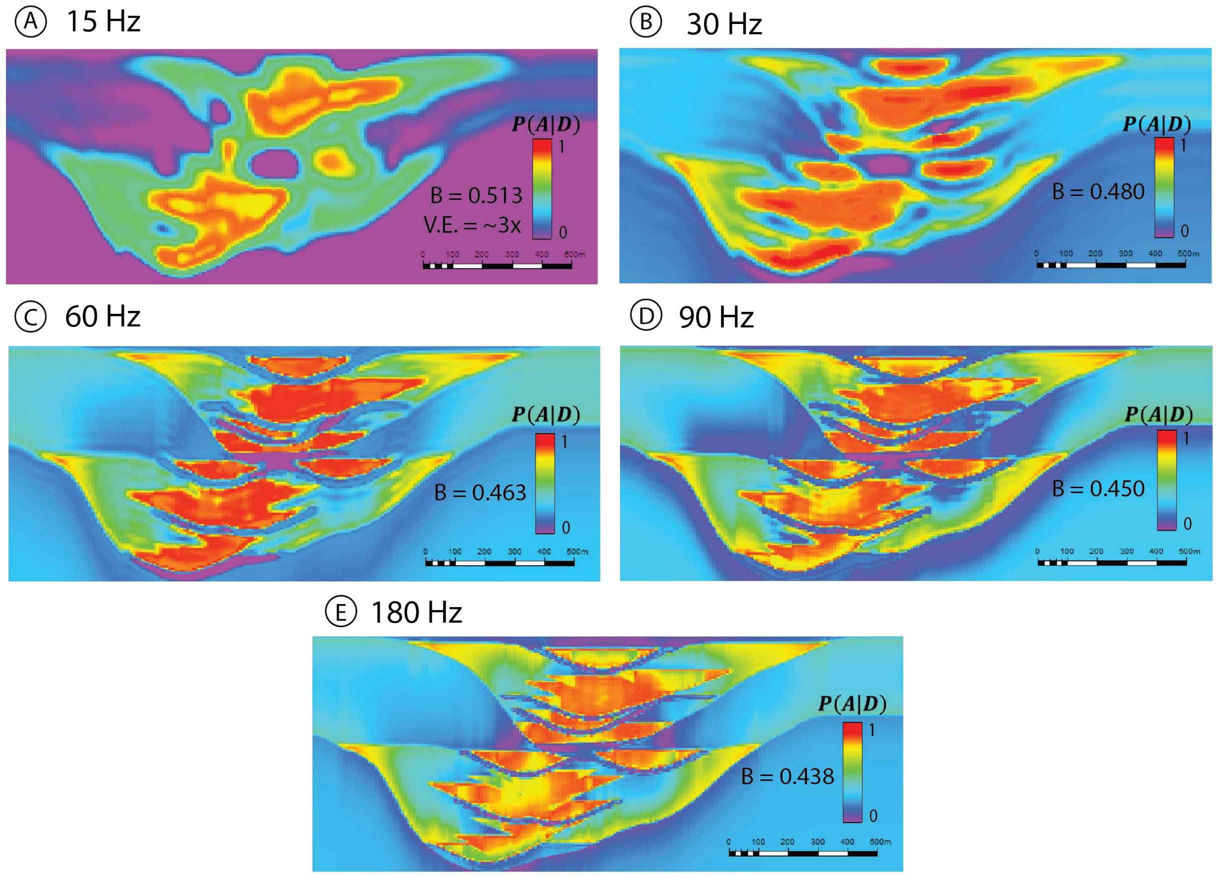

Figure 24. Probability models for channel element axis at each frequency, A-E, from Bayesian classification with three calibration wells. The calculated B value for each model is shown, using shallow rock properties. Channel element axis sandstone B value (probability of correct classification) decreases with increasing frequency.

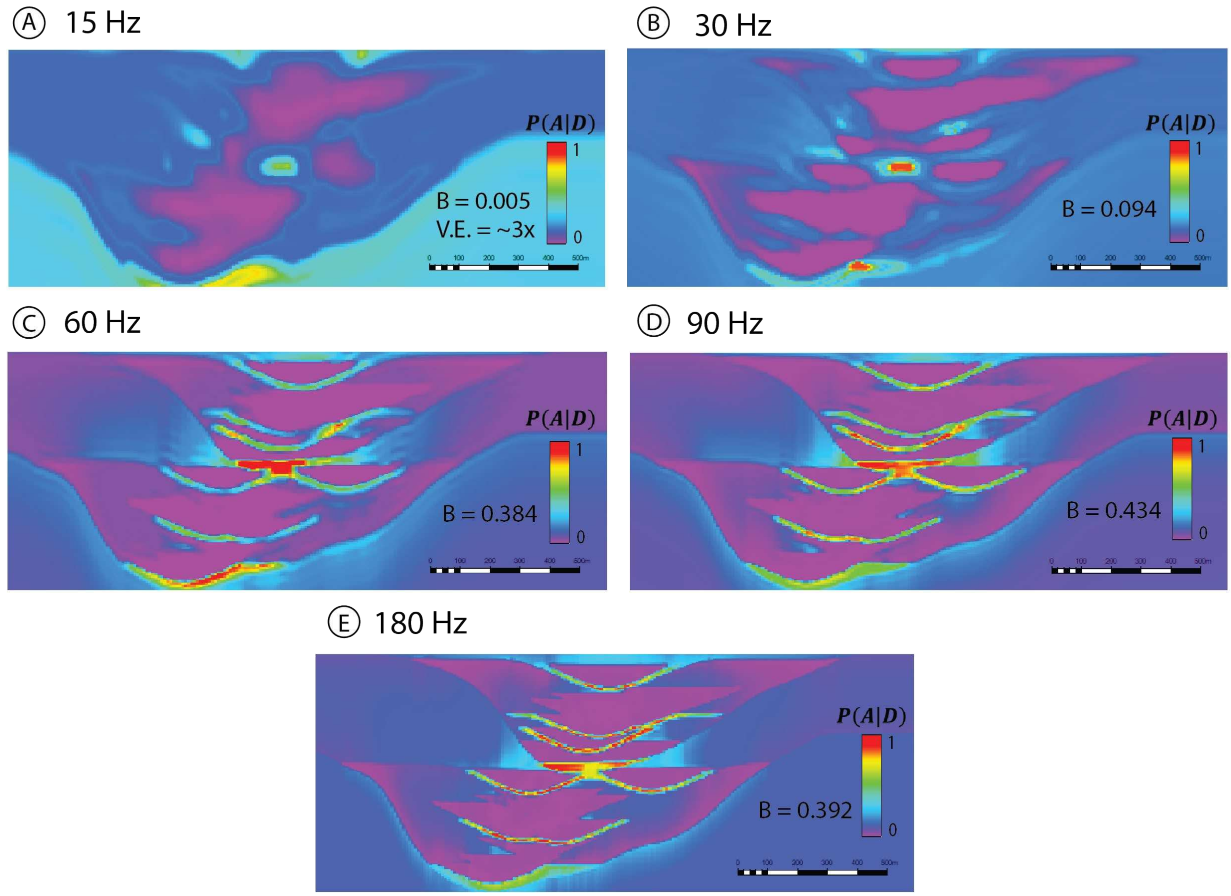

Figure 25. Mass transport deposit (MTD) probability models at each frequency, A-E, from Bayesian classification with three calibration wells. The calculated B value for each model is shown, using shallow rock properties. MTD B value (probability of correct classification) increases with increasing frequency.

Three additional models were created at varying frequencies of 15, 30, and 60 Hz using the deep Gulf of Mexico rock properties (Fig. 26). The facies classifications of these models were compared to the shallow Offshore West Africa rock properties at 15, 30, and 60 Hz (Fig. 26). When comparing shallow offshore West Africa rock properties and deep Gulf of Mexico rock properties, the probability of correct classification (B value) is higher for deep rock properties than shallow rock properties at all frequencies compared (Figs. 27 and 28). This result was counterintuitive but may result from the fact that the deep rock properties have a wider AI range than the shallow rock properties. At deeper depths, compaction has a greater effect on the rocks, and sand becomes more compacted and less porous than shale due to cementation (Regenauer-Lieb et al., 2018). This is likely why the deep rock properties have a wider AI range than the shallow rock properties.

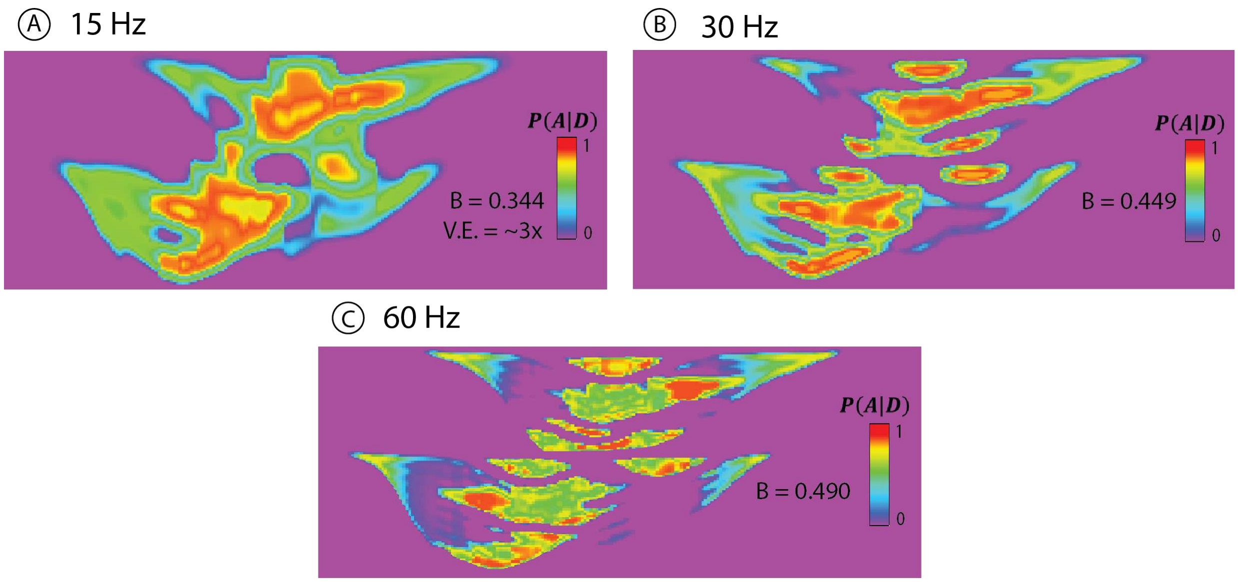

Figure 26. Probability models for channel element axis sandstone at each frequency, A-C, from Bayesian classification with three calibration wells. Rock properties used are from the deep Gulf of Mexico. The calculated B value for each facies is shown, using deep rock properties. Probability of correct classification (B value) increases with increasing frequency.

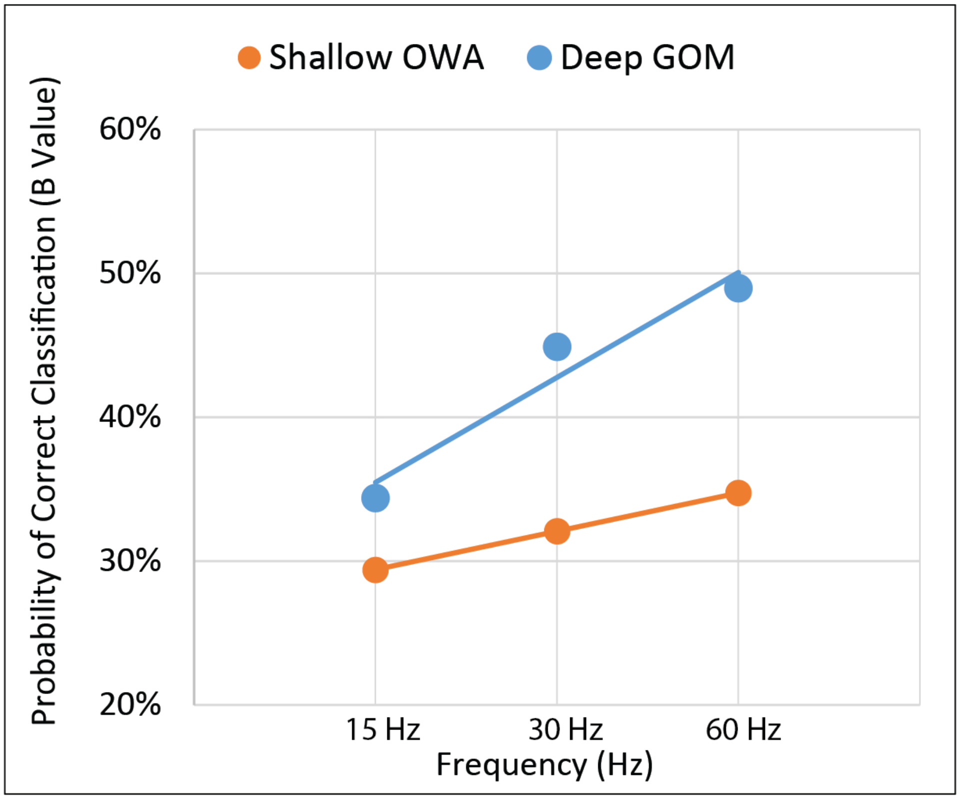

Figure 27. Probability of correct classification (B value) is higher at frequencies modeled, 15, 30, and 60 Hz, for Deep GOM rock properties in comparison with Shallow OWA rock properties.

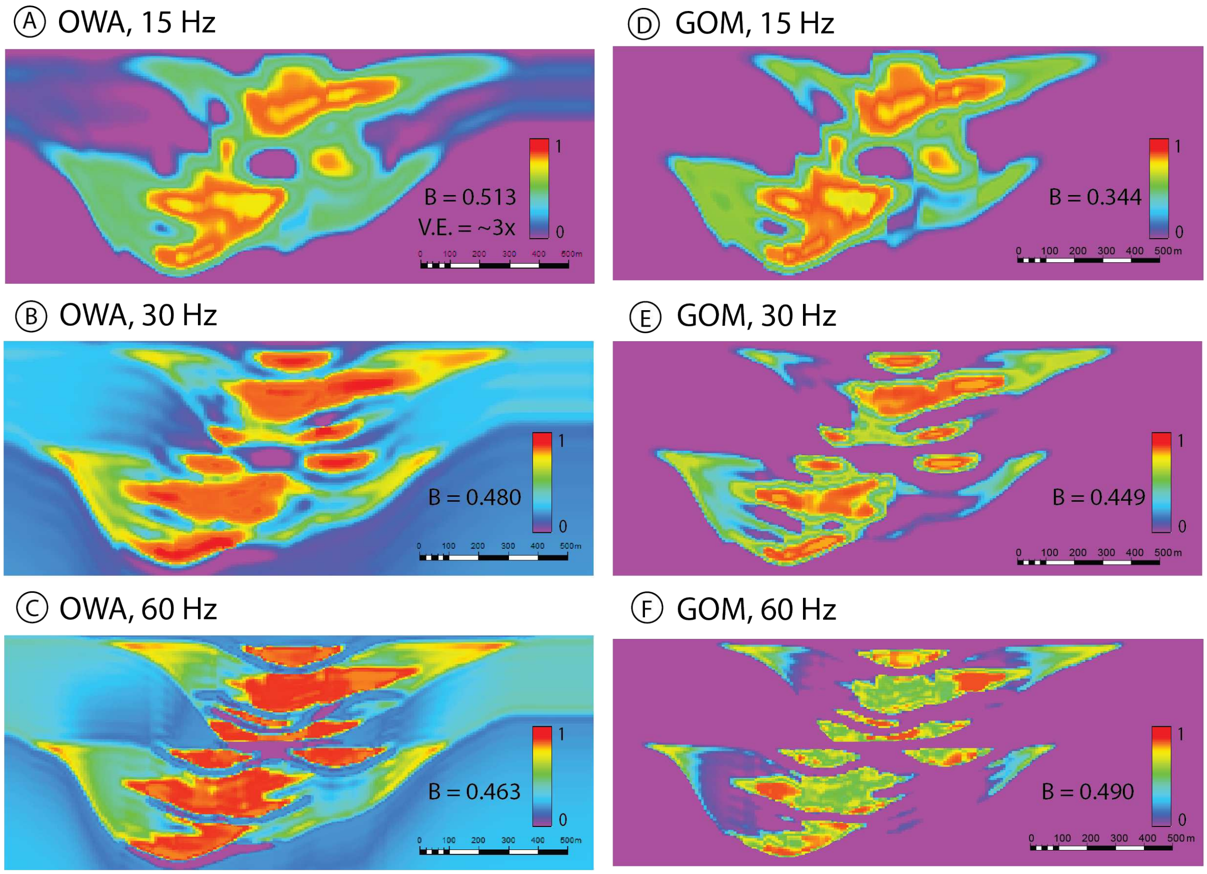

Figure 28. Probability models for channel element axis from Bayesian classification with three calibration wells. The calculated B value is shown, at varying frequencies, A-C, using shallow offshore West Africa rock properties and D-F using deep rock properties from the Gulf of Mexico. Probability of correct classification (B value) is higher for facies classification of models using deep rock properties from the Gulf of Mexico compared to models using shallow rock properties from offshore West Africa.

4.2.2.2 Architecture by Channel Element Stacking Pattern

Classification is evaluated by architecture using channel element stacking patterns. The hypothesis is that interference from successively stacked channel elements reduces channel element sandstone axis imaging due to the loss of AI contrast. The hypothesis is tested by evaluating stacking patterns using 1) NTG within channel complex set containers as a proxy for stacking (i.e., high NTG represents vertically aligned/stacked channel elements and low NTG represents channel elements that are spread out), and 2) the cumulative distance between stacked channel elements. To do so, the model is broken up into eighteen sectors, representing upper and lower channel complex set containers, and NTG within channel complex set containers is evaluated by sector (Fig. 29).

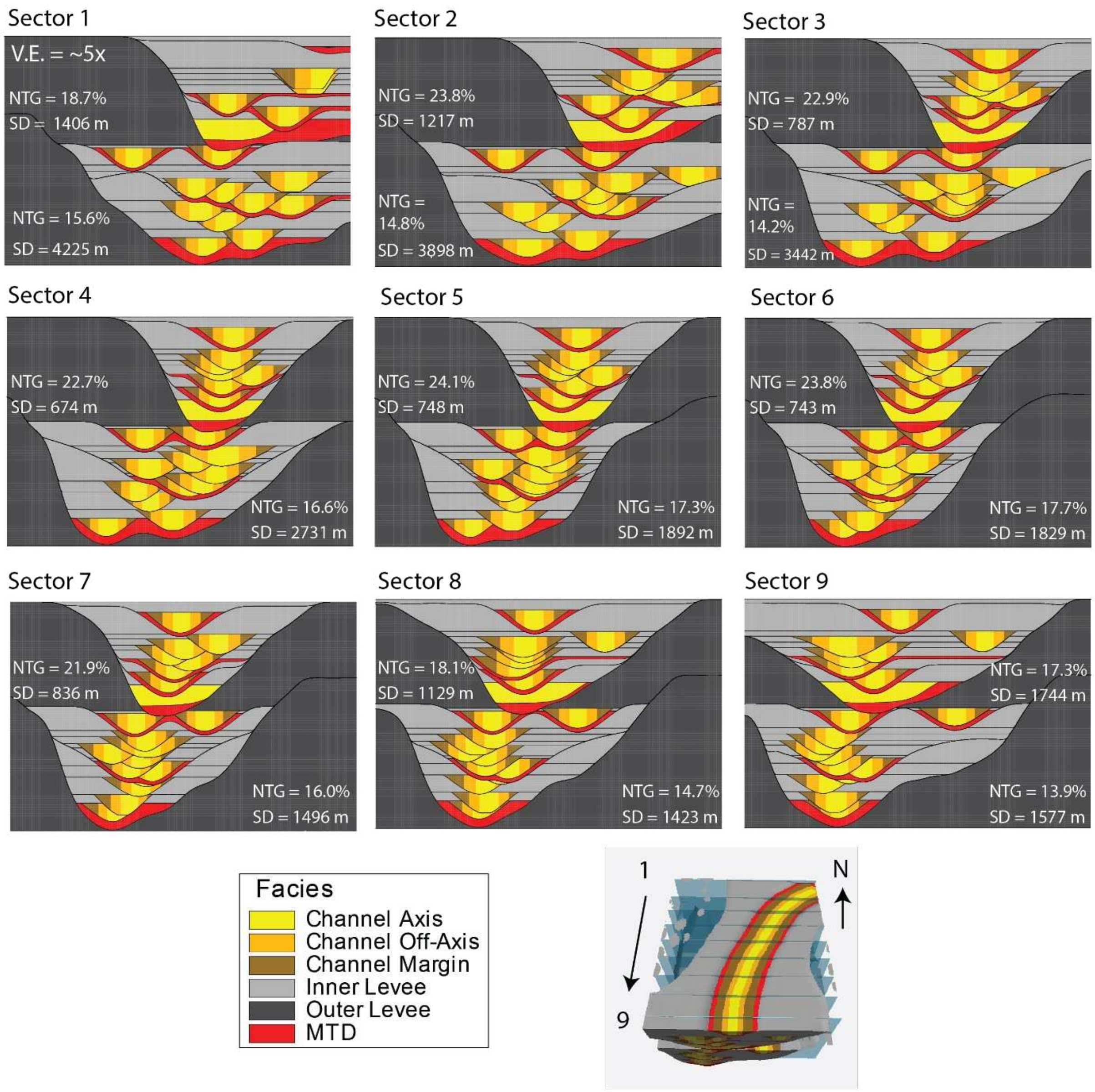

Figure 29. North to South cross section sectors through the facies model showing an array of stacking patterns present. Each of the nine sectors is further broken apart into two sectors, one for the upper channel complex set, and one for the lower channel complex set, resulting in eighteen sectors overall representing channel complex set containers at 9 cross-sections through the model. Net-to-gross (NTG) and stacking distance (SD) are labeled by sector.

Using NTG as a proxy for stacking, organized stacking patterns correlate with higher NTG, while disorganized stack patterns correlate with lower NTG (Fig. 30). This supports the hypothesis that interference from successively stacked channel elements (i.e., high NTG, reduces channel sandstone axis imaging due to the loss of AI contrast). This is true for models using both sets of rock properties (Fig. 31).

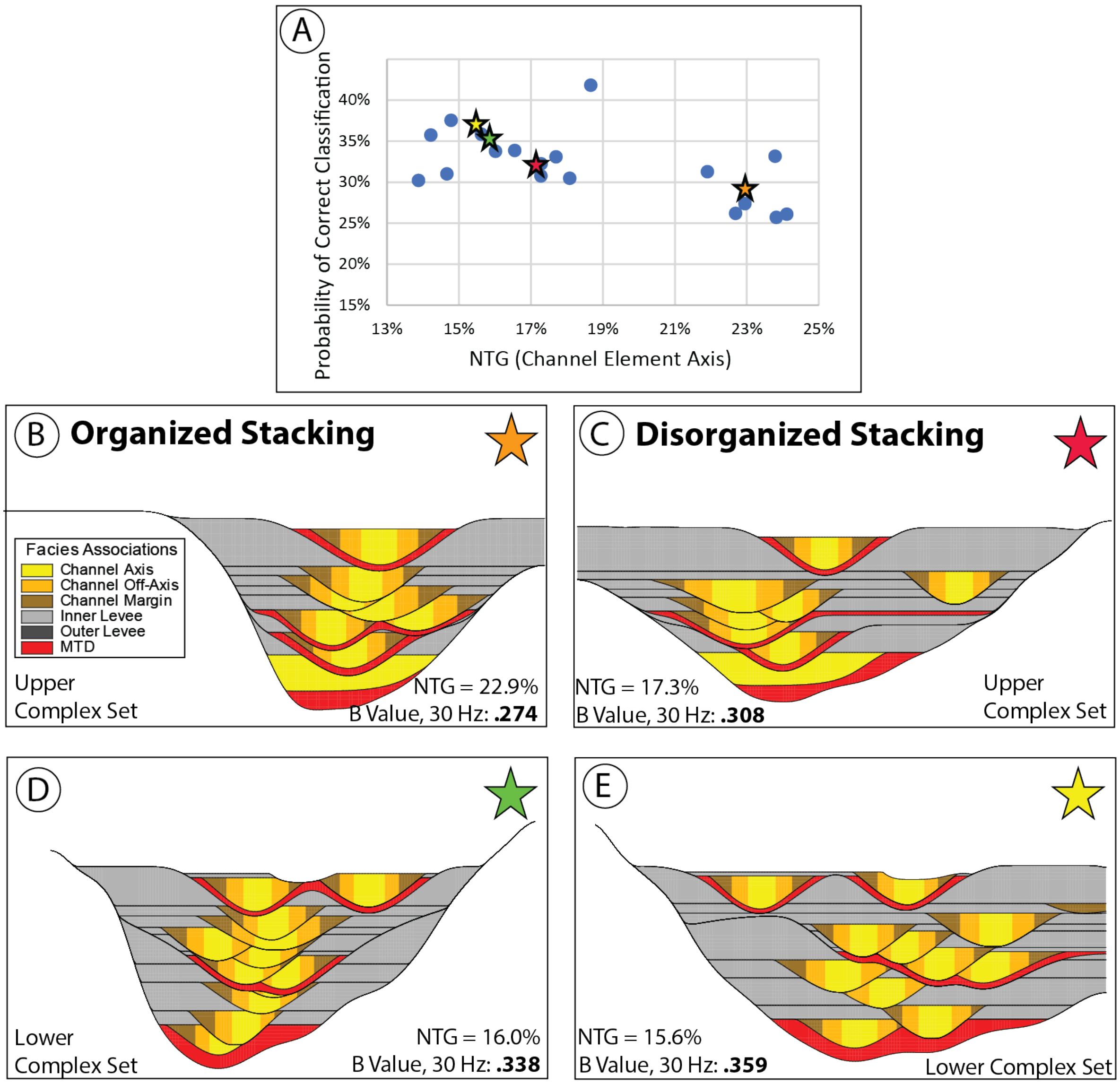

Figure 30. A) Plot of probability of correct classification (B value) vs. NTG where net is defined as the channel element axis sandstone. Organized stacking patterns (B,D) show lower B values than disorganized stacking patterns (C,E).

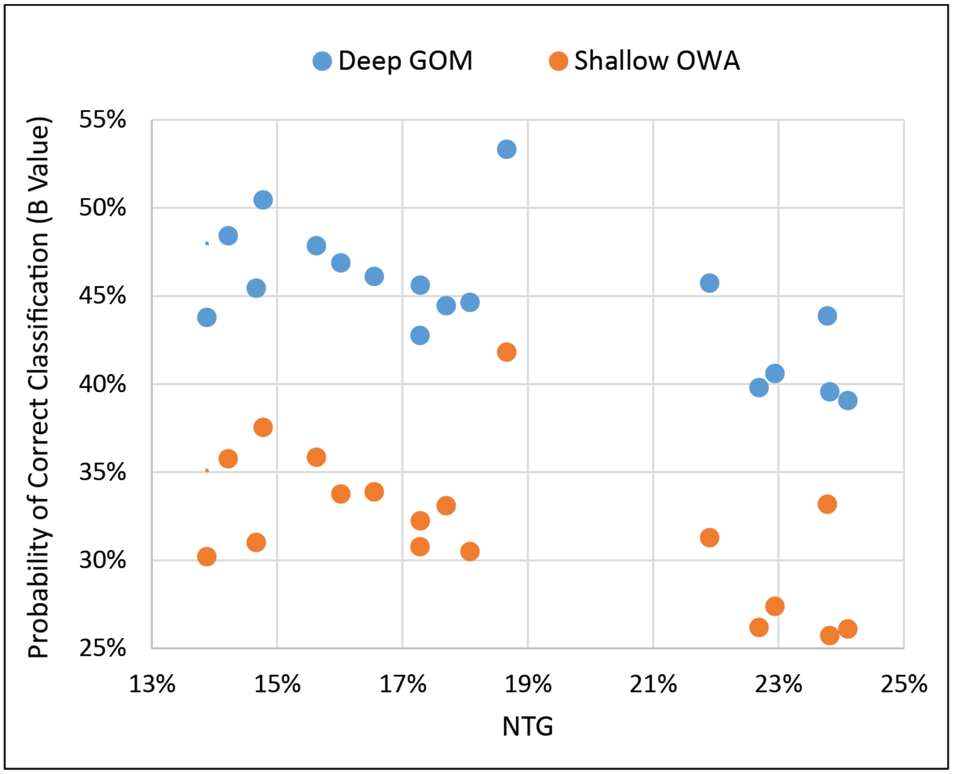

Figure 31. B value (probability of correct classification) for channel element axis sandstone decreases as net-to-gross (NTG) increases for each of the 18 sectors (30 Hz models) using both sets of rock properties, showing how predictability is stronger when channel elements are isolated in background facies.

Another way to capture stacking patterns is through the cumulative distance between successively stacked channel elements or stacking distance (Fig. 32). Stacking distance and NTG have a negative association (Fig. 33). Channel complex sets with a short stacking distance were organized or vertically aligned (higher NTG), whereas a longer stacking distance meant the channel elements were more disorganized or laterally spread out (lower NTG). Probability of correct classification (B value) was found to be higher for disorganized stacking patterns, which had a lower NTG and a longer stacking distance, compared to organized stacking patterns, which had a higher NTG and a shorter stacking distance (Fig. 32). Disorganized stacking patterns isolate channel elements within background levee facies, allowing for better imaging of top and base of sandstone, and thus more accurate prediction.

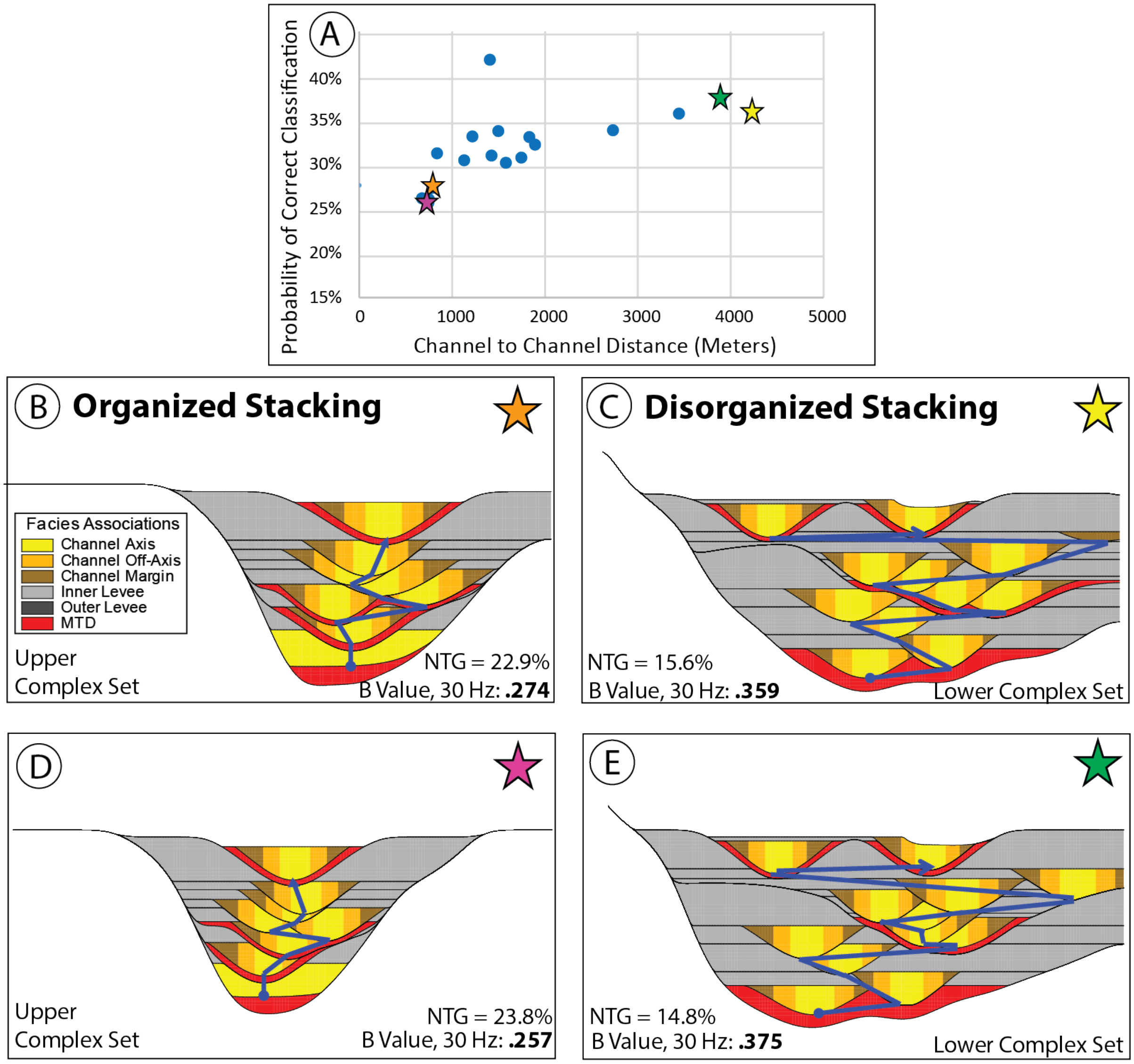

Figure 32. A) Plot of probability of correct classification (B value) vs. channel-to-channel stacking distance. Organized stacking patterns with shorter channel-to-channel stacking distance (B, D) show lower B values than disorganized stacking patterns with longer channel-to-channel stacking distance (C, E), similar to net-to-gross (NTG) results in Fig. 30.

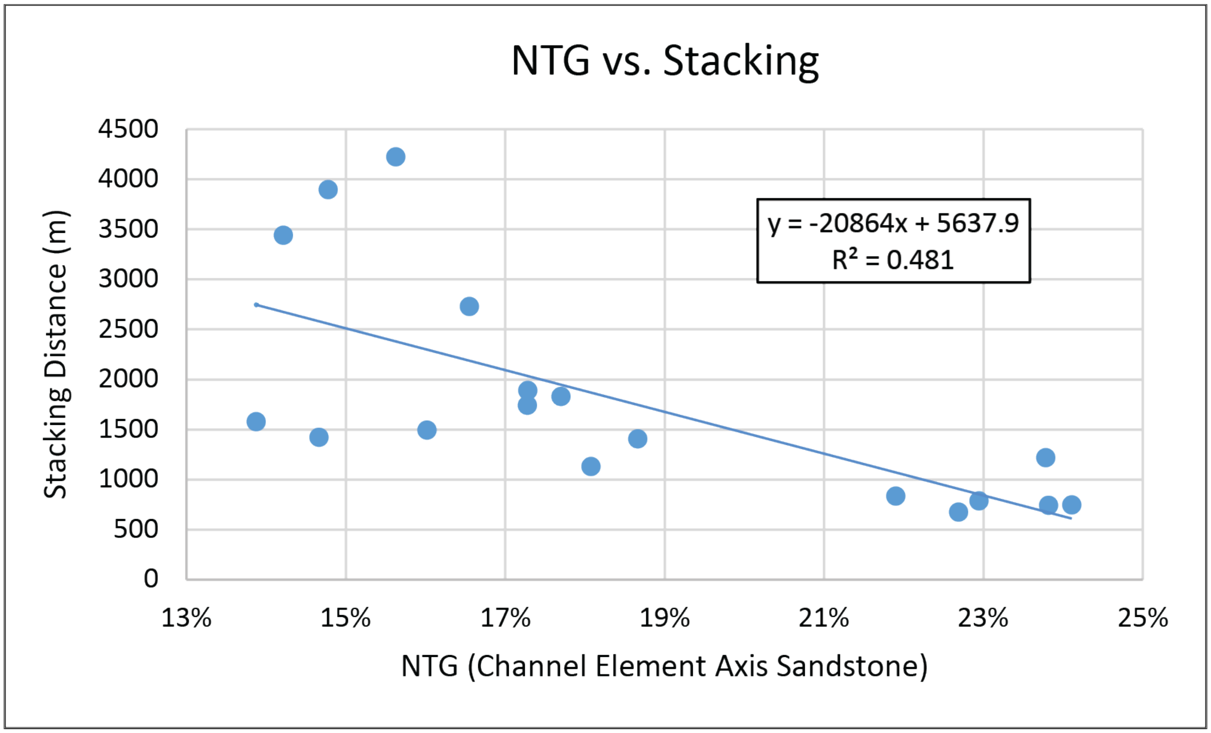

Figure 33. Net-to-gross (NTG) vs stacking distance values for each of the 18 sectors. They are negatively correlated with an R^2 value of 0.481.

Plotting the B values at each of the 5 frequencies tested for channel element axis sandstone using OWA rock properties vs NTG provides further insight (Fig. 34). B values decrease most sharply with increasing NTG at 15 Hz, while also decreasing at 30, 60, and 90 Hz. At 180 Hz, B values increase slightly. Thus NTG is seen to have the largest impact on the 15 Hz model and the least impact on the 180 Hz model.

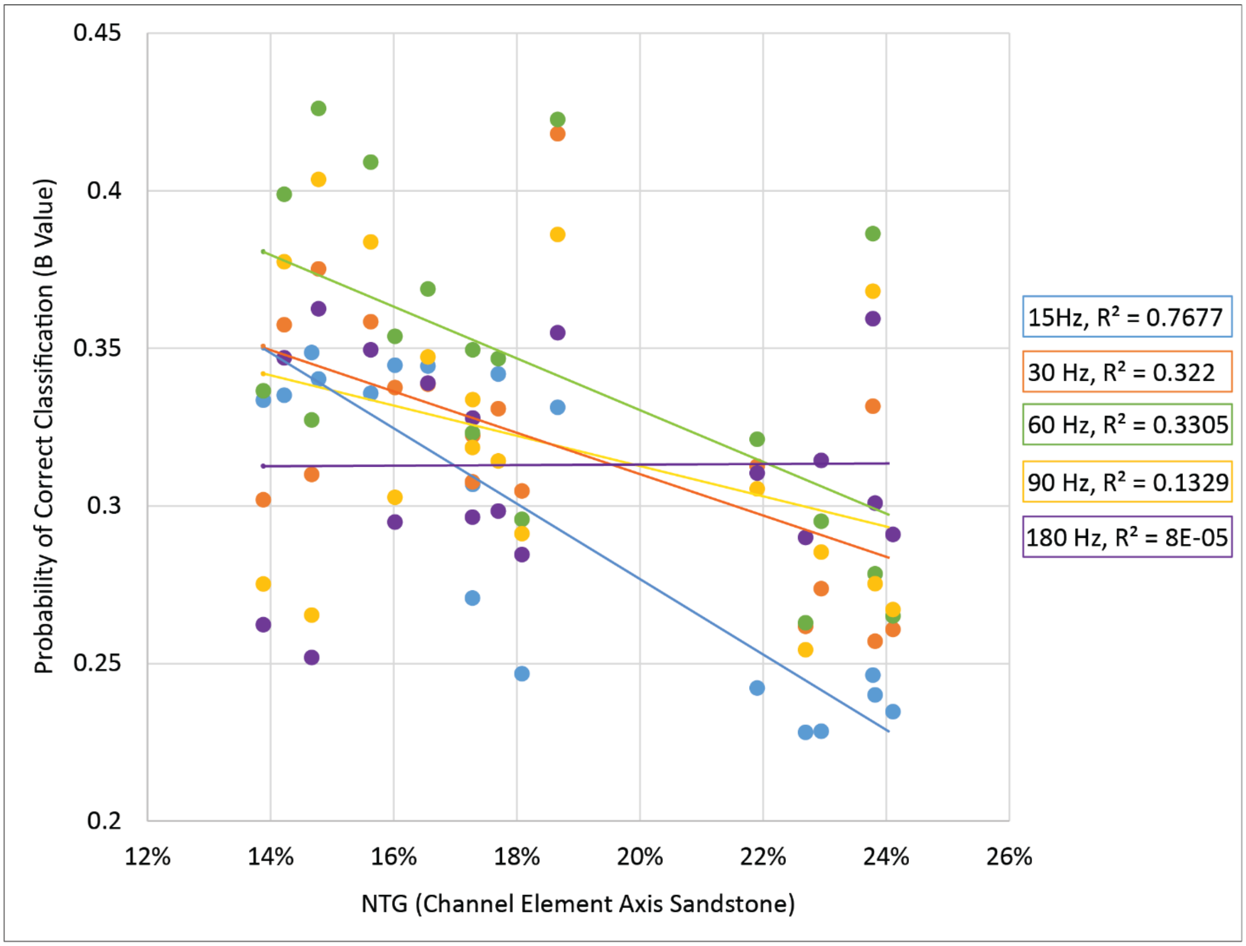

Figure 34. B values for channel element axis sandstone using offshore West Africa rock properties vs net-to-gross (NTG) for each of the eighteen sectors. B values decrease most sharply with increasing NTG at 15 Hz. At 180 Hz, B values increase slightly.

4.3 Summary

The results of this study indicate that inverted 3D seismic models show increasing probability of correct facies classification for channel element axis sandstone with increasing seismic frequency. The results also show increasing probability of correct facies classification for MTDs with increasing seismic frequency. Both results can be explained by the greater impact of tuning at lower frequencies. 3D synthetic seismic models created using deeper rock properties have a higher correct predictability than the models created with shallower rock properties.

The hypothesis that interference from successively stacked channel elements reduces channel element sandstone axis imaging due to the loss of AI contrast proved to be true. Stacking patterns were evaluated using 1) NTG within channel complex set containers as a proxy for stacking and 2) the cumulative distance between stacked channel elements. There is the highest probability of correct classification where there is a large contrast of AI. This is driven by architecture (i.e., channel stacking patterns and MTD location and thickness).

CHAPTER 5: DISCUSSION

The results of this study will have implications for reservoir prediction and modeling. There are implications for interpretation and seismic attributes, and also implications for using probabilities for modeling. These results will be discussed in a broader context and in relation to other relevant studies.

5.1 Implications for Interpretation and Seismic Attributes

This study seeks to quantitatively evaluate the preservation of deep-water channel architecture using 3D synthetic seismic modeling of outcrop data. Exploration seismic typically has 5 to ~20 Hz peak frequency, appraisal has >25 Hz peak frequency, and development scale has up to 50 Hz peak frequency (Stright et al., 2014; Nielson, 2019). Forward seismic modeling provides insight into what higher frequency data may look like if it was available.

As frequency increased within the seismic and inverse models, so did the ability to resolve individual channel elements and mass transport deposits (MTDs), due to less tuning. Models created using shallow offshore West Africa rock properties had smaller tuning thickness than those created with deep Gulf of Mexico rock properties. Pemberton et al. (2018) noted that tuning effects result in composite seismic surfaces that were vertically displaced from their true location, inhibiting accurate interpretation. Similar to this work, at low frequencies (i.e., 15 and 30 Hz), neither the confined channel strata at Laguna Figueroa nor the mixed channel and scour architecture at Arroyo Picana were clearly resolved (Pemberton et al., 2018).

The seismic volumes in this study were inverted to create acoustic impedance models. Well-to-seismic calibration from these models was used to predict facies away from well control.

Factors affecting the quality of this prediction include: the amount of impedance variations in rock properties, quality of the seismic data, and reliability of the impedance volume (Cerney and Bartel, 2012). Thus, the input seismic has a large effect on the quality of the output impedance models. Factors affecting the inversion output also include quality of the input parameters for the inversion and the inversion technique itself (Cerney and Bartel, 2012). Seismically derived impedances are band-limited because the input seismic data are frequency band-limited (Cerney and Bartel, 2012). Low frequency models are used to correct for this. This study had a simple low frequency model which consisted of a prior model cube of P-impedance with a single value of 5.04 kPa.s/m. This simple choice allowed quick creation of the inverse models. A more complex, advanced low frequency model may have led to a better inversion, and thus better interpretation from acoustic impedance, and better well-to-seismic calibration for the facies prediction.

5.2 Implications for Modeling and Probabilities for Modeling

The results of this study indicate that inverted 3D seismic models show increasing probability of correct facies classification (B value) for channel element axis sandstone with increasing seismic frequency. Channel element axis sandstone B value increases gradually up to 60 Hz, then decreases gradually with increasing frequency of 90 and 180 Hz. One possible reason for this is that at higher frequencies, less contrast was seen in the inverse models where there were stacked channels (Figs. 15 and 16). It is possible in these areas, the AI value reverted to the value of the LFM model, which used the AI of shale. Results also showed B values increased steeply for MTDs with increasing frequency. This is because at frequencies less than 150 Hz, the 5m thick MTDs are below tuning thickness. Tomasso et al. (2006) came to the same conclusion when modeling a deep-water slope within the Brushy Canyon Formation of west Texas: that resolvability of architectural elements in seismic is dependent upon object thickness and tuning thickness.

The probability of correct classification was higher for deep rock properties in comparison to shallow rock properties. This was contrary to what was expected. AI is known to increase with depth (Bakke et al., 2013) as is shown within the deeper rock properties used. At deeper plays, the frequency of the seismic signal decreases, which present resolution and imaging issues with seismic data (Schwab et al., 2007). Since the model used does not have noise incorporated, this could be one reason the deeper model did not show a lower probability of correct classification as expected. There would be more noise in a deeper seismic section compared to a shallower seismic section. The probability of higher correct classification for deep rock properties in comparison to shallow rock properties may also result from the fact that the AI range of the deep rock properties is greater than the AI range of the shallow rock properties, providing greater AI contrast.

Numerous studies have created forward seismic reflectivity models from outcrop data to provide insight into what heterogeneity is preserved in a filtered seismic response. Much of this work has been done in 2D, creating synthetic seismic lines (Biddle et al., 1992; Stafleu and Schlager, 1995; Campion et al., 2000; Gartner et al., 2001; Tomasso et al., 2006; Schwab et al., 2007; Falivene et al., 2010; Stright et al., 2014), but more recent work has been done in 3D, generating synthetic seismic volumes (Falivene et al., 2010; Pemberton et al., 2018).

Similarly, Schwab et al. (2007) looks at the effect of channel stacking architecture on seismic response. A simple impedance model with two facies is used to create the 2D synthetic seismic sections. It consists of channel sandstone and a background mud, but lacks the ability to capture heterogeneity from channel axis to margin. Lateral and offset channel configurations were modeled at 30, 40, and 50 Hz. They noted the importance of 3D seismic to verify lateral accretion architecture seen on 2D seismic. Access to 3D data is important since stacking patterns can have a significant impact on facies predictability.

These results provide a quantitative measure of how well facies can be classified from inverted seismic attributes (P-impedance). Identifying how architecture impacts prediction can help scientists understand which scenarios may be risker due to a lower probability of correct facies classification. A higher probability of correct prediction will aid in building better dynamic models for flow modeling. Thus, models with laterally stacked channel elements and higher NTG may be more accurate than those with vertically stacked channel elements and lower NTG. Understanding these results can aid in modeling.

CHAPTER 6: CONCLUSIONS AND FUTURE WORK

6.1 Conclusions

Forward seismic and inverse models were created of a deep-water channel system for a range of frequencies from 15 – 180 Hz using two sets of rock properties from shallow offshore West Africa and the deep Gulf of Mexico. The probability of correctly classifying facies was tested using a Bayesian classification and a Markov-Bayes calibration coefficient. Channel element axis sandstone had increasing probability of correct classification up to 90 Hz, with a slight decrease seen at 120 and 180 Hz. Mass transport deposits (MTDs) are not predicted well at 15 and 30 Hz, but with increasing frequency the effects of tuning on the 5m thick MTDs lessen and the probability of correct classification improves.

There is a highest probability of correct classification where there is a large contrast of AI. This is driven by architecture - channel element stacking patterns and MTD location and thickness. Lower NTG and disorganized stacking leads to a higher probability of correct classification due to isolating and imaging individual channel elements. There is a higher probability of correct classification for deep rock properties compared to shallow rock properties, possibly due to a wider spread of AI values for the deep rock properties.

In summary, laterally stacked or disorganized architecture leads to a better prediction of facies. Thus, there can be higher confidence when modeling channel systems with this architecture, in comparison to vertically stacked or organized channels. Understanding channel architecture can reduce uncertainty in geologic modeling.

6.2 Future Work

Future work on this study can test the impact of noise using both sets of rock properties since this study did not use noise. The deeper set could be tested with more noise than the shallow set because deeper sections tend to be nosier. Testing the impact of noise may make the seismic data and impedance data look more realistic. Other seismic attributes such as instantaneous frequency and phase might be used in similar ways to how amplitude was used in this study.

Data from this study can also be run through a machine learning workflow. Machine learning may increase the probability of correct classification. It may also provide insight as to what variables are affecting the prediction the most.

Future work could use full elastic pre-stack inversion instead of post stack inversion. Full elastic pre-stack inversion produces multiple impedance attributes including P-impedance, s-impedance, and density. Using three attributes (i.e., Vp, Vs, and density) instead of one (Vp) may increase the probability of correct facies classification. The AVO class of the seismic could also be interpreted from the pre-stack seismic cubes.

Lastly, future work could include a more detailed low frequency model. A simple p-impedance cube was used. A more detailed low frequency model can be built using the pseudowells in the model. Additional pseudowells can be added in the inner and outer levee areas so the model is not biased toward channel axis element sandstone, channel off-axis, and channel margin. When used correctly, low frequency models can lead to a more accurate inversion. They can also lead to a worse inversion if they are not built correctly. A variety of low frequency models could be made and tested to see which performs best.

REFERENCES

Alfaro, J. C., Corcoran, C., Davies, K., Pineda, F. G., Hampson, G., Hill, D., Howard, M., Kapoor, J., Moldoveanu, N. & Kragh, E. (2007). Reducing exploration risk. *Oilfield Review, 19,* 26-43.

Armitage, D.A. & Stright, L. (2010). Modeling and interpreting the seismic-reflection expression of sandstone in an ancient mass-transport deposit dominated deep-water slope environment. *Marine and Petroleum Geology, 27*(1), 1-12. https://doi.org/10.1016/j.marpetgeo.2009.08.013

Avseth, P., Mukerji, T., & Mavko, G. (2005). *Quantitative Seismic Interpretation: Applying Rock Physics Tools to Reduce Interpretation Risk*. Cambridge University Press.

Biddle, K.T., Schlager, W., Rudolph, K.W. Bush, T.L. (1992). Seismic Model of a Progradational Carbonate Platform, Picco di Vallandro, the Dolomites, Northern Italy. *AAPG Bulletin, 76*, 14-30.

Cerney B. & Bartel, D.C. (2007). "Uncertainties in low-frequency acoustic impedance models," *The Leading Edge 26*, 74-87. https://doi.org/10.1190/1.2431834

Chopra, S. & Marfurt, K.J. (2008). Emerging and future trends in seismic attributes. *The Leading Edge 27*, 298-318. https://doi.org/10.1190/1.2896620

Covault, J. A., Romans, B. W., & Graham, S. A. (2009). Outcrop expression of a continental-margin-scale shelf-edge delta from the Cretaceous Magallanes Basin, Chile. *Journal of Sedimentary Research, 79*(7–8), 523–539. https://doi.org/10.2110/jsr.2009.053

Dalziel, I.W.D., de Wit, M.J., and Palmer, K.F. (1974). Fossil marginal basin in the southern Andes. *Nature, 250*, 291-294.

Daniels, B.G., Auchter, N.C., Hubbard, S.M., Romans, B.W., Matthews, W.A., & Stright, L. (2018). Timing of deepwater slope evolution constrained by large-n detrital and volcanic ash zircon geochronology, Cretaceous Magallanes Basin, Chile. *Geological Society of America Bulletin, 130*(3–4), 438–454. https://doi.org/10.1130/B31757.1

Daniels, B.G. (2019). Multi-scale and geochronologic investigations of Late Cretaceous sediment-routing systems, Magallanes Basin, Chile [Ph.D. thesis]: Calgary, University of Calgary.

Deptuck, M. E., Steffens, G. S., Barton, M., & Pirmez, C. (2003). Architecture and evolution of upper fan channel-belts on the Niger Delta slope and in the Arabian Sea. *Marine and Petroleum Geology*, *20*(6–8), 649–676. https://doi.org/10.1016/j.marpetgeo.2003.01.004

Epelle, E.I. & Gerogiorgis, D.I. (2020). A review of technological advances and open challenges for oil and gas drilling systems engineering. AIChE *Journal, 66*(4) e16842. https://doi.org/10.1002/aic.16842

Fildani, A., & Hessler, A.M. (2005). Stratigraphic record across a retroarc basin inversion: Rocas Verdes-Magallanes Basin, Patagonian Andes, Chile. *Geological Society of America Bulletin, 117(11-12),* 1596–1614. https://doi.org/10.1130/B25708.1.

Fletcher, S. (2013). Stratigraphic characterization of a Cretaceous slope channel complex in the Tres Pasos Formation, Arroyo Picana-Laguna Figueroa outcrop belt [M.S. thesis]: Calgary, University of Calgary.

Fosdick, J. C., Romans, B., Fildani, A., Bernhardt, A., Calderon, M., & Graham, S. A. (2011). Kinematic evolution of the Patagonian retroarc fold-and-thrust belt and Magallanes foreland basin, Chile and Argentina, 51°30'S. *Geological Society of America Bulletin. 123*(9-10), 1679-1698. https://doi.org/10.1130/B30242.1

Goovaerts, P. (1997) *Geostatistics for natural resources evaluation.* Oxford University Press.

Hubbard, S.M., Fildani, A., Romans, B.W., Covault, J.A., & McHargue, T.R. (2010). High-relief slope clinoform development: Insights from outcrop, Magallanes Basin, Chile. *Journal of Sedimentary Research, 80*, 357–375. https://doi.org/10.2110/jsr.2010.042

Hubbard, S. M., Covault, J. A., Fildani, A., & Romans, B. W. (2014). Sediment transfer and deposition in slope channels: Deciphering the record of enigmatic deep-sea processes from outcrop. *Geological Society of America Bulletin, 126*(5–6), 857–871. https://doi.org/10.1130/B30996.1

Jackson, A., Stright, L., Hubbard, S.M., & Romans, B.W. (2019). Static connectivity of stacked deep-water channel elements constrained by high-resolution digital outcrop models. *AAPG Bulletin, 103,* 2943–2973. https://doi.org/10.1306/03061917346

La Marca, K., Silver, C., Bedle, H. & Slatt, R. (2019). Seismic facies identification in a deepwater channel complex applying seismic attributes and unsupervised machine learning techniques. A case study in the Taranaki Basin, New Zealand. *SEG Technical Program Expanded Abstracts,* 2059-2063. https://doi.org/10.1190/segam2019-3216705.1

La Marca, K. (2020). Seismic attribute optimization with unsupervised machine learning techniques for deepwater seismic facies interpretation: users vs machines. [M.S. thesis]: Norman, OK, University of Oklahoma.

Li, W., Yue, D., Wang, W., Wang, W., Wu, S., Li, J., & Chen, D. (2009). Fusing multiple frequency-decomposed seismic attributes with machine learning for thickness prediction and sedimentary facies interpretation in fluvial reservoirs. *Journal of Petroleum Science and Engineering, 177*, 1087-1102. https://doi.org/10.1016/j.petrol.2019.03.017

Kane, I. A., & Hodgson, D. M. (2011). Sedimentological criteria to differentiate submarine channel levee subenvironments: Exhumed examples from the Rosario Fm. (Upper Cretaceous) of Baja California, Mexico, and the Fort Brown Fm. (Permian), Karoo Basin, S. Africa. *Marine and Petroleum Geology, 28*(3), 807–823.https://doi.org/10.1016/j.marpetgeo.2010.05.009

Macauley, R., & Hubbard, S.M. (2013). Slope channel sedimentary processes and stratigraphic stacking, Cretaceous Tres Pasos Formation slope system, Chilean Patagonia. *Marine and Petroleum Geology, 41*, 146–162. https://doi.org/10.1016/j.marpetgeo.2012.02.004

Maier, K. L., Gales, J. A., Paull, C. K., Rosenberger, K., Talling, J., Simmons, S. M., Gwiazda, R., McGann, M., Cartigny, M. J.B., Lundsten, E., Anderson, K., Clare, M. A., Xu, J., Parsons, D., Barry, J., Wolfson-Schwehr, M., Nieminski, N. M., & Sumner, E. J. (2019). Linking direct measurements of turbidity currents to submarine canyon-floor deposits. *Frontiers in Earth Science, 7*, 1-18. https://doi.org/10.3389/feart.2019.00144

McHargue, T., Pyrcz, M. J., Sullivan, M. D., Clark, J. D., Fildani, A., Romans, B.W., & Drinkwater, N.J., 2011, Architecture of turbidite channel systems on the continental slope: Patterns and predictions. *Marine and Petroleum Geology, 28*, 728–743. https://doi.org/10.1016/j.marpetgeo.2010.07.008.

Meirovitz, C., Stright, L., Hubbard, S.M., Romans, B.W. (2020). The Influence of Inter- and Intra-channel Architecture on Deep-water Turbidite Reservoir Performance. *Petroleum Geoscience, 27*(2). https://doi.org/10.1144/petgeo2020-005

Nardin, T.R., Hein, F.J., Gorsline, D.S., & Edwards, B.D. (1979). A review of mass movement processes, sediment and acoustic characteristics, and contrasts in slope and base-of-slope systems versus canyon-fan-basin floor systems. *SEPM Special Publication, 27*, 61-73. https://doi.org/10.2110/pec.79.27.0061

Neal, J., & Krohn, C., 2012. Higher Resolution Subsurface Imaging. *Society of Petroleum Engineers, 64*(3), 44-53. https://doi.org/10.2118/0312-0044-JPT

Nielson, A. (2017). Using RMS Amplitudes from Forward Seismic-Reflectivity Modeling of Channelized Deep-Water Slope Deposits To Inform Stratigraphic Interpretation and Sub-Seismic Scale Architecture, Tres Pasos Formation, Magallanes Basin, Patagonia, Chile. [M.S. thesis]: Fort Collins, CO, Colorado State University.

Pemberton, E.A.L, Hubbard, S.M., Fildani, A., Romans, B., Stright, L. (2016). The stratigraphic expression of decreasing confinement along a deep-water sediment routing system: Outcrop example from southern Chile. *Geosphere, 12*(1), 114–134. https://doi.org/10.1130/GES01233.1

Pemberton, E.A.L., Stright, L., Fletcher, S., & Hubbard, S.M. (2018). The influence of stratigraphic architecture on seismic response: Reflectivity modeling of outcropping deepwater channel units. *Interpretation, 6*, T783–T808. https://doi.org/10.1190/int-2017-0170.1

Pettingill H. & Weimer, P. (2002). World-Wide Deepwater Exploration and Production: Past, Present, and Future. [Conference Presentation]. Offshore Technology Conference, Houston, TX. https://doi.org/10.4043/14024-ms

Posamentier, H. W., & Kolla, V. (2003). Seismic geomorphology and stratigraphy of depositional elements in deep-water settings. *Journal of Sedimentary Research, 73*(3), 367–388. https://doi.org/10.1306/111302730367

Randolph, M.F., Gaudin, C., Gourvenec, S.M., White, D.J., Boylan, N., & Cassidy, M.J. (2011). Recent advances in offshore geotechnics for deep water oil and gas developments. *Ocean Engineering, 38*(7), 818-834. https://doi.org/10.1016/j.oceaneng.2010.10.021

Regenauer-Lieb, K., Poulet, T., Veveakis, M., Hamid, R., & Chen, X. (2018). Next Generation Reservoir Engineering. ASEG Extended Abstracts. 2018. 1, 1-5. https://doi.org/10.1071/ASEG2018abM3_4C

Romans, B.W., Hubbard, S.M., & Graham, S.A. (2009). Stratigraphic evolution of an outcropping continental slope system, Tres Pasos Formation at Cerro Divisadero, Chile. *Sedimentology, 56*, 737–764. https://doi.org/10.1111/j.1365-3091.2008.00995.x.

Romans, B. W., Fildani, A., Graham, S. A., Hubbard, S. M., & Covault, J. A. (2010). Importance of predecessor basin history on sedimentary fill of a retroarc foreland basin: provenance analysis of the Cretaceous Magallanes basin, Chile (50-52°S). *Basin Research*, *22*(5), 640–658. https://doi.org/10.1111/j.1365-2117.2009.00443.x

Romans, B.W., Fildani, A., Hubbard, S.M., Covault, J.A., Fosdick, J.C., & Graham, S.A. (2011). Evolution of deep-water stratigraphic architecture, Magallanes Basin, Chile. *Marine and Petroleum Geology, 28*(3)*,* 612–628. https://doi.org/10.1016/j.marpetgeo.2010.05.002

Ruetten, A. (2021). Evaluating the Impact of Hierarchical Deep-Water Slope Channel Architecture on Fluid Flow Behavior, Cretaceous Tres Pasos Formation, Chile [M.S. thesis]: Fort Collins, CO, Colorado State University.

Russell, B., & Hampson, D. (1991). Comparison of poststack seismic inversion methods, SEG Technical Program Expanded Abstracts: 876-878. https://doi.org/10.1190/1.1888870

Petrel (2019). Schlumberger.

Sheriff, R., & Geldart, L. (1995). *Exploration Seismology (2nd ed.).* Cambridge: Cambridge University Press. https://doi.org/10.1017/CBO9781139168359

Slatt, R.M. (2006). *Stratigraphic reservoir characterization for petroleum geologists, geophysicists, and engineers: Handbook of Petroleum Exploration and Production*, 6, Elsevier, Amsterdam.

Southern, S.J., Stright, L., Jobe, Z.R., Romans, B., & Hubbard, S. (2017). The stratigraphic expression of slope channel evolution: insights from qualitative and quantitative assessment of channel fills from the Cretaceous Tres Pasos Formation, southern Chile. AAPG Annual Convention, Houston, TX.

Stright, L., Stewart, J., Campion, K., & Graham, S. (2014). Geologic and seismic modeling of a coarse-grained deep-water channel reservoir analog (Black's Beach, La Jolla, California). *AAPG Bulletin, 98*(4), 695 – 728. https://doi.org/10.1306/09121312211

Vento, N. (2020). Hypothesis-based machine learning for deep-water channel systems [M.S. thesis]: Fort Collins, CO, Colorado State University.

Wilson, T. J. (1991). Transition from back-arc to foreland basin development in the southernmost Andes: Stratigraphic record from the Ultima Esperanza District, Chile. *Geological Society of America Bulletin, 103*, 98–111. https://doi.org/10.1130/00167606(1991)103<0098:TFBATF>2.3.CO;2

Yilmaz, O. (2001). *Seismic Data Analysis: Processing, Inversion, and Interpretation of Seismic Data.* (S. M. Doherty, Ed.). Society of Exploration Geophysicists. https://doi.org/10.1190/1.9781560801580

Zhang, L., Wang, H., Li, Y. & Pan, M. (2017). Quantitative characterization of sandstone amalgamation and its impact on reservoir connectivity. *Petroleum Exploration and Development, 44*(2), 226–233. https://doi.org/10.1016/S1876-3804(17)30025-3

Zhu, H., Journel, A.G. (1993). *Formatting and Integrating Soft Data: Stochastic Imaging via the Markov-Bayes Algorithm*. (A. Soares, Ed.) *Geostatistics Tróia '92*. Quantitative Geology and Geostatistics, 5. Springer, Dordrecht.

APPENDIX A: FORWARD SEISMIC MODELS

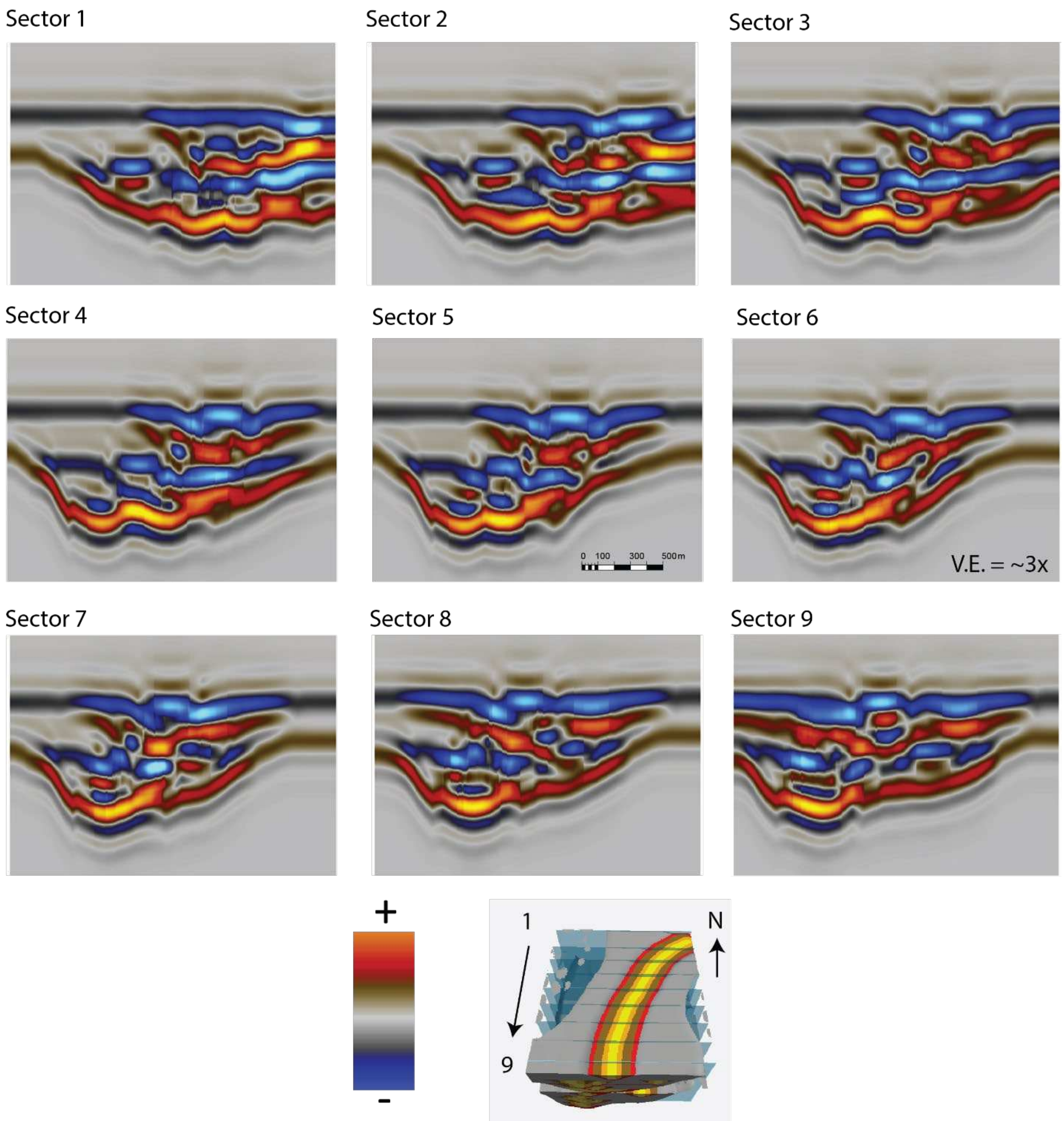

Figure A1. Sectors of the 3D forward seismic model at 15 Hz using shallow offshore West Africa rock properties.

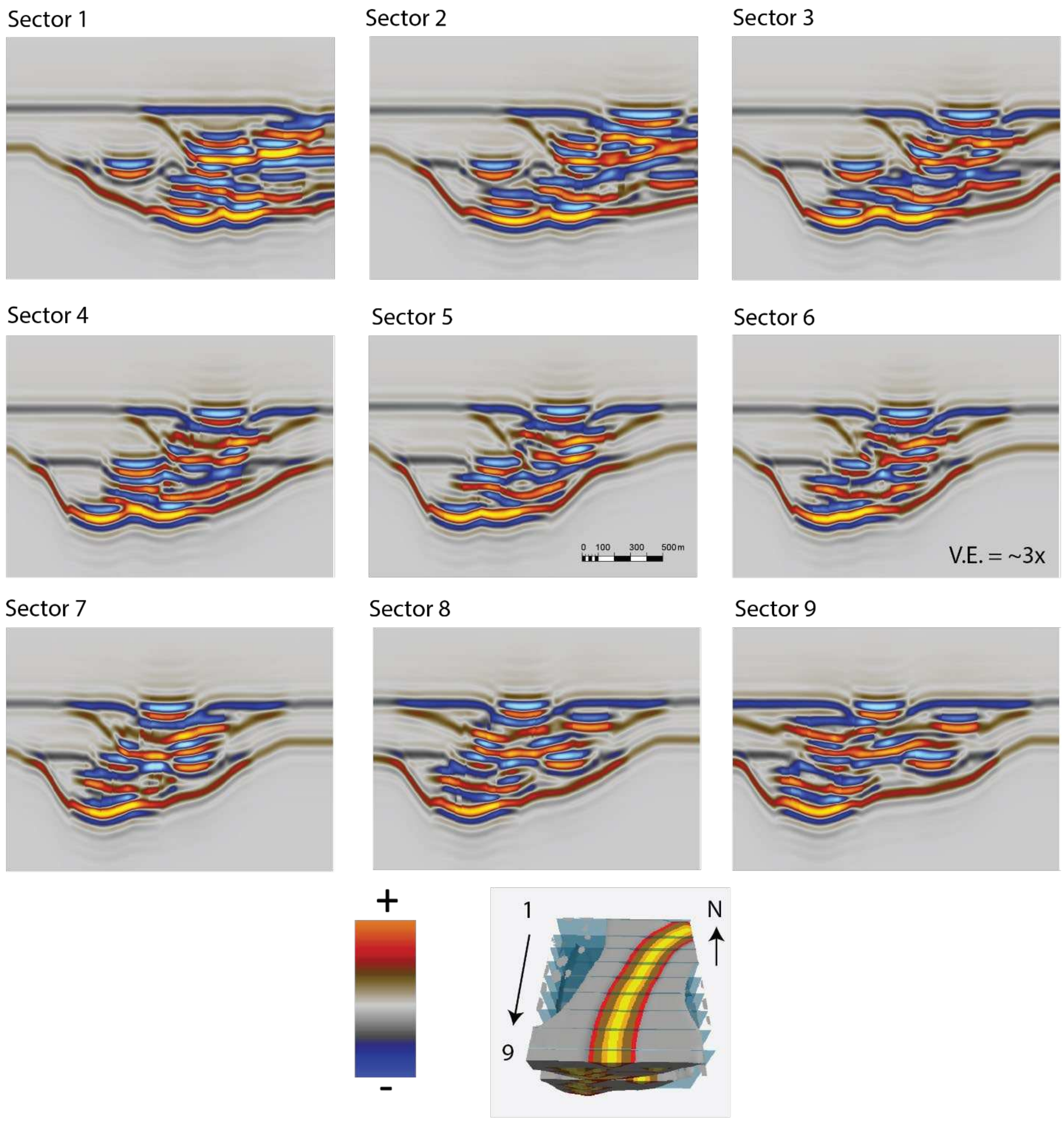

Figure A2. Sectors of the 3D forward seismic model at 30 Hz using shallow offshore West Africa rock properties.

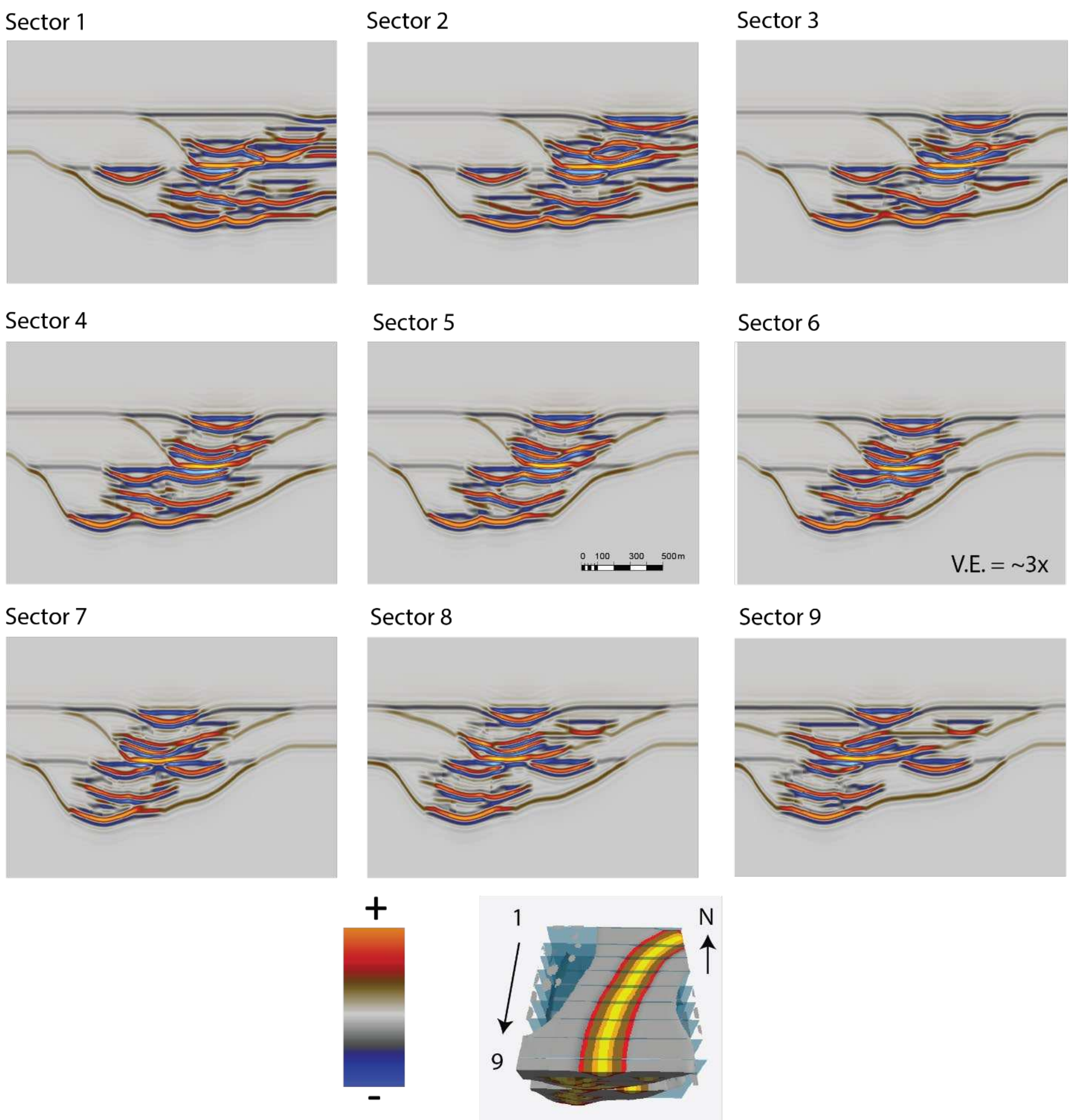

Figure A3. Sectors of the 3D forward seismic model at 60 Hz using shallow offshore West Africa rock properties.

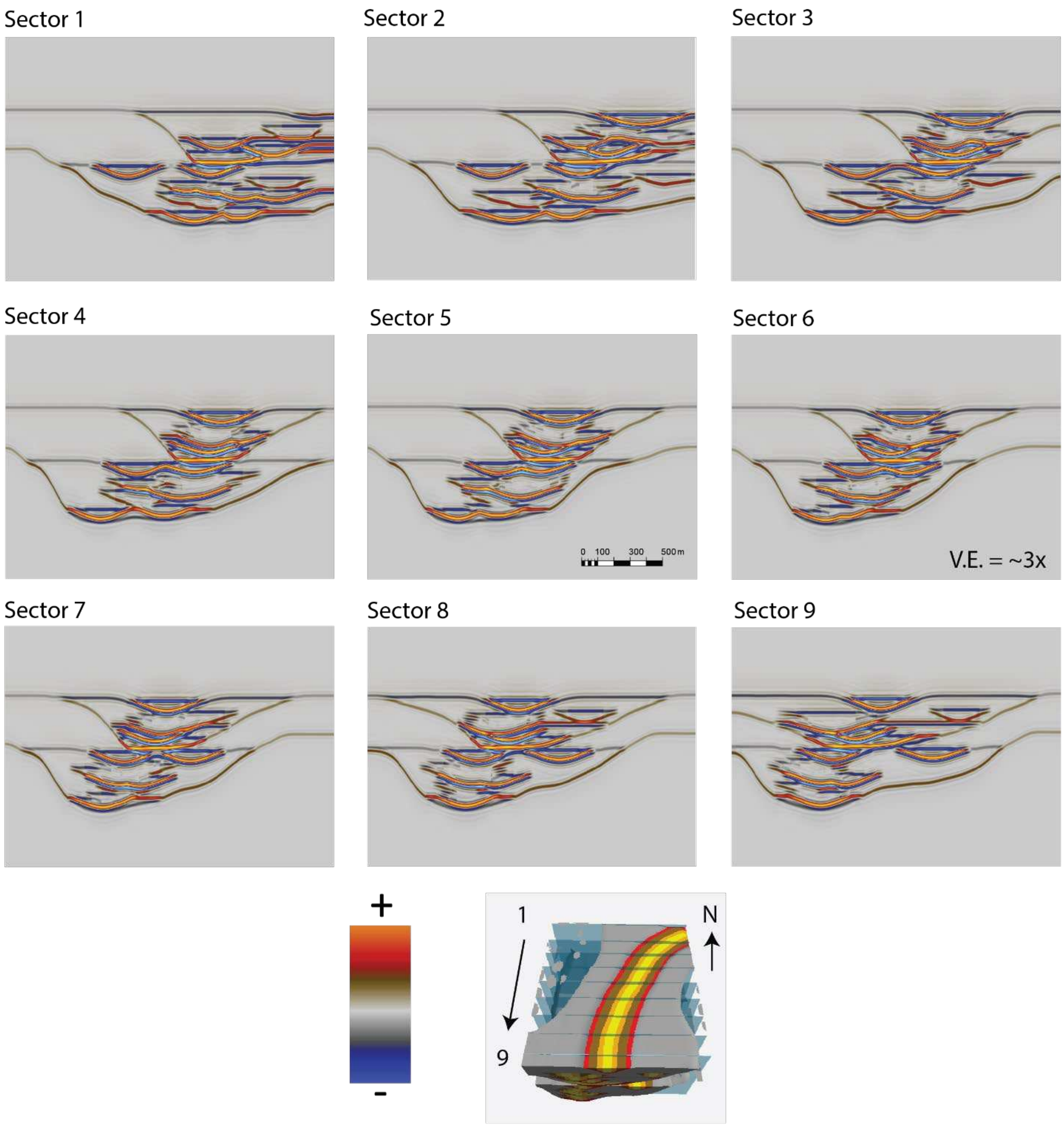

Figure A4. Sectors of the 3D forward seismic model at 90 Hz using shallow offshore West Africa rock properties.

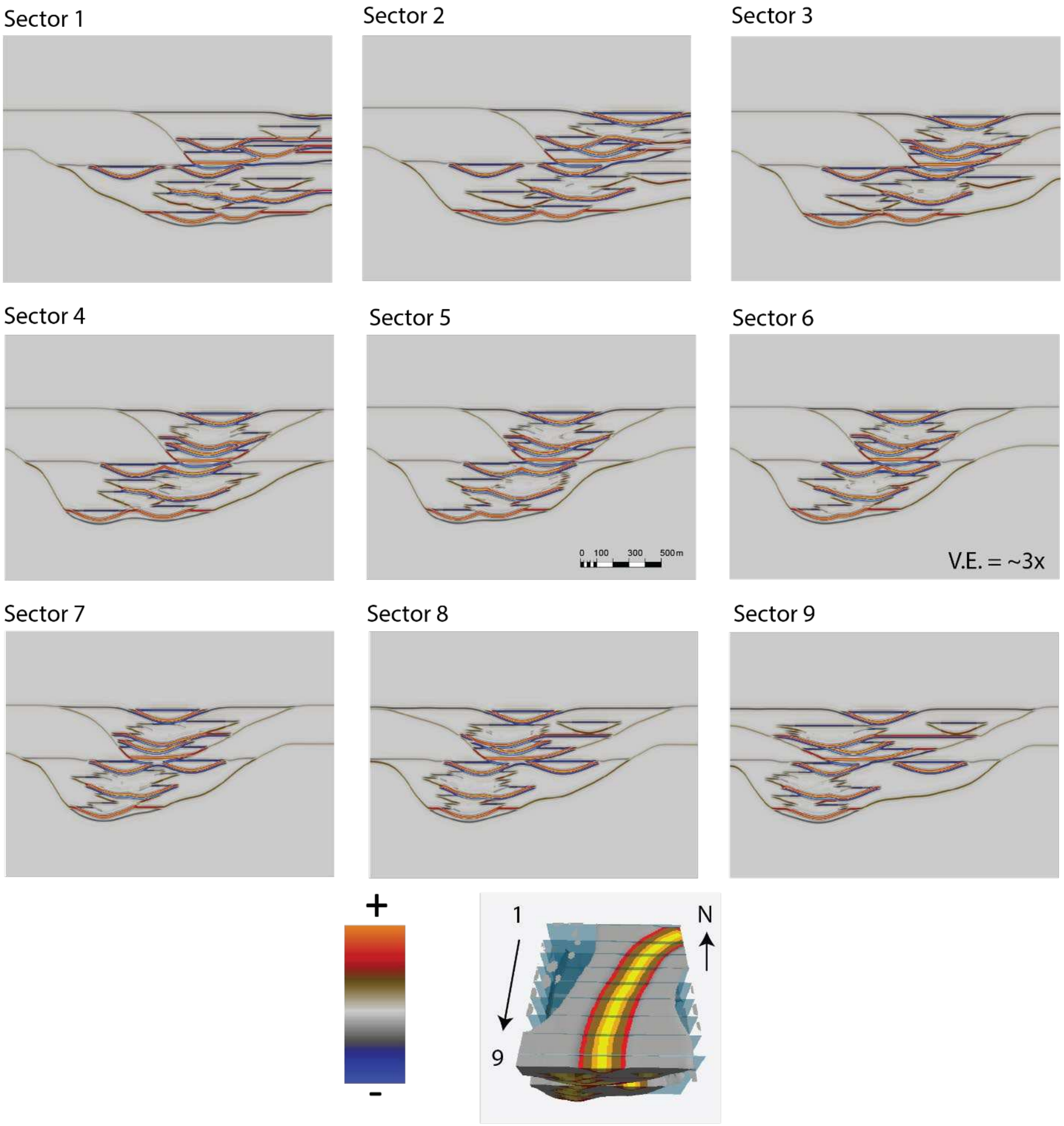

Figure A5. Sectors of the 3D forward seismic model at 180 Hz using shallow offshore West Africa rock properties.

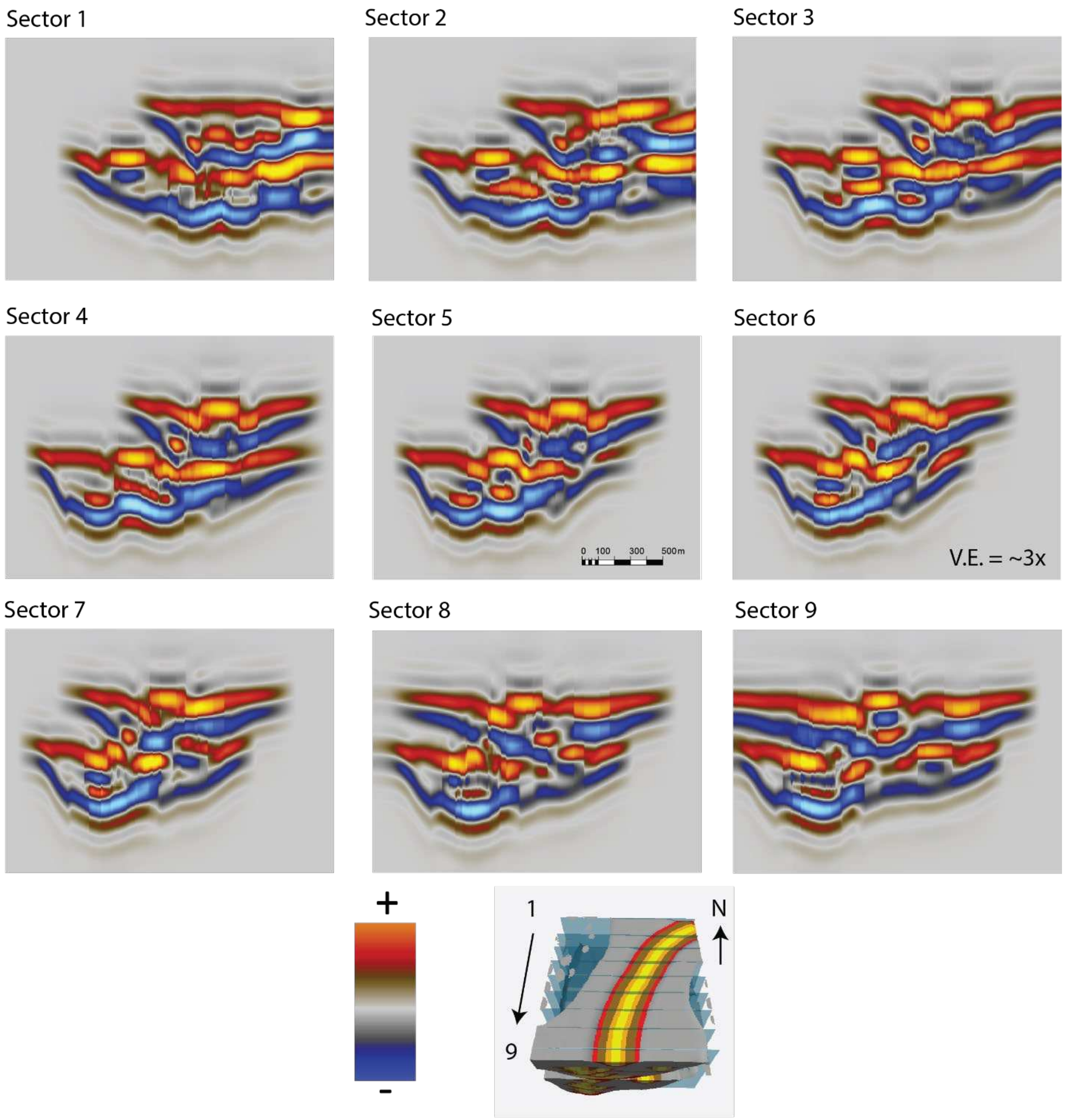

Figure A6. Sectors of the 3D forward seismic model at 15 Hz using deep Gulf of Mexico rock properties.

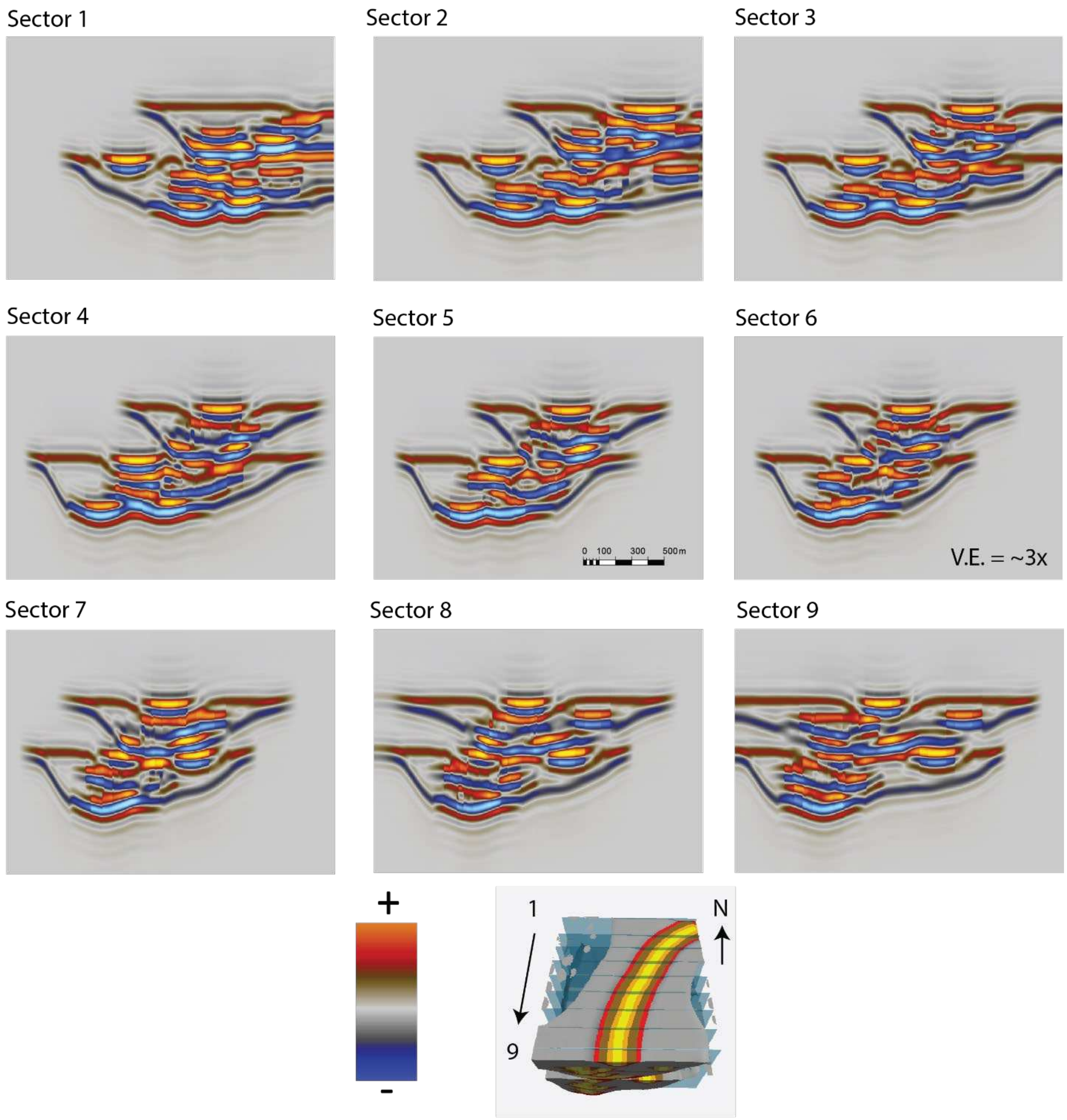

Figure A7. Sectors of the 3D forward seismic model at 30 Hz using deep Gulf of Mexico rock properties.

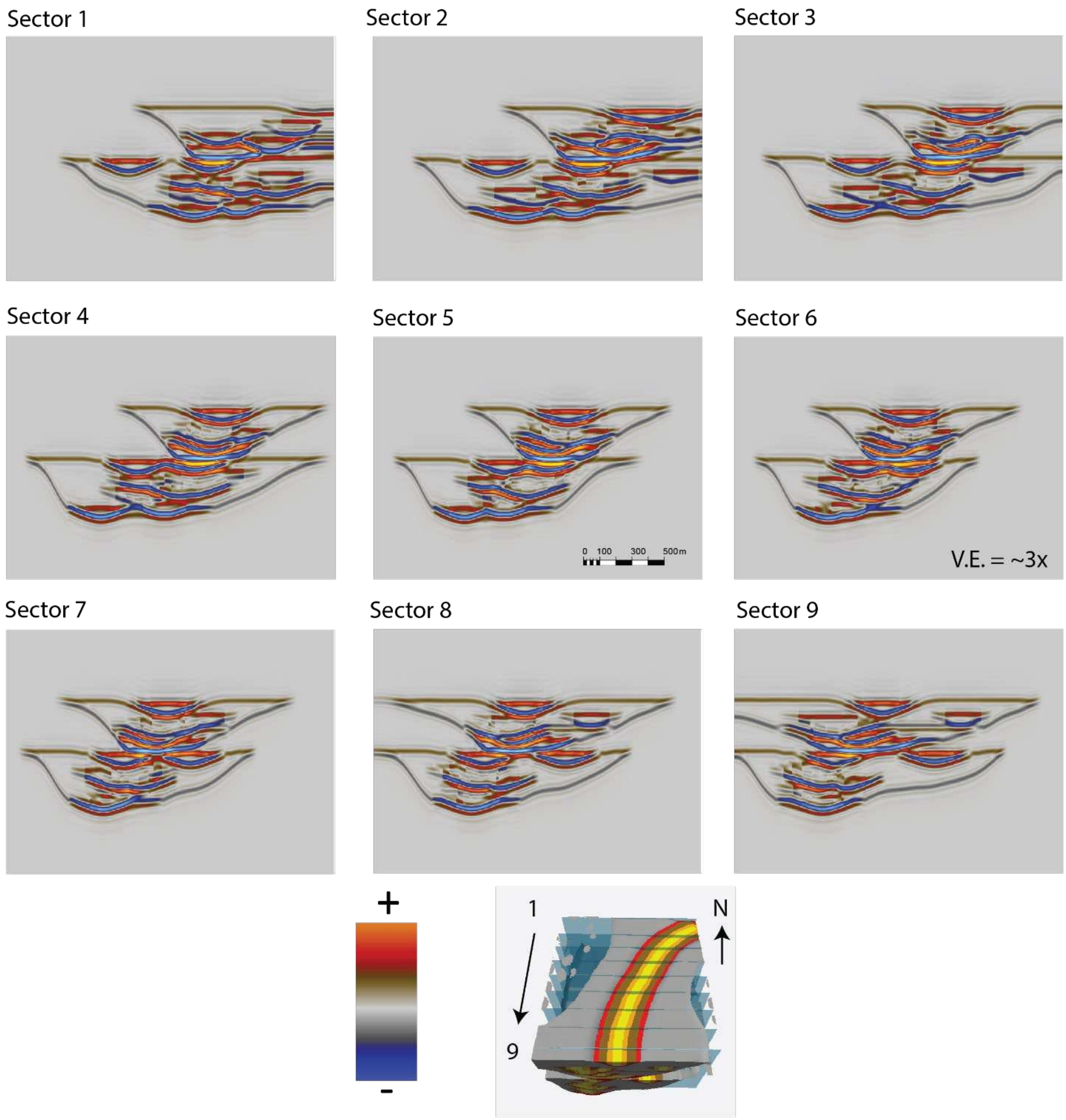

Figure A8. Sectors of the 3D forward seismic model at 60 Hz using deep Gulf of Mexico rock properties.

APPENDIX B: INVERSE MODELS:

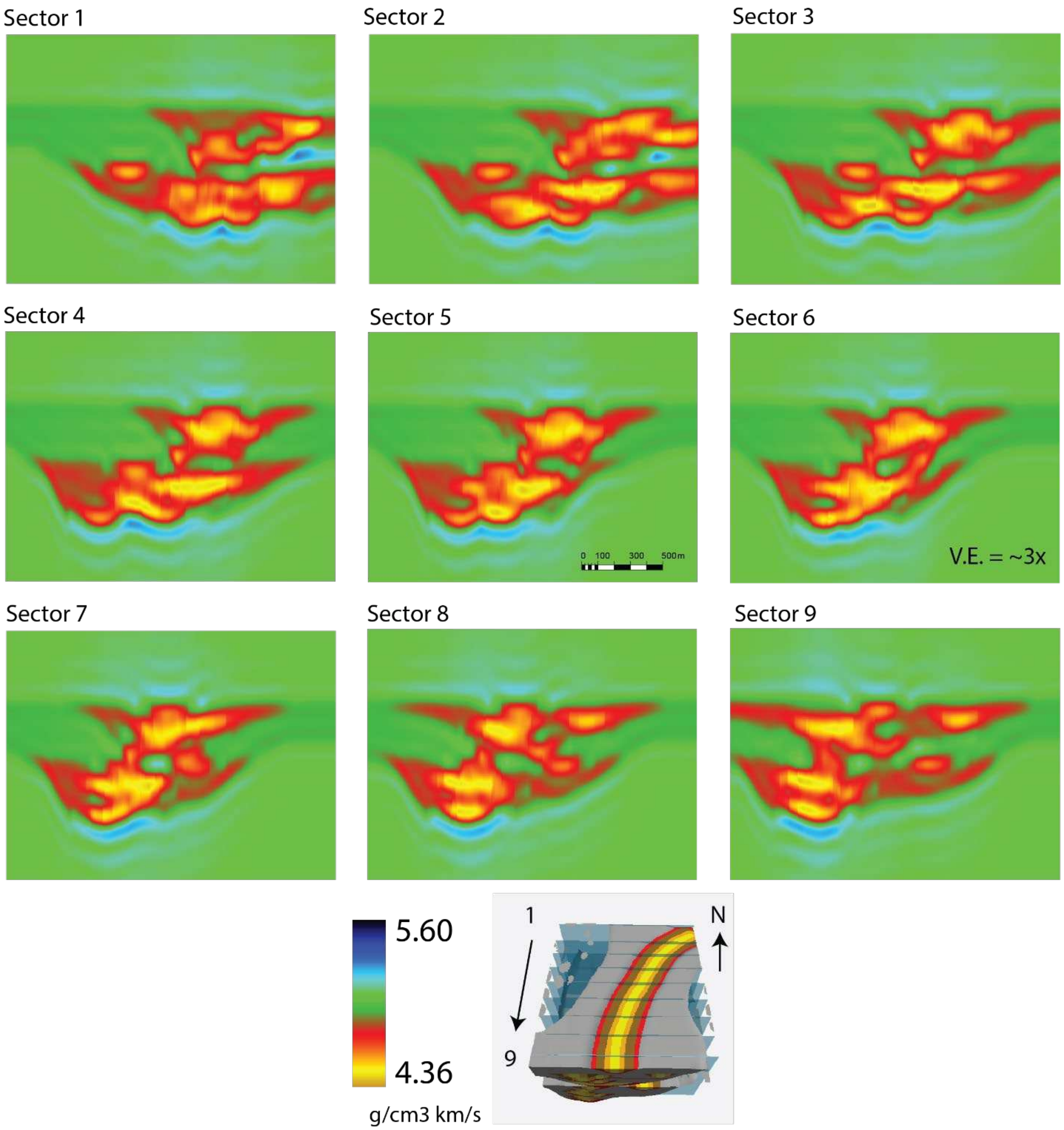

Figure B1. Sectors of the 3D inverse model showing acoustic impedance (g/cm^3 km/s) at 15 Hz using shallow offshore West Africa rock properties.

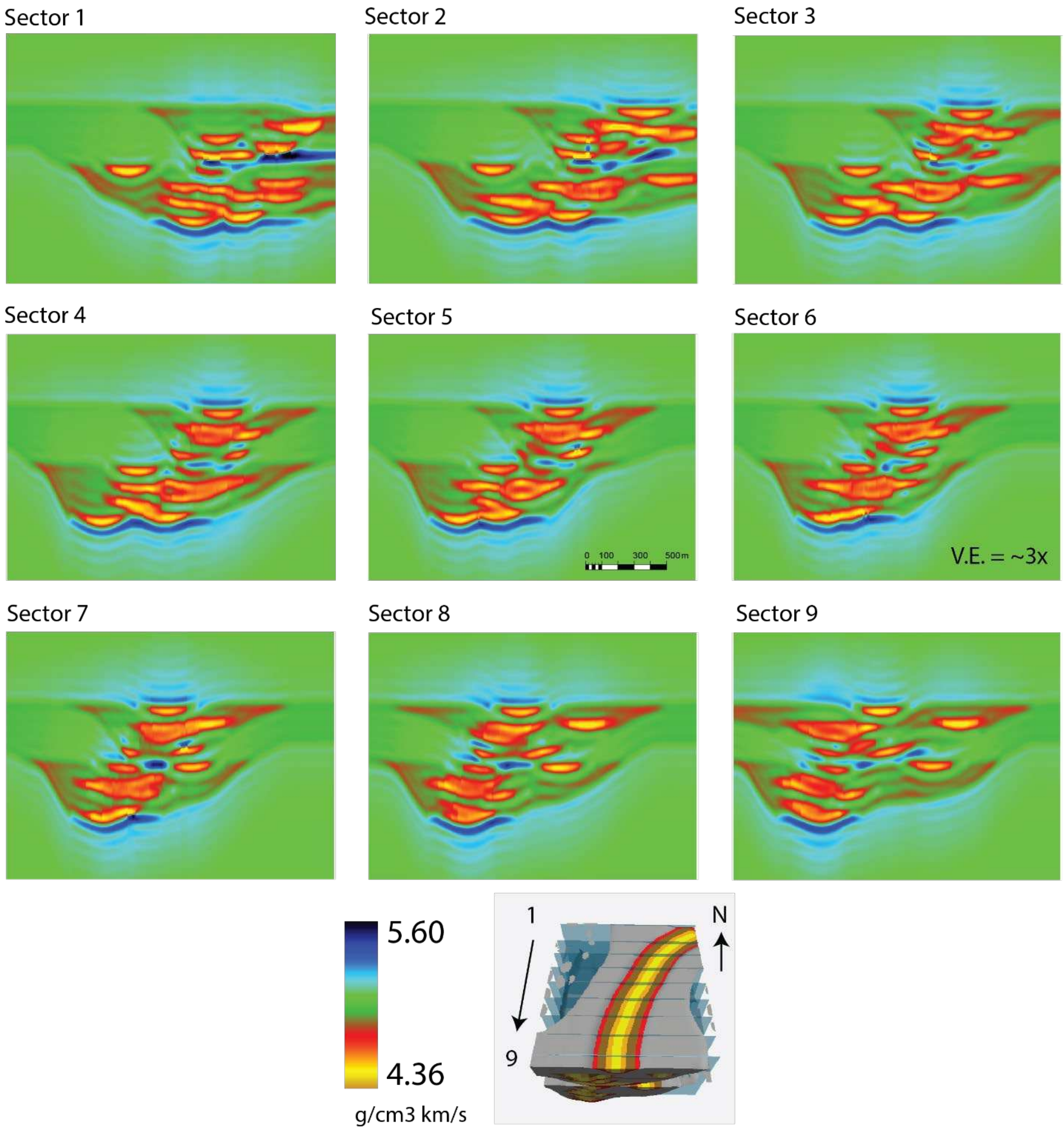

Figure B2. Sectors of the 3D inverse model showing acoustic impedance (g/cm^3 km/s) at 30 Hz using shallow offshore West Africa rock properties.

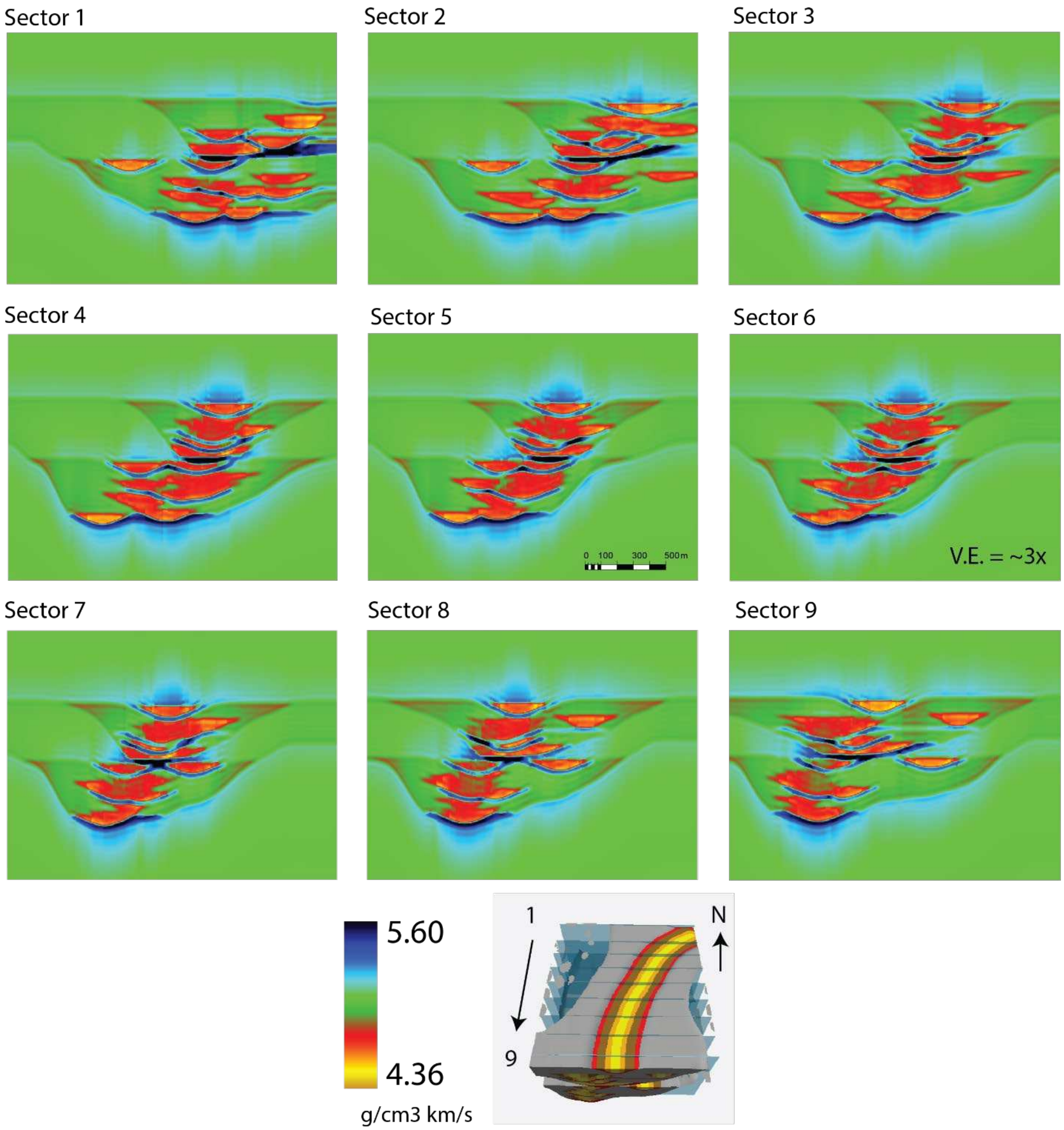

Figure B3. Sectors of the 3D inverse model showing acoustic impedance (g/cm^3 km/s) at 60 Hz using shallow offshore West Africa rock properties.

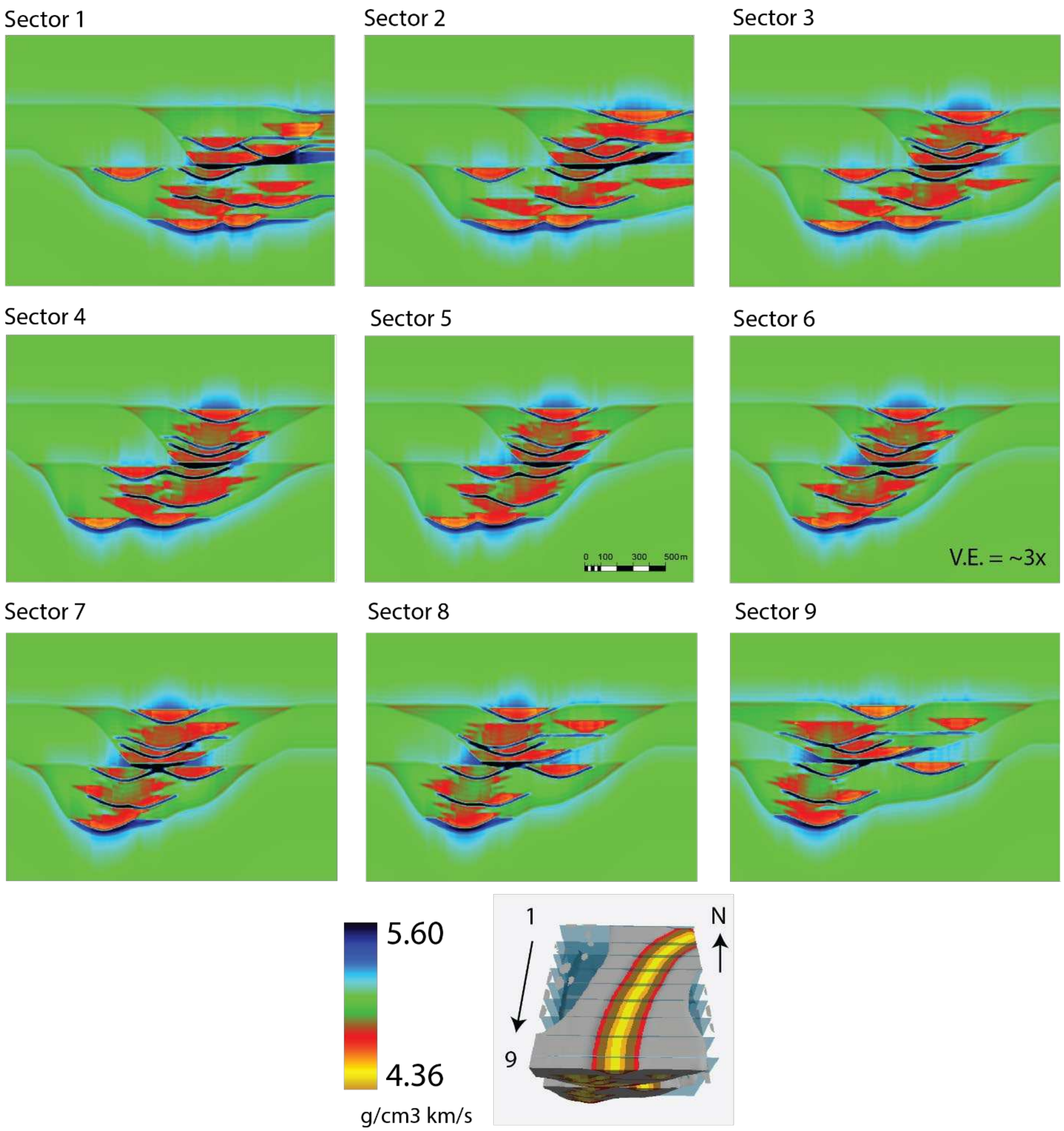

Figure B4. Sectors of the 3D inverse model showing acoustic impedance (g/cm^3 km/s) at 90 Hz using shallow offshore West Africa rock properties.

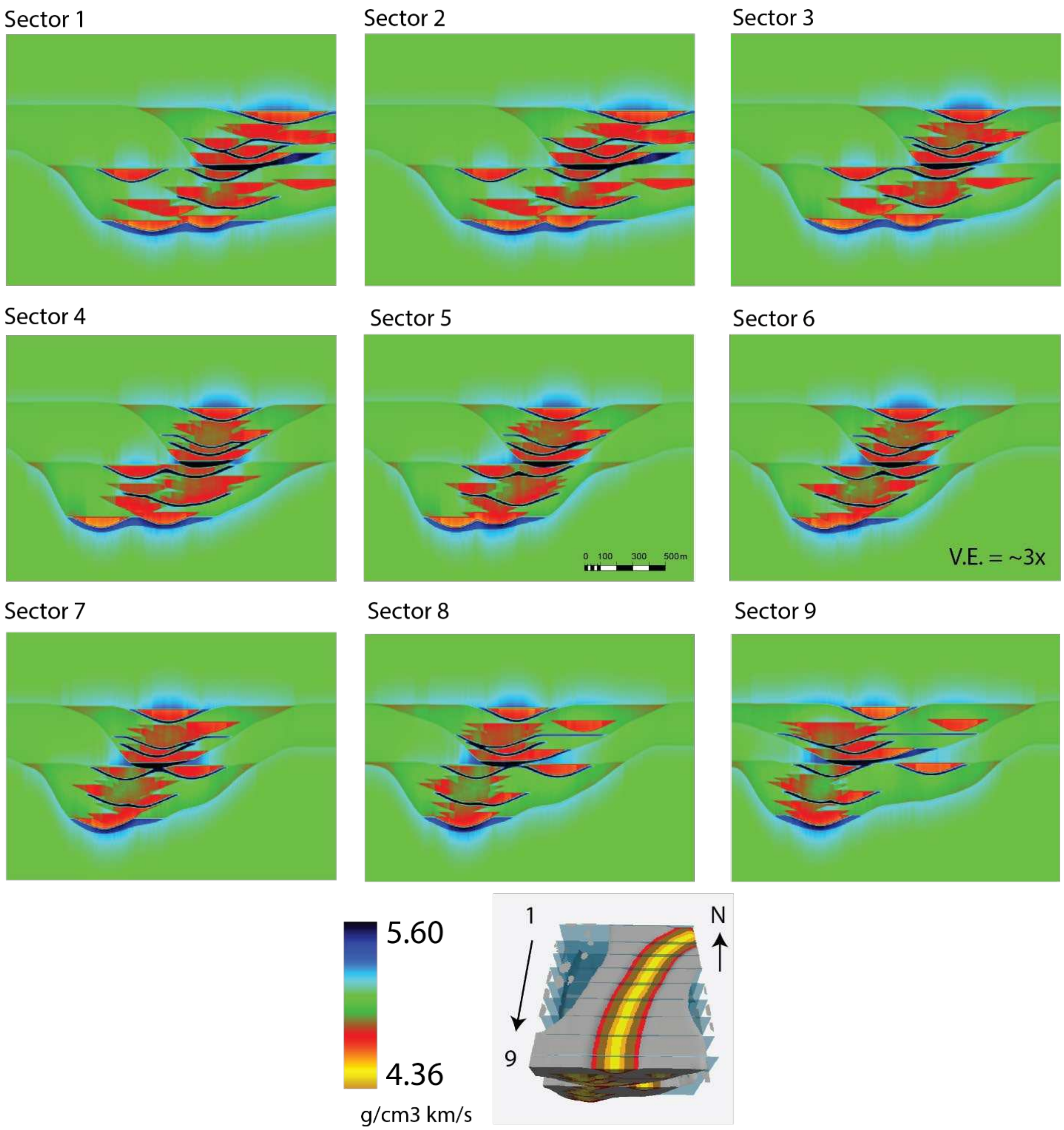

Figure B5. Sectors of the 3D inverse model showing acoustic impedance (g/cm^3 km/s) at 180 Hz using shallow offshore West Africa rock properties.

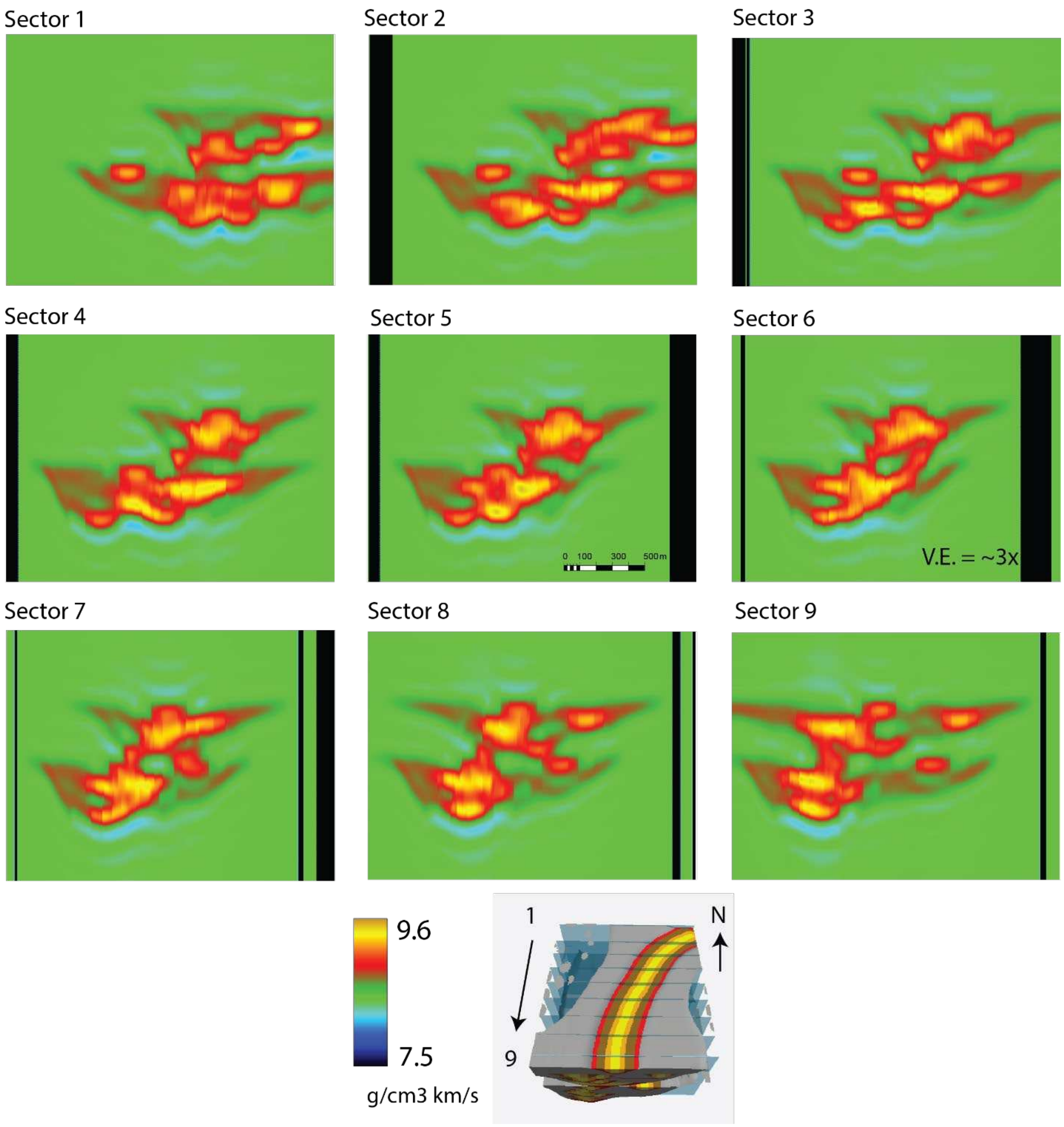

Figure B6. Sectors of the 3D inverse model showing acoustic impedance (g/cm^3 km/s) at 15 Hz using deep Gulf of Mexico rock properties.

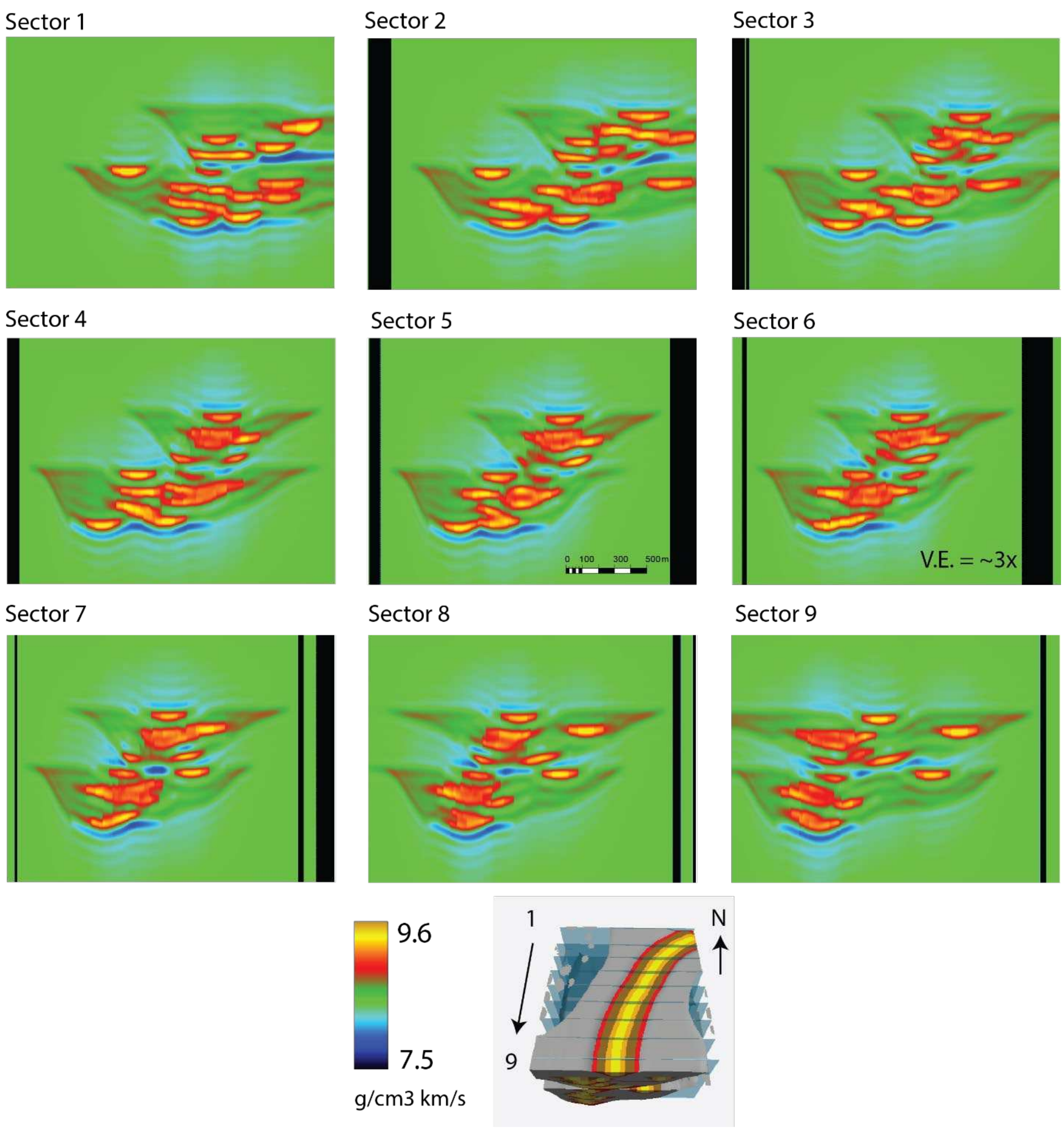

Figure B7. Sectors of the 3D inverse model showing acoustic impedance (g/cm^3 km/s) at 30 Hz using deep Gulf of Mexico rock properties.

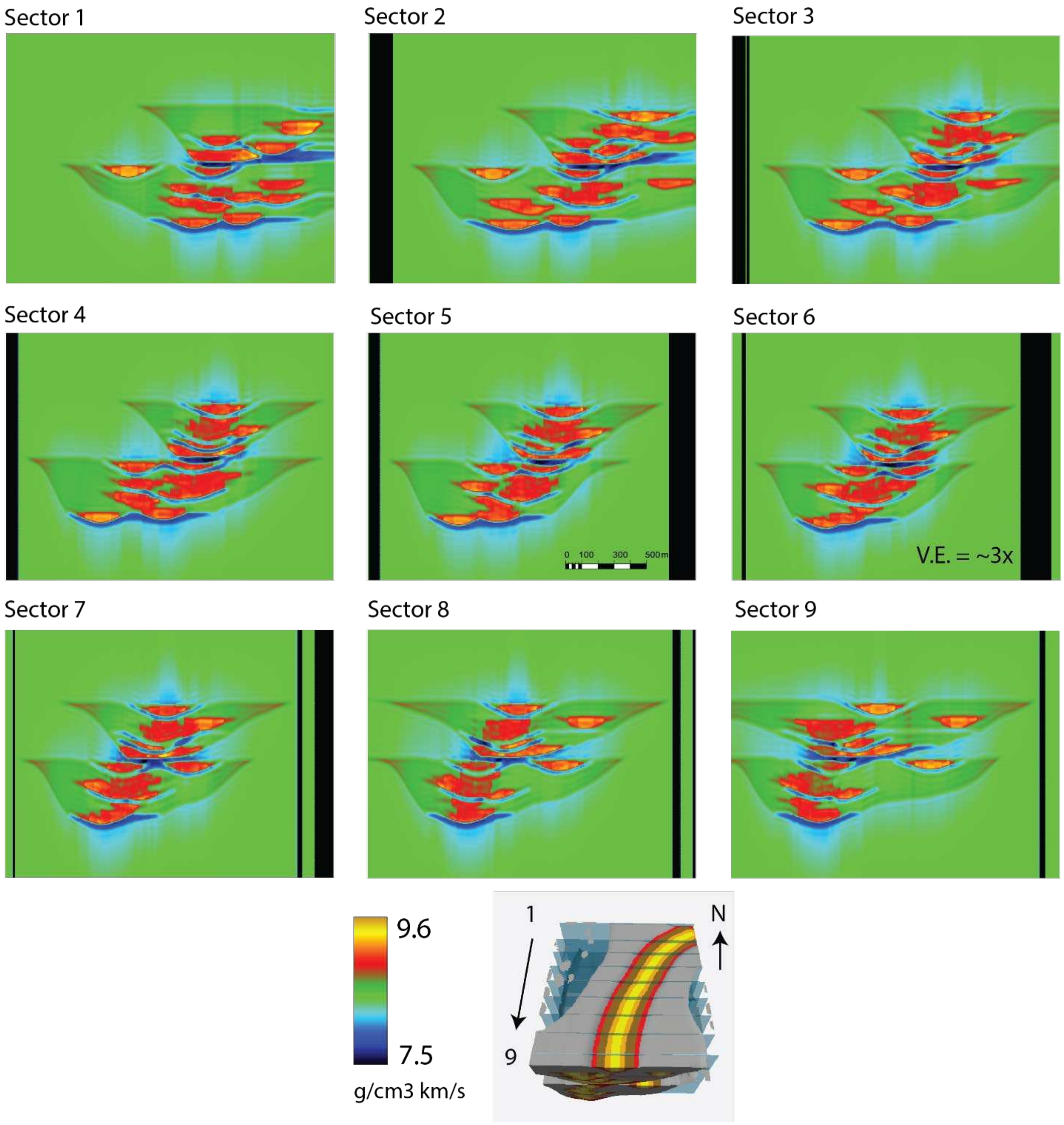

Figure B8. Sectors of the 3D inverse model showing acoustic impedance (g/cm^3 km/s) at 60 Hz using deep Gulf of Mexico rock properties.